LEIBNIZ-INSTITUT
FÜR
ATMOSPHÄREN
PHYSIK

INAUGURAL-DISSERTATION

am Leibniz-Institut für Atmosphärenphysik in Kühlungsborn
zur Erlangung der Doktorwürde
der Mathematisch-Naturwissenschaftlichen Fakultät
der Universität Rostock

Stratospheric turbulence observations with the new balloon-borne instrument LITOS

von
Anne Theuerkauf

Abstract: A balloon-borne instrument called LITOS (Leibniz-Institute Turbulence Observations in the Stratosphere) has been developed to study turbulence in the stratospheric wind and temperature field down to the smallest spatial scales of millimeters. LITOS has been successfully launched two times from Kiruna (67 °N, 21 °E) and several times from the institute site in Khlungsborn (54 °N, 12 °E). Since hot and cold wire techniques have never been used before on balloon platforms, laboratory measurements have been performed to verify their applicability for stratospheric conditions. The Kiruna flights show the intermittent structure of turbulence in the stratosphere. In addition, the results of a cluster algorithm reveal that more turbulent layers have been observed within the stratosphere than in the troposphere. On average the turbulent layers are only several ten meters thick. Furthermore, turbulent layers within the temperature field are typically thinner compared to layers in the wind field. Based on a modified theory, the energy dissipation rate has been determined with high precision, and detailed altitude profiles are obtained. The dissipation rates vary between 9.9×10^{-4} and 7.5×10^{-2} W/kg. The profiles reveal an increase of the energy dissipation rate with altitude. The mean energy dissipation rates unexpectedly differ between turbulence in the temperature and wind field. The values for the temperature profile are typically one to two orders of magnitude higher than for the wind profiles. To relate the turbulent layers to the atmospheric background conditions, the Richardson number has been determined. However, the analyses reveal that no direct relation between the Richardson number and turbulent layers has been found. The investigations of possible sources show that Kelvin-Helmholtz instabilities are the main source for some of the turbulent layer.

Postal address:
Schloss-Str. 6
18225 Ostseebad Kühlungsborn
Germany

IAP Kühlungsborn
Dezember 2012
IAP Nr. 33/2013
ISSN 1615–8083

LEIBNIZ-INSTITUT FÜR ATMOSPHÄREN PHYSIK

Stratospheric turbulence observations with the new balloon-borne instrument LITOS

von
Anne Theuerkauf

Dieser Forschungsbericht wurde als Dissertation von der Mathematisch-Naturwissenschaftlichen Fakultät der Universität Rostock angenommen.

Gutachter: **Prof. Dr. F.-J. Lübken (Universität Rostock)**
Prof. Dr. A. Leder (Universität Rostock)

verteidigt am: 21. Dezember 2012

Abstract

A balloon-borne instrument called LITOS (Leibniz-Institute Turbulence Observations in the Stratosphere) has been developed to study turbulence in the stratospheric wind and temperature field down to the smallest spatial scales of millimeters. LITOS has been successfully launched two times from Kiruna (67 °N, 21 °E) and several times from the institute site in Kühlungsborn (54 °N, 12 °E). Since hot and cold wire techniques have never been used before on balloon platforms, laboratory measurements have been performed to verify their applicability for stratospheric conditions. The Kiruna flights show the intermittent structure of turbulence in the stratosphere. In addition, the results of a cluster algorithm reveal that more turbulent layers have been observed within the stratosphere than in the troposphere. On average the turbulent layers are only several ten meters thick. Furthermore, turbulent layers within the temperature field are typically thinner compared to layers in the wind field. Based on a modified theory, the energy dissipation rate has been determined with high precision, and detailed altitude profiles are obtained. The dissipation rates vary between 9.9×10^{-4} and 7.5×10^{-2} W/kg. The profiles reveal an increase of the energy dissipation rate with altitude. The mean energy dissipation rates unexpectedly differ between turbulence in the temperature and wind field. The values for the temperature profile are typically one to two orders of magnitude higher than for the wind profiles. To relate the turbulent layers to the atmospheric background conditions, the Richardson number has been determined. However, the analyses reveal that no direct relation between the Richardson number and turbulent layers has been found. The investigations of possible sources show that Kelvin-Helmholtz instabilities are the main source for some of the turbulent layer.

Zusammenfassung

Zur Untersuchung der stratosphärischen Turbulenz im Temperatur- und Windfeld auf kleinsten räumlichen Skalen von Millimetern wurde das neue ballongetragene Intrument LITOS entwickelt. Mehrere erfolgreiche Starts von LITOS erfolgten von Kühlungsborn (54 °N, 12 °O aus, sowie in 2008 und 2009 von Kiruna (67 °N, 21 °O) aus. Die LITOS Messtechniken wurden zuvor nicht für Ballonexperimente genutzt, aber die Anwendbarkeit für stratosphärische Bedingungen wurde in umfangreichen Laboruntersuchungen nachgewiesen. Die Beobachtungen der Flüge von Kiruna zeigt die große räumlich-zeitliche Variabilität der Turbulenz in der Stratosphäre. Die Ergebnisse eines Cluster-Verfahrens zeigen, dass in der Stratosphäre mehr turbulente Schichten erfasst wurden als in der Troposphäre. Im Mittel sind die turbulenten Schichten nur wenige zehn Meter dick. Die turbulenten Schichten im Temperaturfeld sind dabei im Mittel dünner als die Schichten im Windfeld. Auf der Basis einer weiterentwickelten Theorie wurden äußerst genaue Werte für die Energiedissipationsrate berechnet und detaillierte Höhenprofile erstellt. Die Dissipationsraten liegen zwischen 9.9×10^{-4} und 7.5×10^{-2} W/kg und steigen im Allgemeinen mit der Höhe an. Ein unerwarteter Unterschied zeigt sich zwischen der mittleren Dissipation der Temperatur und des Windes. Im Mittel liegen die Dissipationsraten der Temperatur ein bis zwei Größenordnungen über den Werten für den Wind. Der Zusammenhang der beobachteten Turbulenzschichten zur Hinter-

grundatmosphäre wurde mit Hilfe der Richardson-Zahl analysiert. Ein direkter Zusammenhang zwischen der Richardson-Zahl und dem Auftreten von Turbulenz konnte jedoch nicht nachgewiesen werden. Als eine der Hauptquellen für die beobachteten turbulenten Schichten konnten Kelvin-Helmholtz-Instabilitäten ermittelt werden.

Contents

Chapter 1

Introduction

Just 100 years ago, pioneering aerological experiments performed by Aßmann and Teisserenc de Bort led to the discovery of an unexpected phenomenon [*Assmann*, 1902; *Teisserenc de Bort*, 1902]. They observed a temperature increase above 10 km altitude and thus discovered the beginning of a new atmospheric layer - the stratosphere. In the following decades the technical progress enabled further research on the atmospheric structure above 10 km. The sum of all these measurements resulted in a temperature profile which allows a division of the atmosphere into specific layers as shown in Fig. 1.1.

The lowest part of the atmosphere extends to an altitude of $\sim$10 km and is called the troposphere. Within this layer the temperature decreases and due to the high amount of water vapor it is characterized by clouds and weather systems. The tropopause marks the transition between the troposphere and the stratosphere. The exact altitude of the tropopause varies with latitude and weather situation, while it typically reaches lower altitudes at the pole and higher altitudes towards the tropics.

The stratosphere is characterized by an increase of the temperature up to the stratopause at $\sim$50 km. Since this study focuses on measurements in the stratosphere, the characteristics of this altitude layer and some important phenomena will be described in more detail below. After the temperature has reached a maximum at the stratopause, the mesosphere begins and the temperature starts to decrease again. The mesosphere extends up to the mesopause in 86 - 105 km (depending on season), where the coldest temperature on Earth is found and phenomena like noctilucent clouds appear [e.g. *Gadsden and Schöder*, 1989]. Above the mesopause the temperature increases and the thermosphere begins.

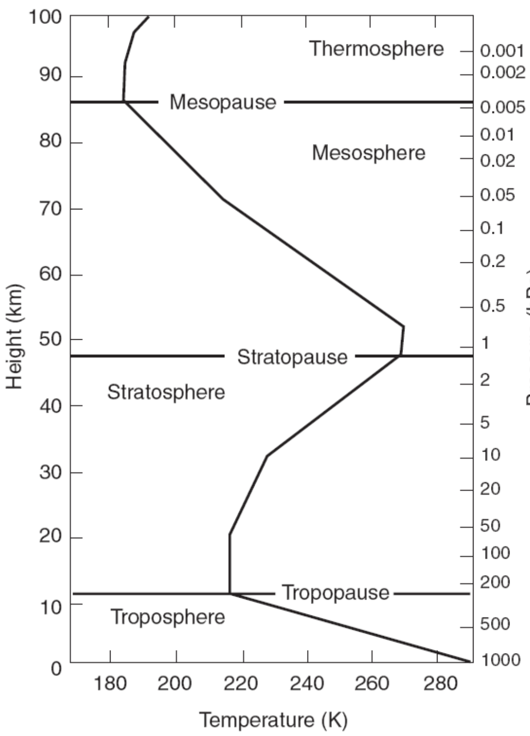

Figure 1.1.: Midlatitude mean temperature profile [from *Holton*, 2004].

As mentioned above, the temperature in the stratosphere increases with altitude, which is caused by the fact that ozone in the stratosphere absorbs the ultraviolet radiation coming from the sun. Almost 90% percent of the atmospheric ozone is found in the stratosphere leading to the increasing temperature [*Labitzke and van Loon*, 1999]. A global circulation within the stratosphere has been detected by Brewer [*Brewer*, 1949] and Dobson [*Dobson*, 1956]. Basically this residual circulation (or Brewer-Dobson circulation) consists of an upward motion from the troposphere into the stratosphere within the tropics, a poleward transport within the stratosphere and a downward motion in the middle and polar latitudes. By this circulation mass and trace gases are transported from the tropical tropopause to the extratropics [*Holton*, 2004]. The average time an air parcel needs to be transported from the tropical tropopause to a given location in the stratosphere is defined as the mean age of stratospheric air [*Engel et al.*, 2009]. So far, a wide discrepancy exists between observations of the age of stratospheric air and numerical models and further investigations are needed [*Waugh and Hall*, 2002; *Waugh*, 2009].
One of the most striking stratospheric phenomena has been discovered by Scherhag in 1952 [*Scherhag*, 1952]. A dramatic warming within a few days occurs during winter in the Northern Hemisphere (minor warming) which can be accompanied by a total change of the stratospheric circulation (major warming) [*Labitzke*, 1972]. Even though the described effects influence not only the stratosphere but also the atmospheric layers above and below, the stratosphere has long been underestimated within climate models. Instead it has solely been considered as a kind of upper border [*Labitzke and van Loon*, 1999]. But the role of the stratosphere changed fundamentally due to experimental and theoretical studies over the past two decades [*Gerber et al.*, 2012]. For instance, any long-term changes to stratospheric winds and temperatures possibly affect the surface climate and climate variability [*Baldwin et al.*, 2007]. Comprehensive climate simulations and experiments have revealed that the vertical coupling between the troposphere and stratosphere occur in both directions, e.g. changes in stratospheric ozone or temperature can lead to changes in the troposphere [*Labitzke and van Loon*, 1999]. Consequently, a better representation of the stratosphere is needed to improve weather forecasts and climate predictions [*Gerber et al.*, 2012]. However, there are still many stratospheric processes like the mean age of air, which are not or not fully understood and therefore further experiments and theoretical studies are needed in order to improve the understanding of the stratosphere.
Due to the small negative or even positive temperature gradient in the stratosphere, it is a region of stability and stratification. However, turbulence occurs because of breaking gravity waves or strong wind shears, which induce Kelvin-Helmholtz instabilities. Stratospheric turbulence appears on scales ranging from only millimeters up to several meters. Previous observations have shown that it occurs in thin isolated layers, also called “pancakes”, extending some ten or hundred meters in the vertical and some hundred kilometers in the horizontal [e.g. *Barat*, 1982a; *Sato and Woodman*, 1982]. The turbulent regions are separated vertically by sharp boundaries from the non-turbulent regions. Although turbulence and associated processes play a quite important role within many different aspects of the atmosphere, they have not been fully quantified or understood [e.g. *Wyngaard*, 1992; *Fritts et al.*, 2003]. In fact, almost all theoretical and numerical models dealing with atmospheric

circulation, dynamics, energetics and composition, must contain the effects of turbulence [*Gavrilov et al.*, 2005]. Even though turbulence in the stratosphere is weak on average compared to e.g. mesospheric turbulence [e.g. *Lübken*, 1992; *Hocking*, 1999], it nevertheless affects a large number of atmospheric processes. For instance, the energy transfer from the troposphere to the mesosphere is modified by energy dissipation within the stratosphere due to turbulence. Examinations of stratospheric turbulence is therefore not only important for understanding the stratosphere itself, but for understanding the energy budget of the whole middle atmosphere. Moreover, stratospheric turbulence is a potentially important process in the vertical mixing of trace species [e.g. *Lilly et al.*, 1974]. Besides the more scientific interests, turbulence in the troposphere and lower stratosphere can also be quite dangerous for aviation [*Sharman et al.*, 2012]. Probably everyone ever traveled by plane experienced the huge amount of energy connected with turbulence.
An important turbulence parameter for atmospheric models is the energy dissipation rate ε, i.e. the amount of energy dissipated into heat. In the stratosphere dissipation occurs at the very small scales of only some centimeters or even less. Remote sensing systems like radars, lidars and satellite-based sounders do not provide sufficient resolution to measure turbulence down to the smallest scales, or provide no signal at all in the middle stratosphere [e.g. *Gurvich and Brekhovskikh*, 2001; *Luce et al.*, 2002; *Engler et al.*, 2005; *Smalikho et al.*, 2005; *Sofieva et al.*, 2007]. In-situ measurements are typically performed either below 15 km with aircraft and tethered lifting systems [e.g. *Frehlich et al.*, 2003; *Siebert et al.*, 2007] or above 60 km with sounding rockets [e.g. *Lübken et al.*, 2002]. Thus in-situ high resolution balloon soundings still provide the only possibility for detailed observations of stratospheric turbulence. During the 1980s, pioneering work has been done by J. Barat and coworkers with balloon-borne ionic anemometers [e.g. *Barat*, 1982a; *Barat et al.*, 1984; *Dalaudier et al.*, 1989]. Their measurements resolved scales down to some ten centimeters. However, the higher the measurement resolution and therefore the precision is, the more exact results are obtained for the energy dissipation rate. But those soundings are technically challenging and up to now stratospheric soundings quantifying turbulence are rare. In fact a sub-centimeter resolution has not been achieved yet.

1.1. Overview

The aim of this study is to examine turbulence in the stratosphere with a new balloon-borne instrument down to the smallest scales for the first time. In Chapt. 2 theories and terminologies relevant for the analysis of turbulence measurements with will be briefly described. Additionally, a statistical method will be presented, which allows the exact determination of the energy dissipation rate based on measured spectra of velocity or temperature fluctuations. The measurement method as well as the new balloon-borne instrument itself will be described in Chapt. 3. This chapter also includes the results of laboratory experiments performed to prove the applicability of the sensors for stratospheric conditions. In Chapt. 4 the turbulence observations of LITOS will be presented and with the help of a developed cluster algorithm characteristics of the turbulent layers are determined. Furthermore the turbulent spectra are analyzed in order to retrieve altitude profiles of the energy dissipation rate. Chap. 5 describes the relation of the turbulence observations to the geophysical background conditions and discusses possible source of the turbulent layers. Finally, Chapt. 6 contains a summary of the most important results and an outlook. The appendices include detailed mathematical descriptions or further figures of the observations.

Chapter 2

Theoretical description of turbulent flows

Turbulence is omnipresent, since most flows in nature and engineering applications are turbulent [e.g. *Tennekes and Lumley*, 1985]. However, after decades of turbulence investigations, a comprehensive understanding of this phenomenon is still missing and it continues to be one main issue in physical researches [e.g. *Frisch*, 1995; *Pope*, 2006]. Turbulence measurements in the atmosphere are analyzed based on theoretical assumptions, which will be shortly introduced in the following. Thereby, the main focus lies on the description of theories and terminologies relevant for the analysis of turbulence measurements with LITOS. A more detailed and general review of turbulence theories can be found in standard literature e.g. [*Hinze*, 1959; *Tennekes and Lumley*, 1985; *Lesieur*, 1997; *Pope*, 2006]. The first section includes a short description of turbulence characteristics and definitions of relevant parameters. In Sec. 2.2 the main aspects of the statistical theory of turbulence will be presented. A method will be described, which allows the exact determination of the energy dissipation rate on basis of the measured spectra of velocity or temperature fluctuations.

2.1. Characteristics of turbulent flows

Due to the complexity of turbulent flows, it is not feasible to give a precise definition of turbulence itself. Alternatively, a list of most important characteristics has been summarized from e.g. *Tennekes and Lumley* [1985]; *Lesieur* [1997] and *Pope* [2006]. Accordingly, turbulence

- is unpredictable and chaotic in space and time
- is a formation of eddies
- appears, if inertial forces prevail viscous forces
- transports and mixes effectively momentum, kinetic energy, and contaminants like heat, particles, and moisture
- is dissipative
- extends over a wide scale range.

Apart from these characteristics, different parameters have been stated determining the transition from laminar to turbulent flows as well as describing the turbulent flow itself. Since some parameters are relevant for the understanding of turbulence theory and the measurement analyses, they are shortly presented in the next section.

2.1.1. Parameters to describe turbulent flows

As described above, turbulence appears if inertial forces prevail viscous forces. The ratio between these two forces is described by the so called **Reynolds number**, which is given by [*Tatarskii*, 1961]:

$$Re = vL/\nu \tag{2.1}$$

where v, L, and ν are the velocity, characteristic length (characterizes the dimension of the flow) and kinematic viscosity, respectively. A laminar flow is stable as long as the Reynolds number does not exceed a critical value. Once, Re gets larger than its critical value (e.g. the velocity of the fluid increases), the motion becomes unstable and turbulence arises from instabilities [*Tatarskii*, 1961; *Tennekes and Lumley*, 1985].
Within the atmosphere it can be observed that the critical Reynolds number is mostly exceeded within the troposphere. Therefore, turbulence with different intensity can be found anywhere in this altitude range. Going higher up, the Reynolds number decreases, since the viscous forces increase. Hence, above a certain altitude, the viscous forces dominate and will damp efficiently turbulent fluctuations.

Theoretical descriptions of turbulence production lead to the turbulent kinetic energy equation (TKE). The TKE equation contains different terms of turbulence generation, namely terms for mechanical production, buoyant production (or loss), frictional dissipation and for redistribution by transport and pressure forces. Considering the relation between buoyant and mechanical production, another important turbulence parameter, the **flux Richardson number** is defined:

$$Ri_{\mathrm{f}} = \frac{\overline{w'T'}\ (\frac{g}{T})}{\overline{u'w'}\ \frac{\delta\overline{u}}{\delta z}} \tag{2.2}$$

where u', w' are the fluctuating horizontal and vertical wind components, T' are the temperature fluctuations, T and $\overline{u}$ are the mean temperature and the mean horizontal wind. Due to difficulties in obtaining the flux Richardson number, the gradients of potential temperature and horizontal wind are usually assumed to be proportional to the mean flux of temperature $\overline{w'T'}$ and momentum $\overline{u'w'}$ [*Tennekes and Lumley*, 1985]. Thus the **gradient Richardson number** is used instead:

$$Ri = \frac{\frac{g}{\theta}\,\frac{\delta\theta}{\delta z}}{\left(\frac{\delta\overline{u}}{\delta z}\right)^2} = \frac{N_{\mathrm{B}}^2}{S^2} \tag{2.3}$$

where N_B^2 is the Brunt-Väisälä frequency and S^2 is the wind shear. A common assumption is that if Ri becomes negative, the production of turbulent kinetic energy increases and the atmosphere is statically unstable. Whereas positive values of Ri indicate that kinetic energy is lost and the atmosphere becomes stably stratified. Turbulence will be completely suppressed, when positive Ri gets large enough [*Tennekes and Lumley*, 1985]. More precisely, from linear theory it is suggested that turbulence cannot be maintained above a critical Richardson number $Ri_\mathrm{c} = 1/4$. Only if Ri becomes smaller than Ri_c, the mechanical production is intense enough to maintain turbulence in a stable layer [*Holton*, 2004]. But once created, turbulence may sustain up to $Ri \sim 1$. However, the existence of such a critical Richardson number has recently been questioned [e.g. *Achatz*, 2005, 2007; *Galperin et al.*, 2007; *Balsley et al.*, 2008]. Observations have shown that turbulent motions occur far beyond any critical Richardson number predicted by linear theory [e.g. *Mauritzen and Svensson*, 2007]. In Sect. 5.2 measurement results will be shown and the existence of a critical Richardson number Ri_c will be discussed.

2.1.2. Energy cascade, spectrum and Kolmogorov hypothesis

Once turbulence is initiated, the so called energy cascade takes place linking all scales of motion within a turbulent flow. Based on the dominating physical processes, this cascade is divided in its typical subranges and each subrange can be described by a specific form of the corresponding energy spectrum. Generally, the energy spectrum represents the averaged turbulent kinetic energy TKE per unit mass [*Tatarskii*, 1971; *Pope*, 2006]:

$$TKE = \int_0^\infty E(k)\mathrm{d}k \tag{2.4}$$

where k is the wavenumber. A second main quantity in this context is the rate of energy dissipated into heat by molecular viscosity. The so called energy dissipation rate ε is related to $E(k)$ by [*Pope*, 2006]:

$$\varepsilon = \int_0^\infty 2\nu E(k)\mathrm{d}k \tag{2.5}$$

with ν = kinematic viscosity.

Figure 2.1 presents a turbulent energy spectrum with its subranges and their intersections. At the beginning of the energy cascade (small wave numbers), primary instabilities extract energy from the ambient flow. Thus the large eddies are determined by the mean flow field and boundary conditions.
The resulting **buoyancy subrange** is dominated by buoyant forces and the form of the energy spectrum is solely related to the Brunt-Väisälä frequency N_B^2:

$$E(k) \propto N_B^2\ k^{-3}. \tag{2.6}$$

While producing secondary motion, those instabilities become unstable themselves and transfer their energy to smaller eddies [*Tennekes and Lumley*, 1985]. These smaller eddies undergo

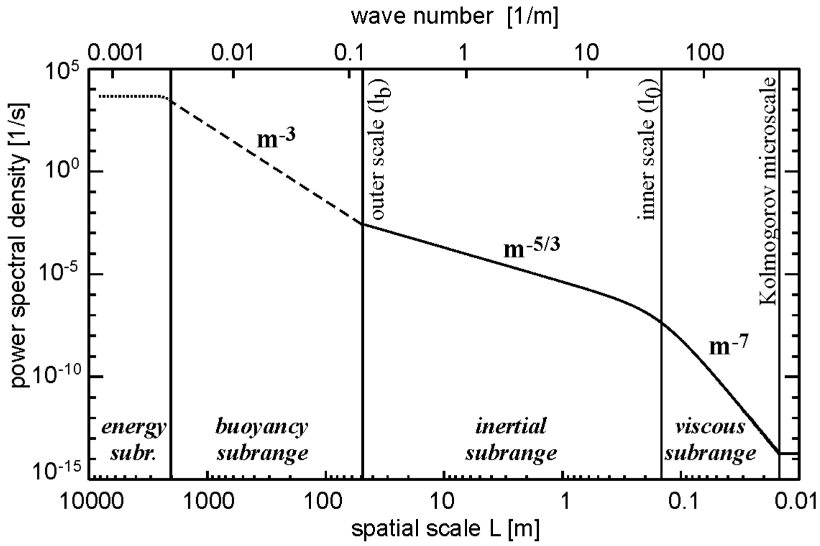

Figure 2.1.: Theoretical turbulent spectrum for 20 km altitude with typical slopes of m^{-3}, $m^{-5/3}$ and m^{-7} for the buoyancy, the inertial and the viscous subrange. The transition between the subranges are called the outer scale l_b and the inner scale l_0. The Kolmogorov microscale characterizes the smallest, dissipative eddies at the end of the viscous subrange. Spectrum is calculated based on *Lübken et al.* [1993].

a similar break-up process and consequently transfer their energy to even smaller eddies, i.e. higher wave numbers [*Pope*, 2006]. The transfer of energy to smaller eddies is the dominating physical process in the inertial subrange of the turbulent spectrum. Here, the motions are solely determined by inertial forces. Any viscous and buoyant effects are negligible and no energy is added by the mean flow or taken out by viscous dissipation. As the relation between the inertial forces to viscous forces is presented by the Reynolds number (2.1), an inertial subrange can only emerge if *Re* is large enough, typically larger than 1000 [*Tennekes and Lumley*, 1985]. Accordingly, the inertial range expands as the Reynolds number increases. Furthermore, Kolmogorov stated in his second similarity hypothesis, that in every turbulent flow at sufficiently high Reynolds number, the statistics of motion in the inertial subrange are determined uniquely by ε, independent of ν [*Pope*, 2006]. Thus, from dimensional reasoning the form of the energy spectrum in the **inertial subrange** is given by [*Tennekes and Lumley*, 1985]:

$$E(k) \propto \varepsilon^{2/3} k^{-5/3}. \tag{2.7}$$

The subrange is limited by the so called outer scale l_b to the buoyancy subrange and by the inner scale l_0 to the viscous subrange. Both transition scales depend on the rate of energy dissipation ε and this relation will be used later in Sect. 2.2.5.

Finally, at very large wave numbers, within the **viscous subrange**, energy is dissipated into heat by molecular viscosity. Based on similarity considerations, the form of the energy spectrum is expected to be [*Heisenberg*, 1948]:

$$E(k) \propto k^{-7}. \tag{2.8}$$

As the directional information of small wave numbers are lost as the energy passes down the cascade, all information about the geometry of the large eddies are also lost. Consequently, the statistics of the motions at scales smaller than the inner scale l_0 have a universal form determined uniquely by ν and ε [*Pope*, 2006]. This assumption constitutes the first similarity hypothesis of Kolmogorov, which states basically that in every high-Reynolds-number turbulent flow, the statistics of small-scale motions are in a sense universal. Based on the first hypothesis, the **inner scale** l_0 can be defined, because there is only one combination of ε and ν which has the dimension of length [*Tatarskii*, 1971]:

$$l_0 = \sqrt[4]{\frac{\nu^3}{\varepsilon}}. \tag{2.9}$$

Summarizing, the downward energy cascading is quite important, because it means that the dissipation of energy at the end of the process is determined by the amount of energy available at the beginning of the cascade.

2.2. Statistical description of turbulence

Since turbulent flows are unpredictable and chaotic in space and time, statistical methods are expedient for turbulence analyses.
Basically, the two mostly applied methods are the structure function and the determination of the power spectral density. Both methods are usually applied to obtain turbulence parameters like the energy dissipation rate ε. Hence, a short description of the structure functions will be followed by the explanation of the power spectral density method.

2.2.1. Structure function

Within turbulence theory, meteorological quantities like temperature and wind are described by so called random functions or random fields. More specifically, the temperature is defined as a scalar random field, whereas the wind is a vector random field comprising three random velocity components. Before starting with the description of the structure function, it is necessary to introduce some definitions for the random field as they are fundamental for turbulence theory. Provided that all statistics of such a random field are invariant under a shift in time, it is called statistical **stationary** [*Pope*, 2006].
Similarly, in the case that the statistics are independent of position, i.e. the mean value of the quantity is uniform, the random field is called statistical **homogeneous** [*Tennekes and Lumley*, 1985]. It should be pointed out, that only the statistics are independent of position, whereas the components of a quantity can certainly vary in all three coordinate directions and time.

If a homogeneous random field is invariant under rotations and reflections of the coordinate system, then it is statistically **isotropic**.
A first important characteristic of the random field, also called Reynolds decomposition, is the separation into a (slowly varying) mean and the corresponding fluctuations. Apart from the Reynolds decomposition, the correlation function $B(\vec{r}_1, \vec{r}_2)$ is an important characteristic of the random field $f(\vec{r})$ [*Tatarskii*, 1961]:

$$B(\vec{r}_1, \vec{r}_2) = \overline{[f(\vec{r}_1) - \overline{f(\vec{r}_1)}]\,[f(\vec{r}_2) - \overline{f(\vec{r}_2)}]}. \tag{2.10}$$

The correlation function determines, whether the random field of e.g. velocity fluctuations is statistically dependent or independent at two different points r_1 and r_2. To derive further statistical characteristics of the turbulent field, it is usually assumed to be homogeneous and isotropic. Here the problem is, that meteorological fields are typically functions of altitude or time containing large scale variations which destroy homogeneity and isotropy.
However, on small enough spatial scales the turbulent field can be considered to be homogeneous and isotropic. More precisely, if the distance between two points $\vec{r}_1$ and $\vec{r}_2$ of the field $f(\vec{r})$ is not too large, the largest inhomogeneities have no effect on the difference $f(\vec{r}_1) - f(\vec{r}_2)$ and Kolmogorov therefore defined the so-called structure function [*Tatarskii*, 1961]:

$$D(\vec{r}_1, \vec{r}_2) = \overline{[f(\vec{r}_1) - f(\vec{r}_2)]^2}. \tag{2.11}$$

The structure function describes basically the covariance of the difference between the two points r_1 and r_2. The underlying concept of the structure function is the definition of local homogeneity: If the mean value and the structure function of a random field in a region G depend only on $\vec{r}_1 - \vec{r}_2$ for all $\vec{r}_1, \vec{r}_2$ in G, the field is called **locally homogeneous** [*Tatarskii*, 1971]. Providing that the structure function depends only on $|\vec{r}_1 - \vec{r}_2|$, the field is called **locally isotropic**.
Since turbulence observations with LITOS are obtained within the velocity field as well as within the temperature field, their specific structure functions will be shortly described in the following.

2.2.2. Velocity structure function in the inertial and viscous subrange

The vector random field of velocity $v(\vec{r})$ is composed of nine structure functions consisting of the different components in the x, y and z axes of the velocity vector [*Tatarskii*, 1961]:

$$D_{ik}(\vec{r}) = \overline{(v_i - v_i')(v_k - v_k')} \tag{2.12}$$

with $i, k = 1, 2, 3$. For a locally isotropic velocity field, the structure function can be defined as:

$$D_{ik}(\vec{r}) = [D_{ll}(r) - D_{tt}(r)]\; n_i n_k + D_{tt}(r)\delta_{ik} \tag{2.13}$$

where δ_{ik} is the Kronecker delta and n_i, n_k are components of the unit vector in direction of $\vec{r}$. D_{tt} is the transversal structure function and D_{ll} the longitudinal structure function. After solving Eq. 2.13 over i, k by considering the expansion of the transversal and longitudinal structure function, it follows for the "total" structure function [*Tatarskii*, 1971]:

$$D_{ii}(\vec{r}) = D_{\text{tot}}(\vec{r}) = D_{ll}(r) + 2D_{tt}(r) \tag{2.14}$$

For the **inertial subrange** of the turbulent spectrum, Kolmogorov deduced from dimensional combinations that [*Tatarskii*, 1971]:

$$D_{ll}(r) = C_V^2\ \varepsilon^{2/3}\ r^{2/3} \tag{2.15}$$

where C_V is a dimensionless constant also called the structure function constant and ε is the energy dissipation rate. This famous relation is also called **2/3rd law of Kolmogorov and Oboukhov**. Inserting this definition for $D_{ll}(r)$ in 2.14, an expression for the transversal component is obtained [*Tatarskii*, 1971]:

$$D_{tt}(r) = \frac{4}{3}C_V^2\ \varepsilon^{2/3}\ r^{2/3} \tag{2.16}$$

as well as for the total structure function for the inertial subrange:

$$D_{\text{tot}}(r) = \frac{11}{3}C_V^2\ \varepsilon^{2/3}\ r^{2/3}. \tag{2.17}$$

Within the viscous subrange, following the first similarity hypothesis of Kolmogorov, the statistics of motions are solely determined by the kinematic viscosity ν and the energy dissipation rate ε (see Sect. 2.1.2). Hence, the structure functions for the **viscous subrange** for both velocity components can be obtained [*Pope*, 2006]:

$$D_{ll}(r) = \frac{1}{15}\frac{\varepsilon}{\nu}\ r^2, \tag{2.18}$$

$$D_{tt}(r) = \frac{2}{15}\frac{\varepsilon}{\nu}\ r^2. \tag{2.19}$$

With Eq. 2.14 the total structure function within the viscous subrange is defined as:

$$D_{\text{tot}}(r) = \frac{1}{3}\frac{\varepsilon}{\nu}\ r^2. \tag{2.20}$$

2.2.3. Temperature structure function in the inertial and viscous subrange

In contrast to the vector field of the wind velocity, the temperature is a scalar field and can be approximately regarded as a conservative passive tracer. This means, that it has no effect on the dynamical regime of the flow (passive) and it only changes due to turbulent motion (conservative). The structure function of temperature fluctuations within the inertial subrange depends on ε, r and one external parameter N, characterizing the intensity of fluctuations.

Dimensional reasoning then determines the structure function in the **inertial subrange** [*Tatarskii*, 1971]:

$$D_T(r) = C_T^2 r^{2/3} = \frac{a^2 N}{\varepsilon^{1/3}}\ r^{2/3} \tag{2.21}$$

with a = numerical constant.
Analog to the structure function of the velocity field in the viscous subrange, the structure function of the temperature field depends on two quantities only. Instead of the energy dissipation rate the parameter N is used and the kinematic viscosity is replaced by the thermal diffusion coefficient χ. Accordingly, it follows for the structure function in the **viscous subrange** [*Tatarskii*, 1971]:

$$D_T(r) = \frac{1}{3}\frac{1}{f_\alpha}\frac{N}{\chi}\ r^2. \tag{2.22}$$

The factor $1/f_\alpha$ goes back to *Lübken* [1993] in order to account for different normalizations of N.
A short summary of the specific structure functions for velocity and temperature fluctuations can be found in Table 2.1.

Table 2.1.: Structure functions for velocity and temperature fluctuations within the inertial and viscous subrange of the turbulent spectrum.

	velocity	temperature
inertial subrange	$D_{tot}(r) = \frac{11}{3} C_V^2 \varepsilon^{2/3} r^{2/3}$	$D_T(r) = C_T^2 r^{2/3}$
viscous subrange	$D_{tot}(r) = \frac{1}{3}\frac{\varepsilon}{\nu} r^2$	$D_T(r) = \frac{1}{3}\frac{1}{f_\alpha}\frac{N}{\chi} r^2$

2.2.4. Inner scale derived from structure function of temperature fluctuations

As mentioned before, one main goal of turbulence statistics is the determination of parameters like the inner scale l_0 to describe the turbulent motion.
The inner scale is often defined as the intersection of the asymptotic form of the structure function in the inertial and viscous subrange [*Lübken*, 1993]. For instance, the relation of Eq. 2.21 and Eq. 2.22 gives for temperature fluctuations (with $r = l_0$):

$$l_0 = \left(\frac{3 f_\alpha C_T^2 \chi}{N}\right)^{3/4}. \tag{2.23}$$

Accordingly, to obtain the inner scale, C_T^2 has to be determined from turbulence measurements within the inertial subrange (see Eq. 2.21). This, in turn, reveals the major drawback

of the structure function method. It is not possible to obtain ε alone from measurements. Instead only the combination $C_T^2 = a^2 N/\varepsilon^{1/3}$ can be specified. Together with the uncertainties in the constants (e.g. a^2, f_α), rather imprecise values for l_0 can be attained.
Owing to this uncertainty, an alternative method which determines directly the inner scale has been introduced by *Lübken* [1992] and subsequent publications.

2.2.5. Spectral method

In this section the alternative method to determine precisely the inner scale and therewith the energy dissipation rate stated by *Lübken* [1992]; *Lübken et al.* [1993] and *Lübken* [1993] is considered. The method includes a spectral model describing the inertial and viscous subrange of the turbulent energy spectrum. Within their studies, they used two different models, namely the Heisenberg and the Tatarskii model. As the Heisenberg model is numerically more stable it has been preferred in the turbulence analyses and the main aspects of the analysis method will now shortly be presented. It should be noted, that the method of *Lübken* [1992]; *Lübken et al.* [1993] and *Lübken* [1993] has been formulated for density fluctuations. Since only velocity and temperature fluctuations are measured with LITOS and not density fluctuations, certain equations had to be modified.
Therefore, the method has been recalculated in order to adapt it to velocity and temperature fluctuations.
The 1-dimensional model W by *Heisenberg* [1948] exhibits an $k^{-5/3}$ power law in the inertial subrange and a smooth transition to the k^{-7} slope in the viscous subrange. It is given by:

$$W(\omega) = \frac{\Gamma(5/3)\sin(\pi/3)}{2\pi v_\mathrm{b}}\, C^2\, \frac{(\omega/v_\mathrm{b})^{-5/3}}{\left[1+(\omega/v_\mathrm{b}/k_0)^{8/3}\right]^2} \tag{2.24}$$

where Γ is the Gamma function ($\Gamma(5/3) = 0.90167$), v_b is the balloon velocity, $\omega = 2\pi f$ the cyclic frequency, and C^2 the structure function constant. The Heisenberg model "breaks" at k_0, which is the intersection of the asymptotic form of $W(\omega)$ in the inertial and viscous subrange. *Tatarskii* [1971] has shown that k_0 is determined from the behavior of the structure function D at the origin.
Therefore, to proceed, a relation between the structure function and the 1-dimensional power spectrum W is needed. Based on the Wiener-Khinchine's theorem the Fourier transform of the correlation function $B(\vec{r})$ (Eq. 2.10) is equal to the 3-dimensional power spectrum $\Phi(\vec{k})$. As the correlation function can be expressed in terms of the structure function, one obtains [*Tatarskii*, 1971]:

$$D(\vec{r}) = 2\int_{-\infty}^{\infty}\int_{-\infty}^{\infty}\int_{-\infty}^{\infty}\left[1-\cos\vec{k}\vec{r}\right]\Phi(\vec{k})\mathrm{d}^3k. \tag{2.25}$$

If the turbulent field is isotropic, after introducing spherical coordinates in $\vec{k}$-space and integrating over angular variables, Eq. 2.25 takes the form [*Tatarskii*, 1971]:

$$D(r) = 8\pi\int_0^{\infty}\left(1-\frac{\sin kr}{kr}\right)\Phi(k)k^2\mathrm{d}k. \tag{2.26}$$

The next step is the conversion of the 1-dimensional spectrum of Heisenberg $W(\omega)$ into the 3-dimensional spectrum $\Phi(k)$. In order to do this, the time i.e. frequency domain of the Heisenberg spectrum must be related with the wavenumber domain of the spatial spectrum. Usually, an instrument is passing a turbulent field rather rapidly and measures the turbulent fluctuations as a function of time. *Taylor* [1938] assumes in his **frozen field hypothesis**, that during the time of measurement, the turbulent field does not change appreciably [*Tennekes and Lumley*, 1985]. Consequently, k is substituted with ω/v_{b} and the following relation between the 3-dimensional spectrum (Eq. 2.26) and the 1-dimensional frequency spectrum $W(\omega)$ (Eq. 2.24) is derived:

$$\Phi(k) = -\frac{v_{\mathrm{b}}^2}{2\pi k} \cdot \frac{d}{d\omega} W(\omega) \tag{2.27}$$

where v_{b} represents the balloon velocity, i.e. the speed by which the instrument is moved. Using condition 2.27, one arrives at the following form for the 3-dimensional Heisenberg spectrum:

$$\Phi(k) = \frac{\Gamma(5/3)\sin(\pi/3) \cdot C^2}{4\pi^2} \cdot \frac{5}{3} k^{-\frac{11}{3}} \cdot \frac{1 + \frac{21}{5}(k/k_0)^{\frac{8}{3}}}{\left\{1 + (k/k_0)^{\frac{8}{3}}\right\}^3}. \tag{2.28}$$

A detailed derivation of the 3-dimensional form of the 1-dimensional Heisenberg spectrum can be found in the Appendix A.
As mentioned above, k_0 is determined from the behavior of the structure function D at the origin [*Tatarskii*, 1971]. Therefore Eq. 2.26 forms to:

$$\frac{d^2}{dr^2} D(0) = \frac{8\pi}{3} \int_0^\infty \Phi(k) k^4 \mathrm{d}k. \tag{2.29}$$

Using this relation, the inner scale and therewith the energy dissipation rate are derived in the next section.

2.2.6. Inner scale for velocity fluctuations derived from Heisenberg spectrum

Based on the detailed recalculation, the method of *Lübken* [1992]; *Lübken et al.* [1993] and *Lübken* [1993] is now adapted to velocity and temperature fluctuations. Due to the fact, that the structure functions in the viscous subrange differ for temperature and velocity fluctuations, two different equations for the inner scale of the spectrum has to be derived.
Beginning with velocity fluctuations, the structure function within the viscous subrange is given by (2.20):

$$D_{\mathrm{tot}}(r) = \frac{1}{3} \frac{\varepsilon}{\nu} r^2$$

where ε is the energy dissipation rate and ν is the kinematic viscosity.
Inserting this equation and Eq. 2.28 in Eq. 2.29 yields the relation:

$$\begin{aligned}\frac{d^2}{dr^2}D(0) = \frac{2}{3}\frac{\varepsilon}{\nu} = \frac{8\pi}{3}\int_0^\infty \frac{\Gamma(5/3)\sin(\pi/3)\cdot C_V^2}{4\pi^2}\cdot\frac{5}{3}k^{-\frac{11}{3}}\cdot\frac{1+\frac{21}{5}(k/k_0)^{\frac{8}{3}}}{\left\{1+(k/k_0)^{\frac{8}{3}}\right\}^3}\mathrm{d}k \\ = \frac{10\,\Gamma(5/3)\sin(\pi/3)C_V^2}{9\pi}\int_0^\infty\frac{1+\frac{21}{5}(k/k_0)^{\frac{8}{3}}}{\left\{1+(k/k_0)^{\frac{8}{3}}\right\}^3}k^{\frac{1}{3}}\mathrm{d}k.\end{aligned} \tag{2.30}$$

After integration and rearranging for k_0 it follows (see App. B):

$$k_0^{\frac{4}{3}} = \frac{16\,\varepsilon}{9\,\Gamma(5/3)\,\sin(\pi/3)\,C_V^2\,\nu}. \tag{2.31}$$

With the definition of the structure function constant for velocity fluctuations $C_V^2 = 4\alpha\cdot\varepsilon^{2/3}$ [*Barat and Bertin*, 1984b] and the empirical constant $\alpha = 0.5$ [*Antonia et al.*, 1981; *Bertin et al.*, 1997] one obtains:

$$k_0^{\frac{4}{3}} = \frac{8\,\varepsilon^{1/3}}{9\,\Gamma(5/3)\,\sin(\pi/3)\,\nu}. \tag{2.32}$$

Finally, by inserting $\Gamma(5/3) = 0.9027$ and using $l_0 = 2\pi/k_0$ the inner scale for velocity fluctuations is defined:

$$l_0^V = 2\pi\left(\frac{9\cdot 0.9027\cdot\sin(\pi/3)}{8}\cdot\frac{\nu}{\varepsilon^{1/3}}\right)^{3/4} = 5.7\cdot\left(\frac{\nu^3}{\varepsilon}\right)^{\frac{1}{4}}. \tag{2.33}$$

Here, another important parameter in turbulence theory has been obtained, namely the **Kolmogorov microscale**:

$$\eta = \left(\frac{\nu^3}{\varepsilon}\right)^{\frac{1}{4}} \tag{2.34}$$

which characterizes the very smallest, dissipative eddies [*Pope*, 2006]. Therewith, a relation between the inner scale for the spectrum of velocity fluctuations and the Kolmogorov microscale is stated:

$$l_0^V/\eta = 5.7. \tag{2.35}$$

2.2.7. Inner scale for temperature fluctuations derived from Heisenberg spectrum

Similarly, the inner scale for the spectrum of temperature fluctuations can be determined. The structure function in the viscous subrange is given by (2.22):

$$D(r) = \frac{1}{f_\alpha}\frac{1}{3}\frac{N}{\chi}r^2 \tag{2.36}$$

where the parameter N characterizes the intensity of fluctuations (similar to ε for velocity fluctuations) and χ is the thermal diffusion coefficient. The factor $1/f_\alpha$ accounts for different normalizations of N. For temperature fluctuations f_α is taken as 2.
Inserting Eq. 2.36 and the 3-dimensional form of the Heisenberg spectrum (Eq.2.28) in the relation Eq. 2.29 leads to:

$$\frac{d^2}{dr^2}D(0) = \frac{1}{3}\frac{N}{\chi} = \frac{10\,\Gamma(5/3)\sin(\pi/3)C_T^2}{9\pi}\int_0^\infty \frac{1+\frac{21}{5}(k/k_0)^{\frac{8}{3}}}{\left\{1+(k/k_0)^{\frac{8}{3}}\right\}^3}k^{\frac{1}{3}}\mathrm{d}k. \tag{2.37}$$

Again, after integration and solving the equation for k_0 one obtains:

$$k_0^{\frac{4}{3}} = \frac{8\,N}{9\,\Gamma(5/3)\,\sin(\pi/3)\,C_T^2\,\chi}. \tag{2.38}$$

The structure function constant for temperature fluctuations is defined as $C_T^2 = \alpha^2 N/\varepsilon^{1/3}$, where α^2 is a numerical constant [*Tatarskii*, 1971; *Lübken et al.*, 1993]. Inserting in Eq. 2.38 yields (equal to Eq. 2.32 for velocity fluctuations):

$$k_0^{\frac{4}{3}} = \frac{8\,N}{9\,\Gamma(5/3)\,\sin(\pi/3)\,\alpha^2\,N/\varepsilon^{1/3}\,\chi}. \tag{2.39}$$

Replacing χ with the molecular Prandtl number $Pr^{\mathrm{mol}} = \nu/\chi$ [*Tennekes and Lumley*, 1985] yields:

$$k_0^{\frac{4}{3}} = \frac{8\,Pr^{mol}\,\varepsilon^{\frac{1}{3}}}{9\,\alpha^2\,\Gamma(5/3)\,\sin(\pi/3)\,\nu}. \tag{2.40}$$

Thus, using the relation $l_0 = 2\pi/k_0$, the inner scale for temperature fluctuations l_0^T is given by:

$$l_0^T = 2\pi\cdot\left(\frac{9\,a^2\,\Gamma(5/3)\,\sin(\pi/3)}{8\,Pr^{mol}}\right)^{\frac{3}{4}}\cdot\left(\frac{\nu^3}{\varepsilon}\right)^{\frac{1}{4}} \tag{2.41}$$

With $\alpha^2 = 1.74$, $\Gamma(5/3) = 0.9027$ and $Pr^{mol} = 0.73$ a relation between the inner scale for the spectrum of temperature fluctuations and the Kolmogorov microscale is given by:

$$l_0^T = 10.9\cdot\left(\frac{\nu^3}{\varepsilon}\right)^{\frac{1}{4}} \quad \text{or} \quad \mathrm{l}_0^{\mathrm{T}}/\eta = 10.9. \tag{2.42}$$

Using these definitions for the inner scale l_0^T and l_0^V, energy dissipation rates from measured spectra of temperature and velocity fluctuations obtained with the new balloon borne instrument LITOS can be determined. The data processing and the results achieved will be presented in Chap. 4 and 5, respectively.

Chapter 3

Measurement method of LITOS

As described in Sect. 2.2.5, for the precise determination of energy dissipation rates, the determination of the inner scale l_0 is essential. Within the stratosphere, spatial scales of l_0 are in the range of only a few centimeters. Such a high measurement resolution can only be achieved by in-situ soundings. Earlier in-situ soundings measured only down to scales of some ten centimeters, i.e. they do not resolve the inner scale [e.g. *Barat*, 1982a]. Therewith, a new light-weight, compact balloon-borne instrument called LITOS (Leibniz-Institute Turbulence Observations in the Stratosphere) has been developed at the IAP. The instrument is designed for investigations of small-scale turbulent fluctuations in the temperature and wind field. Achieving a measurement resolution of at least 2.5 mm, the entire turbulence spectrum down to the viscous subrange in the stratosphere is studied for the first time. So far, LITOS has been launched successfully several times from the institute site in Kühlungsborn (54° N, 12° E) as a stand-alone payload. During two BEXUS campaigns (Balloon-borne EXperiments for University Students) in 2008 and 2009 from Kiruna (67° N, 21° E), LITOS has been integrated into a bigger gondola for stratospheric balloons.
Section 3.1 describes the instrument in more detail including the applied measurement technique. As the technique has never been used before within the stratosphere, laboratory measurements were performed to study its general behavior and applicability. The results are presented in Sect. 3.2, respectively. Finally, in Sect. 3.3, the implementation of LITOS in a small gondola for launches from normal weather balloon stations, as well as a LITOS version for the BEXUS gondola, i.e. stratospheric balloon launches are described.

3.1. General measurement principle of LITOS

LITOS has been developed for balloon-borne in-situ studies of small-scale velocity and temperature fluctuations. To observe velocity fluctuations a Constant-Temperature-Anemometer (CTA) also called hot-wire is used, where the measurement principle is based on convective cooling caused by the air flow passing a constantly heated thin wire. Temperature fluctuations are measured with a Constant-Current-Anemometer (CCA) or also called cold-wire, which operates basically as a thermistor. Both techniques are well known and used widely for flow measurements in gases and liquids in laboratory studies. The small instrument size and its light weight make them particularly suitable for balloon-borne measurements. But, they have never been applied on balloon platforms yet. Hence, additional laboratory measurements are required (see Sect. 3.2). Another advantage besides the size and weight, are the combination of a fast frequency response (up to several hundred kilohertz) of CTA/CCA systems and the slow ascending rate of a balloon. Therewith, a very high spatial measurement resolution of at least 2.5 mm is achieved. Additionally, CTA as well as CCA cover a wide range of velocity and temperature values. One disadvantage of CTA or CCA systems for field observations is the fragility of the sensor elements, which requires a certain carefulness during the launch procedure. However, the advantages predominate and convincingly results of stratospheric turbulence are obtained (described in Chapt. 4 and 5). As mentioned above, there exist two measurement methods: the constant-temperature mode (CTA) and the constant-current mode (CCA). Both methods will be described more precisely below.

3.1.1. Constant-Temperature-Anemometer for velocity observations

Generally, due to its large diameter, the balloon follows the ambient wind field during the ascent phase (see Fig. 3.1). Accordingly, the payload at altitude z is also following the wind field at balloon height $\vec{v}(z+h)$. Hence, any variation of the wind velocity results in a difference $\Delta\vec{v}$ between the wind vectors at balloon height $\vec{v}(z+h)$ and at payload height $\vec{v}(z)$. Conversely, for a wind constant with altitude, the effective horizontal flow or velocity difference at payload height is zero. Consequently, with the LITOS sensor at payload height an altitude profile of the wind differences $\Delta\vec{v}$ is obtained. The term *wind* will be used hereafter for the measured quantity instead of *wind difference* or *effective flow*.

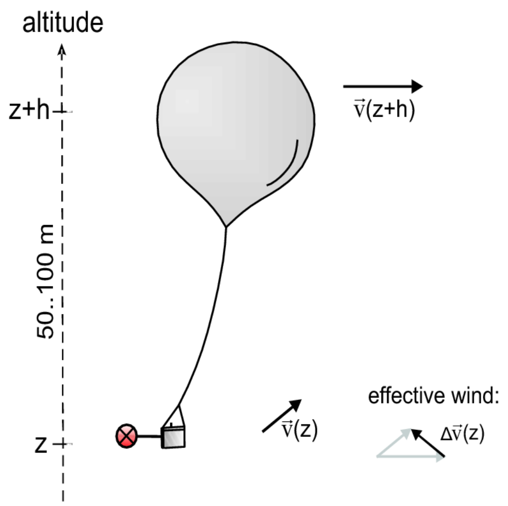

Figure 3.1.: Schematic drawing of the principle of balloon-borne wind turbulence soundings. The LITOS sensor observes the difference $\Delta\vec{v}(z)$ between the wind vectors at balloon height $\vec{v}(z+h)$ and at payload height $\vec{v}(z)$.

In the following, the general principle of both LITOS sensors and their theoretical signal behavior as well as the calibration procedure are described. Constant-Temperature-Anemometers have a long history of application in measuring flow properties like mean and fluctuating velocity components. Early experiments with CTAs have already been performed at the beginning of the last century [*Comte-Bellot*, 1976, and references therein]. In Fig. 3.2 the schematic diagram of a Constant-Temperature-Anemometer is presented. The working principle of CTAs consists basically in detecting the differential voltage of a Wheatstone bridge. More precisely, a thin wire (typical diameter: $> 5\,\mu$m, typical length: ~ 1 mm, e.g. Dantec Dynamics Type 55P03) forms one leg of the Wheatstone Bridge and is heated to $\sim$500 K. To keep the bridge balanced, a servo amplifier controls the current to the wire so that the wire resistance - and hence temperature - is kept constant.

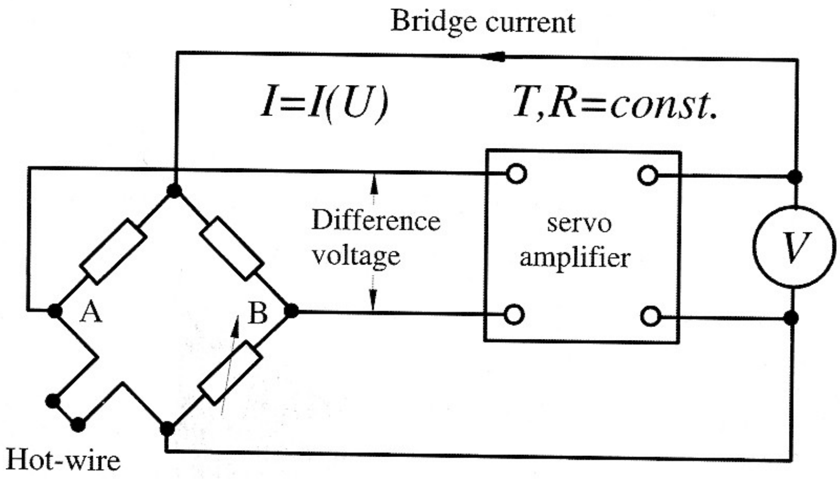

Figure 3.2.: Principal circuit of a Constant-Temperature-Anemometer [from *Durst*, 2008]. Changes of the hot wire resistance, i.e. temperature due to convective cooling arises at the servo amplifier as differential voltages and therefore represent directly the ambient flow velocity. More details are described in the text.

If the bridge is balanced, no voltage difference occurs between the input and output of the servo amplifier. But due to convective cooling by the flow velocity, the wire temperature will accordingly be modified and its resistance changes. Consequently, a differential voltage arises at the servo amplifier. In order to restore the balance of the bridge, the wire current has to be increased or decreased, respectively. Therefore, the resulting bridge voltage depends directly on the ambient flow velocity.
Concerning the general sensor behavior, several extensive studies were performed and have resulted in theoretical and semi-empirical descriptions of the measured signal [e.g., *Bruun*, 1970; *Bruun et al.*, 1988; *van Dijk and Nieuwstadt*, 2004]. Only the main aspects will be summarized here, while the reader is referred to standard text books for more details [e.g., *Bruun*, 1995; *Hinze*, 1959]. Generally, the heat from the wire is transferred to the surrounding fluid by radiation, free convection, forced convection, and the heat flow through the leads (see Fig. 3.3).
Therewith, an equation for the supplied heat $\dot{Q}_{\mathrm{E}}$ is derived which is equivalent to the sum

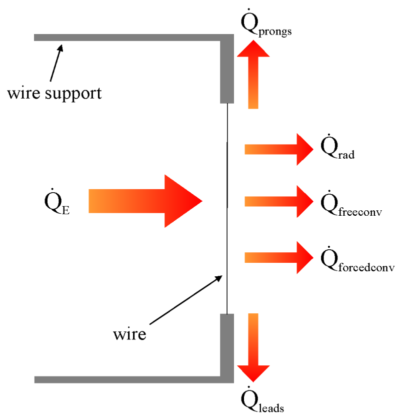

Figure 3.3.: Heat balance at the sensor: The supplied heat $\dot{Q}_{\mathrm{E}}$ is transferred to the surrounding fluid by radiation $\dot{Q}_{\mathrm{rad}}$, free convection $\dot{Q}_{\mathrm{freeconv}}$, forced convection $\dot{Q}_{\mathrm{forcedconv}}$ and the heat flow through the leads $\dot{Q}_{\mathrm{leads}}$.

of the heat fluxes:

$$\dot{Q}_{\mathrm{E}} = I^2 R = \frac{U^2}{R} = \dot{Q}_{\mathrm{rad}} + \dot{Q}_{\mathrm{freeconv}} + \dot{Q}_{\mathrm{leads}} + \dot{Q}_{\mathrm{forcedconv}} \tag{3.1}$$

where U is the bridge voltage, R the wire resistance and I the electric current. Due to the small size of the heated wire, radiative cooling $\dot{Q}_{\mathrm{rad}}$ is considerably smaller than the heat which is emitted by the sensor by e.g. forced convection $\dot{Q}_{\mathrm{forcedconv}}$ [*Durst*, 2008]. To ascertain this assumption, the radiative cooling for stratospheric conditions has been determined based on data from the BEXUS flights.The heat transfer due to radiation amounts to a maximum factor of 1.3 % of the total heat transfer. Therefore, the heat loss resulting from radiation can be neglected.
According to *Collis and Williams* [1959], free convection $\dot{Q}_{\mathrm{freeconv}}$ can also be omitted, if

$$Re > Gr^{1/3} \tag{3.2}$$

where Re is the Reynolds number

$$Re = \frac{v\ d_{\mathrm{w}}}{\nu} \tag{3.3}$$

(v=flow velocity, d_{w}= wire diameter and ν= kinematic viscosity of the fluid) and Gr the Grashof number

$$Gr = g(T_{\mathrm{w}} - T_{\mathrm{a}})\ \frac{d_{\mathrm{w}}^3}{\nu^2\ T_{\mathrm{a}}}, \tag{3.4}$$

(g is the gravitational acceleration, T_{w} the wire temperature and T_{a} the temperature of the ambient fluid). To verify the requirement in Eq. 3.2, the Grashof number and the Reynolds number have been calculated using typical data from the BEXUS soundings (see Fig. 3.4). Throughout the entire ascent phase, Re is much larger than $Gr^{1/3}$ and therefore it is possible to omit the free convection term in the heat transfer Eq. (3.1).
In order to minimize the heat flow from the wire to the leads ($\dot{Q}_{\mathrm{leads}}$), the wire has gold-plated ends connecting it with the wire leads. Thereby, a much more uniform temperature along the wire is achieved. Nevertheless, for typical CTA applications, the heat loss to the

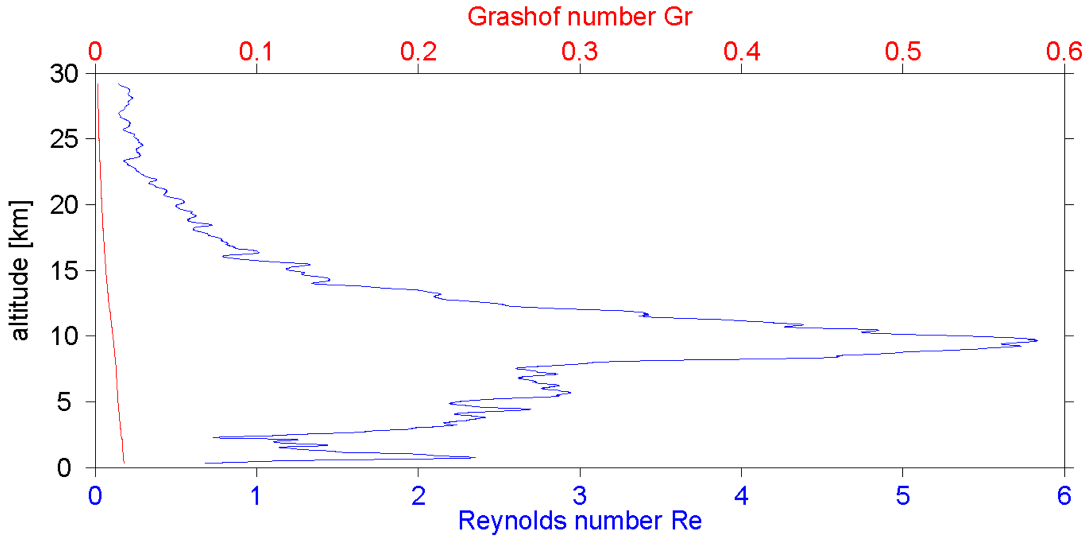

Figure 3.4.: The Reynolds number *Re* (blue line) and the Grashof number *Gr* (red line) plotted as a function of altitude using data from BEXUS soundings. Since *Re* is much larger than *Gr* the heat transferred from the wire to the surrounding fluid by free convection can be omitted.

leads amounts to about 10–20 % of the total heat loss from the sensor [*Durst*, 2008]. Thus the heat flow through the leads is considered to be proportional to the forced convective flow and Eq. (3.1) simplifies to

$$\dot{Q}_{\mathrm{E}} \;\approx\; c \cdot \dot{Q}_{\mathrm{forcedconv}} \tag{3.5}$$

where c is a constant. Finally according to Eq. (3.1) one gets

$$U^2 \;=\; c\, R\, \dot{Q}_{\mathrm{forcedconv}}. \tag{3.6}$$

The measured voltage signal is therefore directly related to the heat loss through forced convection. The latter is defined as:

$$\dot{Q}_{\mathrm{forcedconv}} \;=\; \alpha\, \pi\, l_{\mathrm{w}}\, d_{\mathrm{w}}\, (T_{\mathrm{w}} - T_{\mathrm{a}}), \tag{3.7}$$

where α is the heat-transfer coefficient, l_{w} the wire length, d_{w} the its diameter, T_{w} the temperature of the wire, and T_{a} the temperature of the ambient flow. The heat-transfer coefficient is given by

$$\alpha \;=\; \frac{Nu\, k}{d_{\mathrm{w}}} \tag{3.8}$$

where Nu is the Nusselt number and k represents the heat conduction of the fluid. The Nusselt number is defined to be a function of

$$Nu \;=\; Nu(Re,\, Gr,\, Kn,\, Pr,\, Ma,\, l_{\mathrm{w}}/d_{\mathrm{w}},\, \delta T_{\mathrm{a}}, \ldots). \tag{3.9}$$

By inserting Eqs. (3.1), (3.7), and (3.8) in Eq. (3.5) one obtains for the measured voltage

$$U^2 \;=\; c\; Nu\; k\; \pi\; l_{\mathrm{w}}\; R\; (T_{\mathrm{w}} - T_{\mathrm{a}}). \tag{3.10}$$

For further examination, Nu has to be determined individually for every wire and the flow properties described by e.g. Re, Gr, the Knudsen number Kn, the Prandtl number Pr, and the Mach number Ma. There exist several approaches in the literature for the empirical estimation of the Nusselt number for specific flow conditions [e.g., *Collis and Williams*, 1959; *Cimbala and Park*, 1990; *Durst et al.*, 1996]. The advantage of those formulations of Nu would be that the heat loss from the wire and the dependence on the flow velocity could be obtained without calibration. However, a precise knowledge of all influencing parameters can not be provided with sufficient accuracy. For example, parameters of the wire (i.e. effective length and diameter) are not available with the required precision due to the complicated process of the wire manufacturing. Consequently, for practical reasons, an individual calibration of each wire is usually preferred. It should be pointed out here that for geophysical analysis, it is not necessary to derive absolute wind velocity values from the CTA signal. Instead, the spectrum of the unscaled voltage signal is used to retrieve turbulent parameters (see Sect. 4.3).

However, in order to understand the principle of the CTA techniques and the laboratory experiments, the calibration procedure is briefly described here. During such a calibration procedure, the wire is placed in a wind tunnel to adjust to different laminar flow velocities. As a result, one obtains a static calibration curve of the output voltages U as a function of the flow velocities v. Based on *King* [1914], the calibration data can be fitted by the modified King's law:

$$U^2 = A + Bv^n \tag{3.11}$$

where A and B are empirical calibration constants for each fluid. The exponent n depends slightly on the flow velocity. According to *Jörgensen* [2002], n=0.45 is a recommended starting value and one has to vary n until the curve fit errors are acceptable. By determining the calibration constants A and B, it is then possible to convert the measured voltages to wind velocities. Figure 3.5 shows a typical example with a series of calibration points between 1 and 15 m/s. The measurements were taken at the *Lehrstuhl für Strömungsmechanik* (LSM) at the University of Rostock with a calibrated wind tunnel providing independent values for the wind velocity. Obviously, the wire is most sensitive at small wind velocities, where also the LITOS measurements are expected to occur. Unfortunately, wind velocities below 1 m/s cannot be obtained at the LSM with sufficient stability. Nevertheless the calibration curve is still valid in the low velocity range, as for an accurate King's law fit sufficient calibration points have been taken at higher velocities.

However, the crucial point is that the calibration coefficients are only valid if the ambient conditions do not differ from those during the calibration. This concerns not only the wind conditions, but also density, temperature, and humidity [*Cimbala and Park*, 1990; *Cardell*, 1993; *Durst et al.*, 1996; *Hugo et al.*, 1999]. Thus, the calibration should be performed under ambient conditions similar to the conditions during the measurements. For stratospheric conditions, the air density varies between 1.2 kg/m^3 and $\sim$ 1.0$\times$10^{-2} kg/m^3, the (relative)

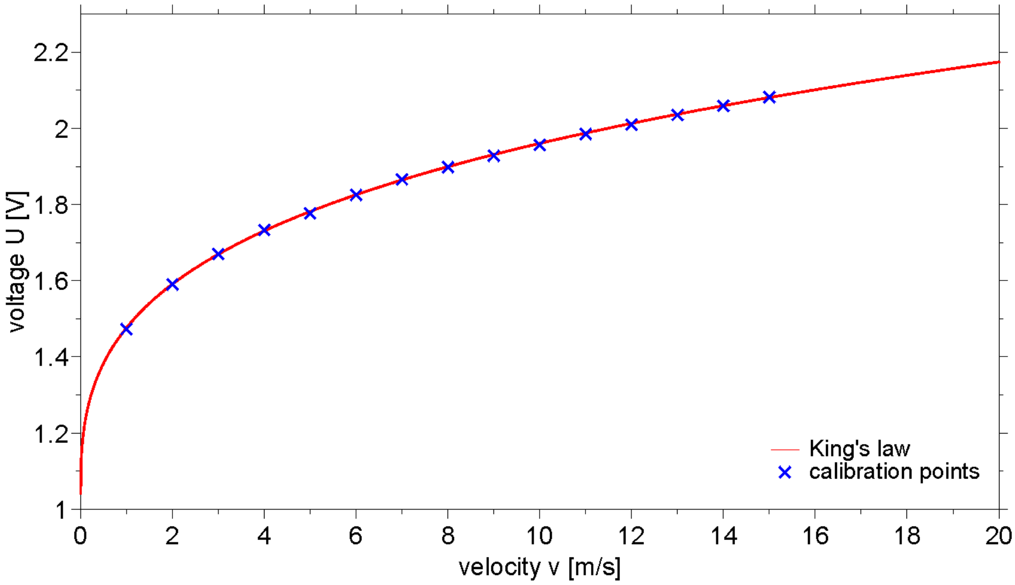

Figure 3.5.: Example of a calibration curve: The King's law (red line) has been fitted to the voltage U (data points) as a function of the flow velocities v. More details are described in the text.

wind velocities are up to 2 m/s and a minimum temperature of ∼200 K can be obtained. The water vapor mixing ratio in the stratosphere amounts to ∼ 5 ppm and therefore the influence on the measurements is negligible [*Durst et al.*, 1996]. For geophysical analyses, i.e. for the calculation of spectra, only 8 − 20 s (40 − 100 m) of data are used and one can assume sufficiently constant background values for e.g. the temperature within this period. However, the CTA behavior for the wide pressure and temperature ranges has occurring during a balloon flight never been investigated and the properties of the CTA sensor are therefore unknown for stratospheric conditions. Hence, laboratory tests within a climate and a vacuum chamber have been performed to check the response of the CTA on varying ambient conditions, i.e. temperature and pressure. The results are presented in Sect. 3.2.

3.1.2. Constant-Current-Anemometer for temperature observations

Constant-Current-Anemometers (CCA) operate basically as a resistance thermometer and are eminently suitable for measurements of high-frequency temperature fluctuations. Figure 3.6 presents the schematic diagram of a CCA. Contrary to CTAs, the Wheatstone bridge is operated with a constant current and the wire resistance varies with the fluid temperature. The resistance variations modify the voltage of the bridge. Hence, the measured voltage fluctuations are directly related to the resistance fluctuations and therewith to the fluid temperature. The important aspect hereby is that the probe current has to be quite low to avoid disturbances by the flow velocity, but on the other hand high enough to provoke a off-balance of the bridge. Therewith, the CCA is usually operated with the lowest possible current [*Bruun*, 1995], i.e. 0.2 mA for LITOS. Additionally, the diameter of the wire is of special importance. As the time constant varies with the wire diameter, it is favorable to use very thin wires (here: length 0.4 mm, diameter 1 μm, Dantec Dynamics Type 55P13).

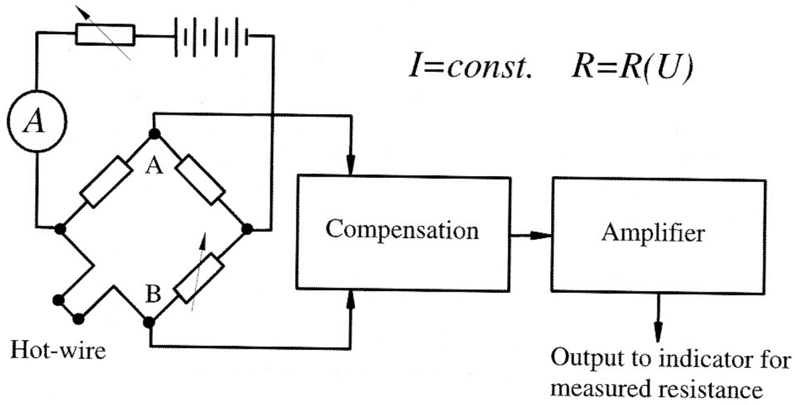

Figure 3.6.: Principal circuit of a Constant-Current-Anemometer [from *Durst*, 2008]. Changes of the cold wire resistance caused by ambient temperature fluctuations lead to modifications of the bridge voltages.

Now, the relationship between the fluid temperature and the bridge voltage will be addressed. First of all, the voltage U can be expressed in term of the probe resistance:

$$U = \ Gain \cdot (100 \cdot I \cdot (R_{\mathrm{sensor}} + R_{\mathrm{leads}} + R_{\mathrm{supp}} + R_{\mathrm{cable}}) - U_{\mathrm{offset}}) \tag{3.12}$$

where R_{leads} is the probe leads resistance, R_{supp} the supporting resistance and R_{cable} the resistance of the connection cable, with all data supplied by the manufacturer. I represents the current of the wire and $Gain$ and U_{offset} are the possible settings of the Wheatstone bridge to adjust for the specific measurement conditions. The probe resistance R_{sensor} varies directly with the ambient temperature T_{a} by:

$$R_{\mathrm{sensor}} = R_{\mathrm{sensor,0}} \cdot (1 + \alpha_0 \cdot (T_{\mathrm{a}} - T_0)) \tag{3.13}$$

where $R_{\mathrm{sensor,0}}$ the sensor resistance at temperature $T_0 = 20\,^\circ$ C and α_0 its temperature coefficient, both provided by the manufacturer. By inserting Eq. 3.13 in Eq. 3.12, the following expression for the temperature of the ambient flow is derived:

$$T = \left[\left(\frac{U + U_{\mathrm{offset}}}{100 \cdot Gain \cdot I} - R_{\mathrm{leads}} - R_{\mathrm{supp}} - R_{\mathrm{cable}}\right)\frac{1}{R_{\mathrm{sensor,0}}} - 1\right]\frac{1}{\alpha_0} + T_0. \tag{3.14}$$

Similar to the CTA system, a relation between the ambient temperature and the supplied voltage is derived via direct calibration. Figure 3.7 shows such a calibration curve for the CCA system obtained within a climate chamber. In contrast to the King's law procedure for CTA calibration, the temperature is directly related to measured voltages via a linear fit:

$$T = A \cdot U + B. \tag{3.15}$$

Therewith the measured voltage fluctuations are converted to absolute temperature fluctuations.
Besides the calibration procedure, another important question concerning the applicability of CCA systems for balloon soundings appears. Will the general behavior of the CCA sensor be influenced by the ambient stratospheric conditions or not? Therefore, the two main influencing factors, namely flow velocity and pressure, have been investigated by laboratory measurements (see next Sect. 3.2).

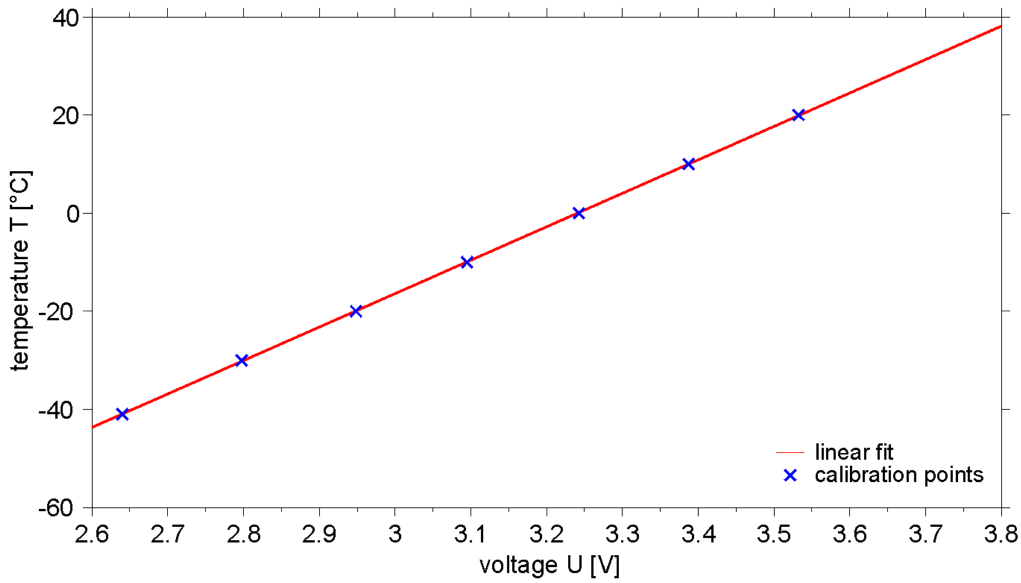

Figure 3.7.: Example of a CCA calibration curve. The red line represents the linear fit to the measured voltage values U (data points) as a function of temperature T.

3.2. Laboratory measurements of CTA and CCA response

As mentioned above, CTA and CCA sensors have never been used for balloon soundings and their properties are therefore unknown for applications besides standard laboratory and lower tropospheric conditions. Hence, laboratory tests within a climate and a vacuum chamber have been carried out to simulate stratospheric conditions. All laboratory measurements have been performed at the German Aerospace Center (DLR) Berlin-Adlershof.
Since both sensors measure directly the wind velocity (CTA) or could possibly be influenced by it (CCA), a small wind calibration unit designed especially for CTA/CCA sensors has been used during all laboratory test procedures. This wind calibration unit contains a nozzle and by measuring the pressure drop across the nozzle the flow velocity is calculated via the

equation of Venant-Wantzel. The wind calibration unit has been integrated into a climate and a vacuum chamber and thereby different values for temperature or pressure (i.e. density) of the flow passing the CTA/CCA sensor have been set, while knowing the exact flow velocities. Overall, measurements for a velocity range from 3 to 35 m/s at pressures between 50 and 1000 hPa and for a temperature range of 233 to 293 K have been taken. Due to technical limitations of the wind calibration unit (i.e. overheating of the motor), no measurements below 3 m/s and below 50 hPa have been performed. Temperature changes have been observed during the entire experiment phase with a data logger from MSR Electronics GmbH and have been considered in the determination of the flow velocity. The accuracy of the calculated flow velocity is therefore solely determined by the precision of the pressure sensors manufactured by Kalinsky Sensor Elektronik GmbH & Co. KG, which is specified with ± 1 %. Hence, the velocity behind the nozzle is determined with an accuracy of ± 0.2 m/s.

The next sections present the results obtained from the laboratory measurements. First, the temperature and pressure influence on CTA measurements will be described in Sect. 3.2.1 and Sect. 3.2.2. Afterwards, the velocity and pressure influence on CCA observations will be studied in Sect. 3.2.3 and Sect. 3.2.4. Finally, in Sect. 3.2.5 possible limitations of CTA and CCA measurements at low density flow will be discussed.

3.2.1. Temperature influence on CTA measurements

In Sect. 3.1.1 it is shown that the heat transfer from the wire to the surrounding fluid is proportional to the temperature difference between the sensor and the fluid. From other studies, it is known that the CTA response is influenced by temperature variations of the surrounding fluid during the experiment [e.g., *van Dijk and Nieuwstadt*, 2004]. For the correction of this temperature influence, different methods are suggested in the literature [e.g., *Bruun*, 1995; *Jörgensen*, 2002]. However, all correction methods are specified for only small temperature drifts and for temperature ranges not found in the stratosphere. In other words, the CTA response has never been investigated below $0\,^\circ$C. The climate chamber at the DLR offers measurements down to $-40\,^\circ$C. The performed measurements therefore describes the sensor behavior at temperatures below $0\,^\circ$C, for the first time.
Figure 3.8 shows the voltage signal for various velocities obtained at different temperatures. The thin lines represent the King's law fits (according to Eq. 3.11) for each temperature level. As expected the results reveal an influence of the temperature on the CTA response. For the examined temperature range, a maximum slope of 5 mV/K (i.e. 0.23 % / K) has been found.
The question is now, whether this temperature influence will have an impact on the sensitivity of the wire response, i.e. on the wind measurements. Therefore, Fig. 3.9 shows the sensitivity ($\Delta U/\Delta v$) as a function of velocity for different temperatures. Obviously, the temperature has no significant effect on the sensor sensitivity. But, besides these findings, a considerable velocity influence on the sensor sensitivity can be noticed. In appendix . C it is shown that the influence of the relative background wind is rather small. For the calculated energy dissipation rate a deviation of only $\sim$2 % has been obtained.

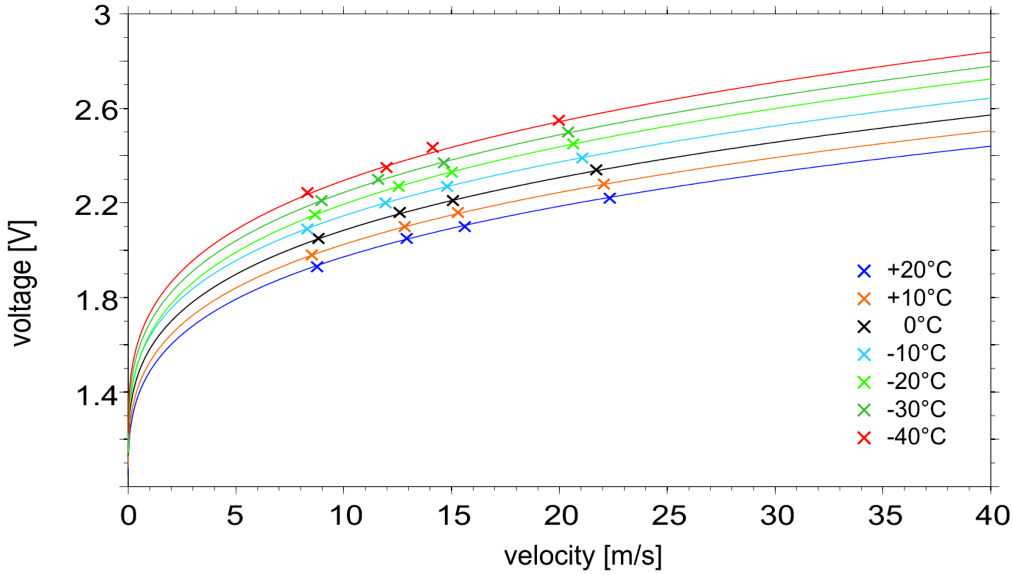

Figure 3.8.: CTA response for different temperatures. The King's law (thin lines) has been fitted to the CTA voltage signal U (data points) as a function of velocity v for different temperatures ranging from $-40\,^\circ$C to $20\,^\circ$C.

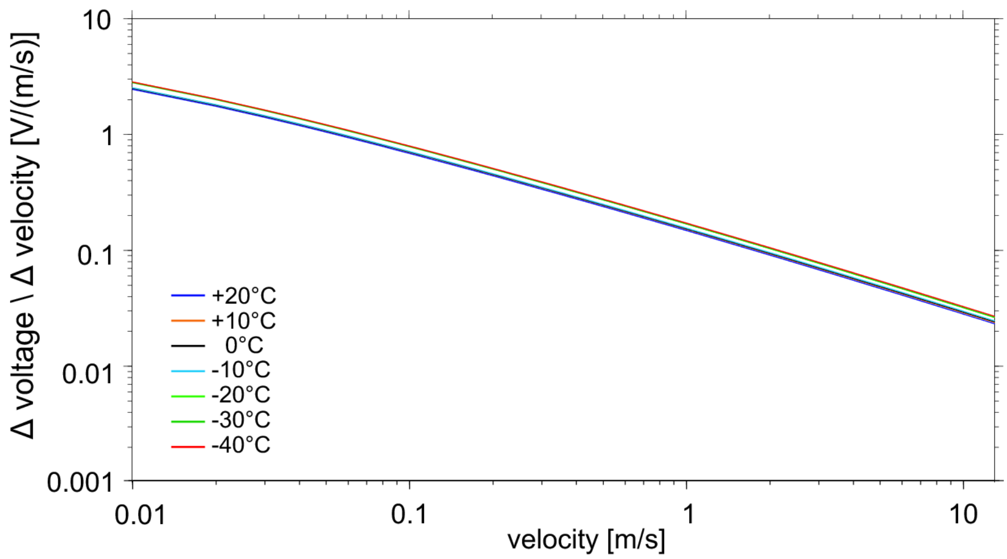

Figure 3.9.: The sensitivity of the CTA signal ($\Delta U/\Delta v$) as a function of velocity shows no significant temperature influence for the examined range from $-40\,^\circ$C to $20\,^\circ$C.

However, as noted earlier the unscaled voltage signal is used for the determination of the spectral slope of the turbulent fluctuations. Since the temperature does not affect the sensitivity of the sensor response, no correction of the temperature influence is required.

3.2.2. Pressure influence on CTA measurements

So far, the pressure influence on the CTA response has been barely investigated and the few approaches do not cover pressure ranges expected for stratospheric soundings [e.g., *Hugo et al.*, 1999]. In order to study the pressure influence on the sensor response, tests within a vacuum chamber have been conducted. The temperature during the measurements changed less than 1 K and therefore does not affect the results.

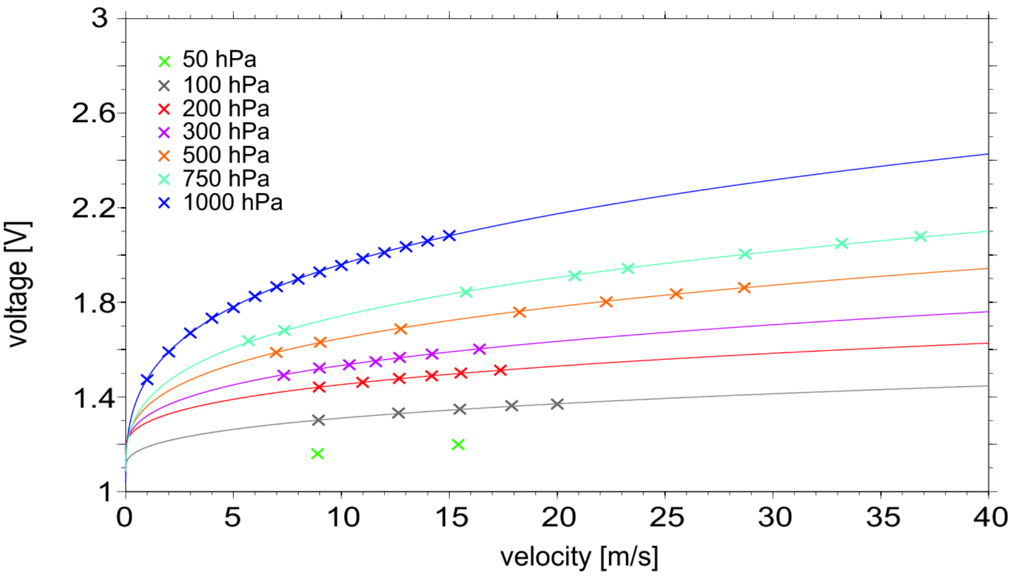

Figure 3.10.: The King's law fit (thin lines) has been calculated for the CTA voltage signals (data points) as a function of velocity for different pressure levels. At 50 hPa, only two points are obtained. Thus the King's law fit is omitted due to large ambiguities.

In Fig. 3.10 the voltage signal is presented for various velocities together with the King's law fits (according to Eq. 3.11) represented by thin lines at different pressure levels. A direct pressure influence can easily be seen, as the slope of the King's law fit at 1000 hPa differs significantly from the 100 hPa curve. In the same way as for the temperature variations, also the sensitivity $\Delta U/\Delta v$ is shown as a function of velocity for the different pressure levels. As can be seen from Fig. 3.11 the sensitivity decreases with decreasing pressure and this effect is most evident at lower velocities. Again, the velocity influences directly the sensitivity of the sensor response and this effect is even much more pronounced than the pressure influence. However, it is demonstrated in appendix C that the dependence of the sensitivity on the velocity has no significant impact on the spectral slopes of the turbulence measurements.

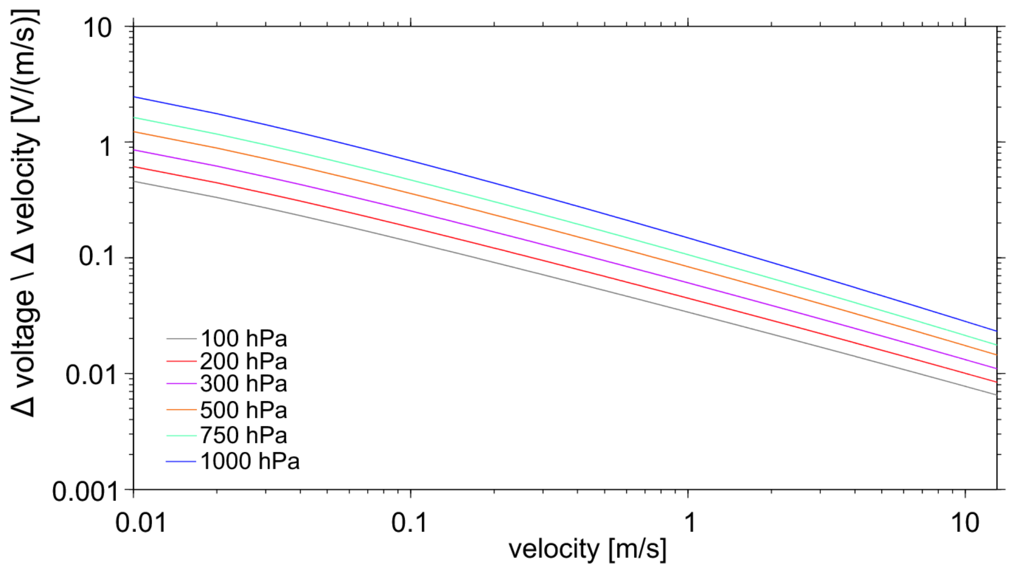

Figure 3.11.: Sensitivity of the CTA signal as a function of velocity for the different examined pressure levels. With decreasing pressure, the sensitivity decreases. For more details: please see text.

Figure 3.11 raises the questions whether the sensor sensitivity decreases further at pressures below 100 hPa and whether there is a lower pressure limit for CTA soundings. This issue will be discussed in Sect. 3.2.5.

3.2.3. Velocity influence on CCA measurements

As described in Sect. 3.1.2, the CCA sensor is operated with a very low current in order to reduce the influence of the surrounding flow velocity to a minimum. To verify this assumption also for stratospheric conditions, laboratory studies for different temperature levels and different flow velocities have been carried out. Figure 3.12 shows the results for temperatures between $+20\,^\circ$C and $-40\,^\circ$C and a velocity range from 0 m/s up to ~ 35 m/s. Obviously, the velocity has no impact on the sensor response as the voltage values show almost no variations for different flow velocities. The maximum voltage difference for one temperature level amounts to 5 mV. This difference can be due to temperature variations inside the climate chamber or due to uncertainties of temperature sensors. Consequently, a velocity influence on the CCA sensor can be excluded and the measured voltage values solely reflect the ambient temperature of the fluid.

3.2.4. Pressure influence on CCA measurements

The CCA behavior at low density flows has never been investigated. But during balloon launches, the pressure varies significantly compared to laboratory applications of CCAs.

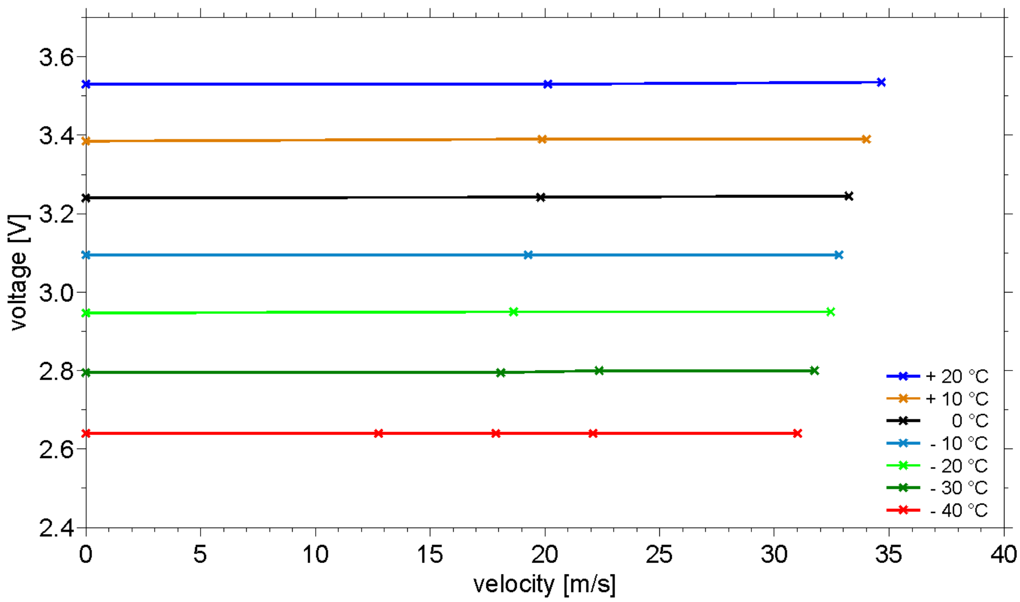

Figure 3.12.: CCA voltage values as a function of flow velocity for different temperature levels obtained within the climate chamber. No influence of the velocity is observed.

Therefore, the pressure influence on the CCA response has been studied. The temperature within the vacuum chamber at the DLR has been measured for different pressure levels with the CCA system and simultaneously with the independent sensor MSR 145 (MSR Electronics GmbH) placed next to the CCA system. Based on a calibration performed within the climate chamber, the CCA voltage values have been converted to temperature values with Eq. 3.15. Both temperature profiles are presented in Fig. 3.13. The CCA system represents nicely the temperature change within the vacuum chamber measured by the MSR sensor. The maximum difference of 0.26 $^\circ$ C between both profiles is well within the accuracy of the MSR sensor specified by the manufacturer with $\pm 0.5\,^\circ$ C. Additionally, even though the MSR sensor has been placed as near as possible to the CCA system, temperature inhomogeneities within the vacuum chamber are likely.
The important result is, that no systematic pressure influence on the sensor behavior is observed. Therewith, the CCA system can be used without restrictions for balloon soundings in the stratosphere.

3.2.5. Limitations of CTA/CCA at low density flows

The heat-transfer equation for the interpretation of the CTA signal (shown in Sect. 3.1.1) and the adjustment of the CCA wire resistance to the fluid temperature requires continuum flow conditions. Therefore, it has to be investigated whether continuum flow approximations are applicable during the balloon flight or not.

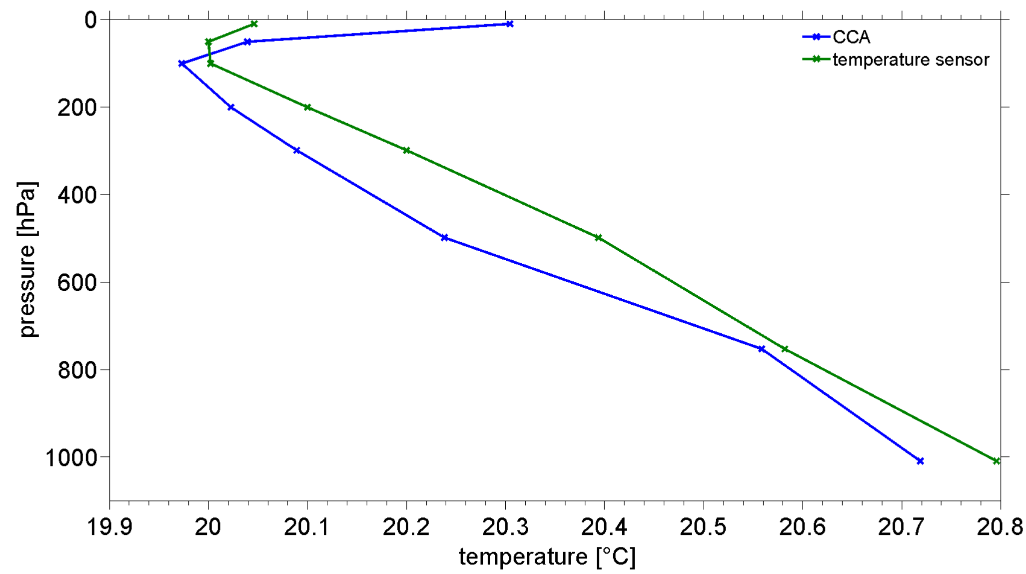

Figure 3.13.: Comparison of the temperature profile obtained inside the vacuum chamber with the CCA system (blue line) and with an independent temperature sensor (green line).

The Knudsen number Kn is a parameter describing the type of flow. Kn is defined as the dimensionless ratio of the mean free path λ to a characteristic length scale, here the wire diameter d_w,

$$Kn = \lambda/d_\mathrm{w}. \tag{3.16}$$

Therewith, the flow regime can be divided into the continuum flow ($Kn<10^{-2}$), the slip flow regime ($10^{-2}<Kn<10^{-1}$), the transition regime ($10^{-1}<Kn<10$) and the free molecular flow for $Kn>10$ [e.g., *Devienne*, 1965]. Typically, CTA and CCA measurements are performed in the slip flow regime, where continuum flow equations are still appropriate. With decreasing pressure, the heat transfer by convection to the surrounding medium decreases. Finally, in the free molecular flow, continuum approximations are no longer applicable. Therewith, a lower pressure limit for CTA and CCA soundings can be estimated when $Kn>10$, i.e. at $\sim$1 hPa ($\sim$45 km).

Figure 3.14 shows the Knudsen number calculated for the vacuum test and for the BEXUS 6 flight. It can easily be seen, that for both cases the Knudsen number is well below the limitation of $Kn>10$.

Based on this result and the fact that the maximum altitude which can be reached with balloons is $\sim$40 km, it can be concluded that balloon-borne CTA and CCA measurements do not occur in the free molecular flow regime, i.e. the measurement principle is valid. Hence, the CTA and CCA system are well suitable for balloon soundings.

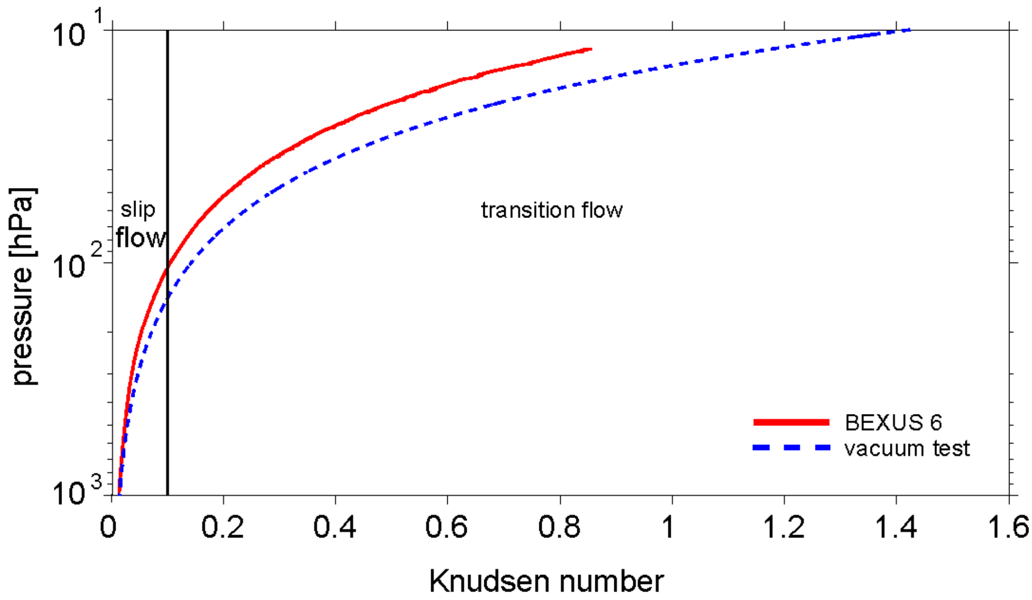

Figure 3.14.: The Knudsen number has been calculated using data from the vacuum test and from the BEXUS 6 flight. The slip flow and the transition flow regime are defined as $10^{-2}<Kn<10^{-1}$ and $10^{-1}<Kn<10$, respectively. More details are described in the text.

3.3. LITOS gondola system

LITOS has been launched as a small and compact stand-alone version for small weather balloon stations and has also been integrated into a bigger gondola for large stratospheric balloon soundings. Certain parts are equal for both versions and will be described in more detail below.

3.3.1. General setup of the LITOS payload

For the measurement of wind fluctuations a commercial CTA system from Dantec Dynamics is used consisting of a probe support, a Wheatstone bridge and special connection cables. Depending on the application, one can choose between different types and forms of the sensing element of the CTA system. For LITOS a single wire probe is used, as they have highest frequency response and a higher flow sensitivity compared to other probes. The wire is made of platinum plated tungsten with gold-plated ends (Dantec Dynamics Type 55P03) and is $5\,\mu$m in diameter and 1.25 mm long. During all measurements, the wire axis has been mounted vertically, i.e. parallel to the ascent direction, to achieve largest sensitivity for horizontal flow and less sensitivity for vertical flow. To observe temperature fluctuations a CCA system also from Dantec Dynamics has been applied. Similar to the CTA system, it consists of the probe support, the Wheatstone bridge and connecting cables. The sensor is a 0.4 mm long, $1\,\mu$m diameter platinum wire.

The output signal of the CTA or CCA system is converted using a specially designed 16 bit ADC with a sampling rate of 2 kHz or 8 kHz. Hence, a spatial resolution of 2.5 mm or $\sim$0.6 mm is achieved, assuming that the balloon ascends with an average speed of 5 m/s. The ADC device also includes a data recording system, which saves the output signal on an SD card. Optionally, the data can be transmitted by telemetry to the ground station.
The telemetry system was developed by Reimesch Kommunikationssysteme. It consists of an ARF35 radio modem with a transmission power of 500 mW, a bandwidth of 38.4 kbps for the 869 MHz band and a crossed-dipole transmitting antenna. In order to transmit the full resolved signal, a special data compression scheme has been developed at the IAP. The data stream is divided into frames. Due to the fact, that the changes of velocity or temperature are comparatively small within a few milliseconds, the compression algorithm saves only the average value within a certain period (frame) together with the deviations from the mean. Additional information like a time stamp and a checksum to identify possible transmission errors, is added. To receive the telemetry signal, a directional antenna system is used on ground. The system contains of four helical antennas mounted in a specific distance to each other, which follow actively the balloon based on GPS data. In combination with the emission power of the modem on board of LITOS, a horizontal distance of $\sim$ 150 km is covered. This range is sufficient for a typical balloon launch.
In addition, a housekeeping device has been developed at the IAP to measure the temperature, humidity, and pressure inside the electronic box. The battery voltage as well as the status of the CTA/CCA system is observed to identify any disturbances or possible failures of the system. As the gondola is not actively stabilized, rotational and pendulum motions may influence the measurements. Therefore, a tri-axis gyroscope and accelerometer (ADIS16350AMLZ) has been integrated to measure the attitude of the gondola with a sampling rate of 50 Hz (see appendix D). Thus, any spurious maxima in the obtained spectra of turbulent fluctuations can be identified and excluded. All housekeeping data are stored on-board on a second SD card.
The LITOS payload is recovered after flight. One reason is that, up to know, it is not possible to transmit all measured data. For instance, the housekeeping data are only saved on board. Also, the data stream of the CTA or CCA signal sampled with 8 kHz is too high to be transmitted completely. Only a reduced data stream of 2 kHz is sent to the ground station, while the whole 8 kHz signal is saved on board. Furthermore, all the electronic devices can be used again after recovery. Therefore, a tracking system manufactured by NAL Research Inc. has been included into the LITOS payload. Every two minutes during the whole flight including landing, it provides a GPS position transmitted via Iridium satellite communication.
Information about the atmospheric background are quite important for turbulence analysis and interpretation. Thus, a standard radiosonde (Väisälä RS92) completes the LITOS gondola system, providing atmospheric background profiles of wind, temperature, humidity and pressure at 2 s steps, i.e. $\sim$10 m. The whole system of LITOS consisting of CTA/CCA, ADC, telemetry, housekeeping, and tracking device. It may be launched together with the radiosonde on small gondolas or together with other independent instruments on large payloads. Specific properties of both launch configurations are described in the following.

3.3.2. LITOS on small gondolas

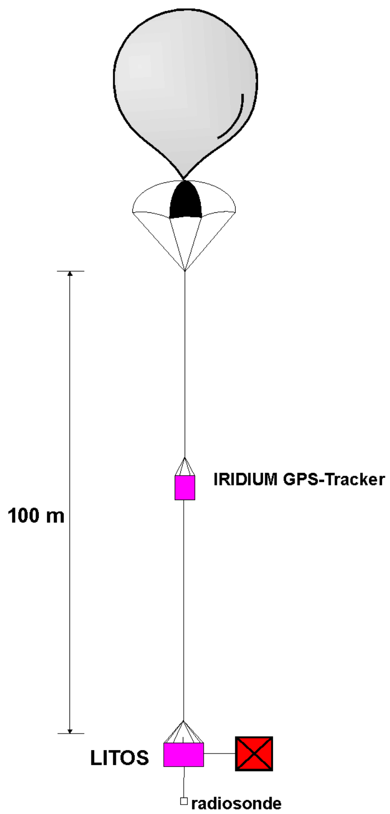

Figure 3.15.: Schematic drawing of the small gondola system of LITOS including a weather balloon, a parachute for safe landing, the Iridium GPS tracking system and the LITOS box with a wind adjusting vane as well as a radiosonde.

LITOS has been launched from Kühlungsborn with a specially designed gondola of 35 cm side length. As the overall weight of the payload is only ∼ 5 kg, this version of LITOS can be launched at any radiosonde station with a large weather balloon. Because of the limited weight, the flight configuration of LITOS on small gondolas includes only a CTA system to measure wind fluctuations. However, attempts are made to develop a combined CTA/CCA system for small LITOS gondolas. Figure 3.15 shows the flight train of LITOS consisting of a rubber balloon, a parachute for a slow descent after balloon burst, the recovery system, the payload itself including the CTA system and the housekeeping device, and finally a radiosonde. Unwinders enable a distance of 100 m between the balloon and the gondola. Such large distance is required, to prevent measurements within the turbulent wake of the balloon. A short overview of the performed launches with LITOS from Kühlungsborn and their differences is presented in Tab. 3.1.

The CTA sensor is placed ∼ 20 cm above the top of the payload in order to avoid disturbances induced by the shear layer around the payload box. Laboratory measurements performed by A. Schneider (IAP, private communication) confirmed this assumption. Furthermore, the payload may be affected by pendulum and rotational motions (see appendix D). While the pendulum motions have comparatively long periods of 15 s, the rotations may occur on different scales. Thus, significant influence on the turbulent measurements has been observed, which hampers further analysis. In order to minimize the rotations, different configurations of wind vanes attached to the payload box have been tested. Best results are obtained with a combination of three wind vanes that decelerate significantly pendulum and rotational motions. This configuration will be further examined and optimized in future flights. Due to the difficulties in turbulence measurements with the small LITOS gondola caused by movements of the gondola, this study focuses on results of the BEXUS flights.

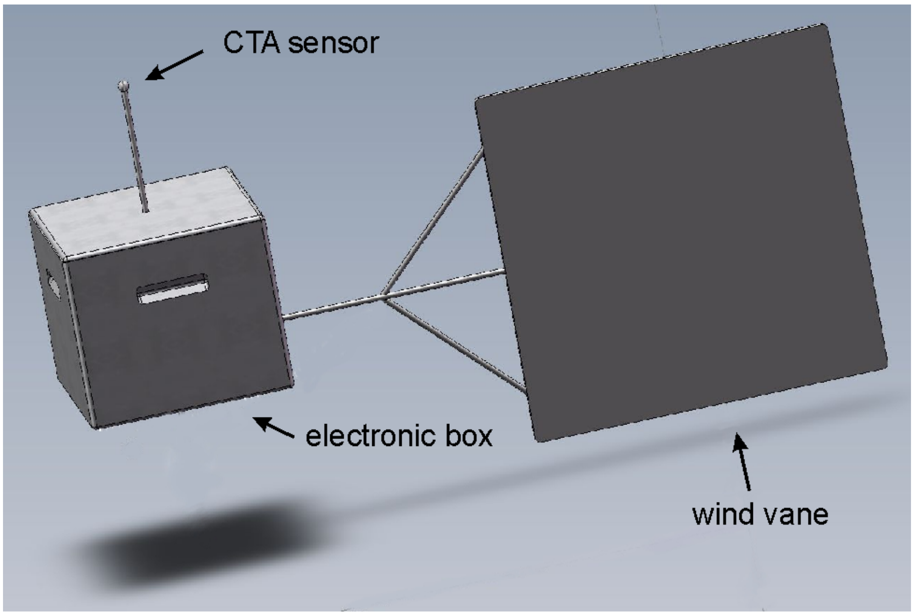

Figure 3.16.: Schematic drawing of the small LITOS gondola. The CTA sensor is placed ∼ 20 cm above the top of the box. A wind vane is mounted to the box in order to stabilize the gondola. All electronic devices are placed inside the box, which has a side length of 35 cm.

Table 3.1.: List of the performed launches of LITOS from the institute site in Kühlungsborn including some of their most important parameters.

Kühlungsborn (54 °N, 12 °E)

	12.12.2007	17.11.2008	27.01.2009	11.03.2010	01.07.2010	25.02.2011
balloon size/type	3000 g	1200 g	2000 g	3000 g	2000 g	300 g
gondola weight	3 kg	5 kg	5 kg	5 kg	5 kg	5.7 kg
distance balloon gondola	50 m	50 m	100 m	100 m	100 m	100 m
mean ascent rate	6.7 m/s	3 m/s	6.4 m/s	.5 m/s	5.1 m/s	4 m/s
max. altitude	35.3 km	28.9 km	31.5 km	30 km	31.5 km	30.8 km
sampling rate	2 kHz	2 kHz	2 kHz	8 kHz	8 kHz	8kHz
rot. and acc. sensor	-	-	-	+	+	+

3.3.3. LITOS on big gondolas

For the launches from Kiruna, LITOS has been integrated into the BEXUS gondola. The flight train of BEXUS, shown in Fig. 3.17, consists of a stratospheric plastic balloon and a cutting system connected to a parachute. Via uplink, the balloon is cut above a safe landing area and the payload descends slowly on parachute. Furthermore, the flight train includes the BEXUS telemetry system (EBASS), a radar reflector, and the payload. The distance between the lower edge of the balloon and the gondola is ~ 50 m.

The gondola has a side length of 75 cm and weighs ~ 120 kg (BEXUS 6) or ~ 140 kg (BEXUS 8). The flow around the gondola can significantly influence the turbulence measurements. In order to minimize those influences, the CTA and CCA sensors have been attached to long extensions (2 m long) mounted to the edges of the gondola (see Fig. 3.18). Therefore, the sensors were located 1.4 m above the gondola and a direct influence of the shear layer of the gondola can be excluded.
As the BEXUS gondola is not actively stabilized, rotational and pendulum motions may influence the measurements. Therefore, the attitude of the gondola has been studied for the BEXUS 6 gondola. The pendulum motions were measured by the LowCoINS instrument on the same payload (P. Montefusco, private communication). Their measurements reveal a typical pendulum velocity of 1.5 m/s (maximum 2 m/s) which affects the LITOS observations as a bias varying sinusoidal with a 20 s period. Before further analysis this bias is removed (see Sect. 4.3). Additional information about the gondola movements is found in appendix D.During the BEXUS 6 campaign in October 2008, only turbulent fluctuations in the velocity field were observed with a CTA system. For the BEXUS 8 campaign in October 2009, the velocity observations have been combined with CCA measurements to study temperature fluctuations. A short overview about the main differences between both launches is shown in Tab. 3.2. Due to much lower gondola motions and

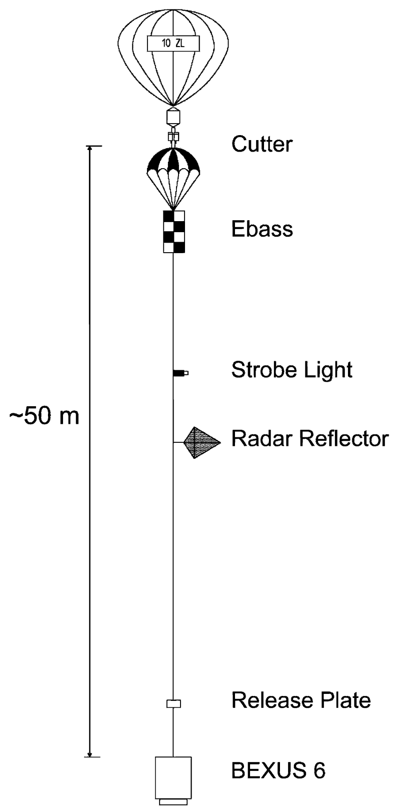

Figure 3.17.: The flight train of the BEXUS 6 gondola with a zero pressure balloon, a cutting mechanism, a parachute, the EBASS system (service system operated by SSC providing function for e.g. altitude control, flight termination), safety devices (Strobe light, Radar reflector), a release plate and the BEXUS gondola including the LITOS system. Schematic drawing was taken from the BEXUS user manual.

therewith less disturbances on the measurements compared to launches from Kühlungsborn, further data analysis will be focused on the results from the BEXUS campaigns only.

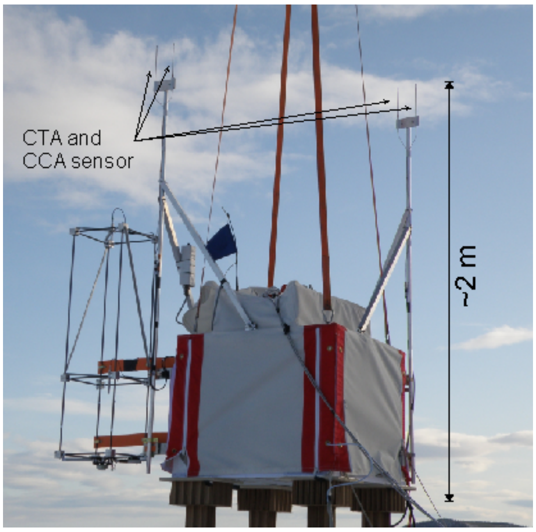

Figure 3.18.: The BEXUS 8 gondola in flight configuration. The CTA/CCA sensors of LITOS are placed 1.4 m above the gondola. All electronic devices have been integrated inside the gondola.

Table 3.2.: Overview of some parameters of the BEXUS 6 and 8 launch from Kiruna. ([1] from LowCoINS experiment)

Kiruna(67°N,21°E)

	BEXUS 6 08.10.2008	BEXUS 8 10.10.2009
balloon size/type	$10\,000\,m^3$	$12\,000\,m^3$
gondola weight	121 kg	140 kg
distance balloon gondola	50 m	50 m
sensor type	CTA	CTA + CCA
mean ascent rate	4.45 m/s	4.7 m/s
max. altitude	29 km	27.8 km
sampling rate	2 kHz	2 + 8 kHz
rot. and acc. sensor	+[1]	+

Chapter 4

Turbulence observations with LITOS

LITOS has been developed to study small-scale turbulent fluctuations in the temperature and wind field. Within this chapter first results of in-situ turbulence observations in the stratosphere will be presented. All data shown here were obtained during the BEXUS 6 campaign on 8 October 2008 and the BEXUS 8 campaign on 10 October 2009 performed at Kiruna (67° N, 21° E). Details concerning the technical set-up and the integration of LITOS into the BEXUS gondola can be found in Sect. 3.3.3.
Section 4.1 deals with observations of wind and temperature fluctuations and their spatial separation in turbulent and non-turbulent regions. In order to find all turbulent layers within the data set, a new algorithm has been developed and implemented. Its great advantage resides in the autonomous analysis of the complex and inhomogeneous data set. The method itself and the results are presented in Sect. 4.2. In Sect. 4.3 it is demonstrated that the observed turbulent regions are real atmospheric turbulence and not due to instrumental effects. For this purpose, spectra of the wind and temperature fluctuations have been calculated and compared with the turbulent spectrum expected from theory. In a second step, the energy dissipation rate is derived by fitting a theoretical model to the turbulent spectrum. The accuracy of the calculated energy dissipation rates is discussed in Sect. 4.3.1. In Sect. 4.4 altitude profiles of the dissipation rate are presented for the temperature and wind field. Finally, averaged values of energy dissipation rates obtained with LITOS are compared to values found in the literature in Sect. 4.4.3.

4.1. Turbulent fluctuations in the wind and temperature field

The data obtained with LITOS comprises voltage values of the CTA and CCA system sampled with a rate of 2 kHz (i.e. 0.5 ms time step) or 8 kHz (i.e. 0.125 ms time step). Before further analyses, these data have to be associated with time and altitude values. Based on the exact starting time and sampling rate and the fact, that there are no gaps within the data stream, time indexes for the measured voltage signal are constructed. These indexes are used to obtain the altitude profile. The altitude information has been taken from a commercial radiosonde (Väisälä RS 92), which is one main part of the LITOS payload. Via the time altitude information of the radiosonde, the time scale of the voltage signal is converted to an altitude scale. Therewith, an altitude profile of the measured voltage values of the CTA

and CCA sensor is obtained.
The voltage signal contains fast variations (with periods in the order of milliseconds) due to temperature and wind shear and slow variations ($\gg 1\,\mathrm{s}$ period) caused by gondola motions and decreasing sensitivity. In order to eliminate the low frequency effects, a spline trend

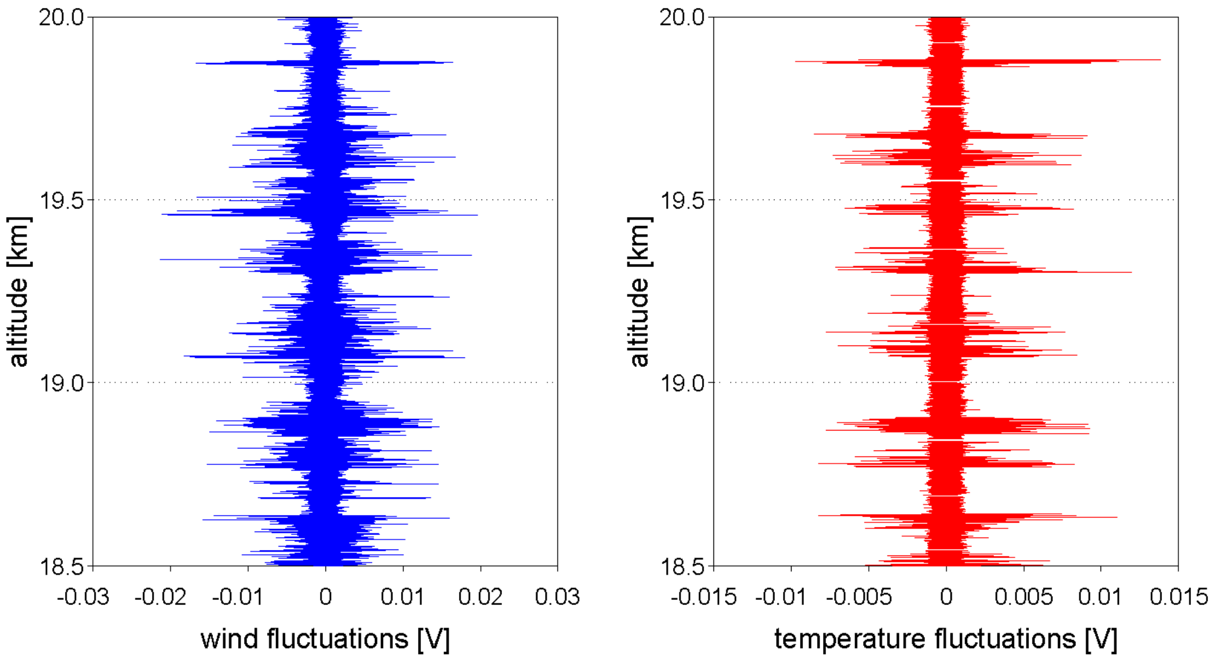

Figure 4.1.: Example of the observed profiles of velocity fluctuations (left panel) and temperature fluctuations (right panel) between 18.5 km and 20 km during the BEXUS 8 flight. Regions with strong turbulent fluctuations can be clearly distinguished from calm regions which are solely characterized by instrumental noise.

is removed from the measured voltage signal. The resulting profile then shows voltage fluctuations generated solely by atmospheric turbulence.
As a typical example, Fig. 4.1 shows measured wind (blue) and temperature fluctuations (red) after the spline removal for the altitude region between 18.5 km and 20 km during the BEXUS 8 flight. It can easily be seen, that within the wind field several turbulent layers have been detected. They can be identified by a varying amplitude of the fluctuations between 3 mV (larger than the noise level) and $\sim$ 20 mV. For example, one turbulent region can be identified between 19350 m and 19450 m or above from 19600 m up to 19750 m with more frequent voltages of $\sim$ 20 mV. Also thin isolated turbulent layers have been detected, e.g. around 19900 m. The question arises whether these regions belong to the same event, i.e. have the same source of turbulence. It is difficult to find an answer to this question, since the knowledge about stratospheric turbulence is limited and up to now experimental evidence or theoretical modeling of this phenomenon is rare. However, in Chap. 5 the occurrence of the turbulent layers and their relation to the background atmosphere as well as possible

indications of their source will be discussed.
The right part of Fig. 4.1 shows the measured temperature fluctuations for the same altitude region as the wind fluctuations. It should be noted, that the small gaps within the temperature profile are due to short-term disturbances caused by instrumental effects which have been removed from the data profile. Similarly to the observations within the wind field, several turbulent layers within the temperature field have been identified by voltage values between 1 mV (larger than the noise level) and ~8 mV, partly up to 14 mV. But, the layers seem to be thinner and the distance in between seems to be larger compared to the turbulent layers of the wind field. Hence, the turbulent regions of the temperature field do not cover the same altitude area as the regions of the turbulent wind field. The discrepancies can be indicative of different sources or different time scales of the measured turbulence. Furthermore, it should be emphasized, that if the mean background temperature gradient is adiabatic, no or only small temperature fluctuations appear while fluctuations within the wind field can still be present [*Holton*, 2004]. The combination of wind and temperature measurements with LITOS offers an excellent possibility to examine the theoretical statements concerning the differences between thermal and kinetic energy and the formation of turbulent layers (see Chap. 5). In addition to the continuing alternation between turbulent and non-turbulent regions, the observations reveal a quite abrupt and distinct transition between both regions.
Figure 4.2 (left) shows a detailed profile of one single turbulent layer within the stratospheric wind field. Again, the plot on the right hand side shows the same altitude region for the temperature field. One can see that in both profiles the laminar flow changes suddenly to turbulence at 19300 m. The turbulent layer within the wind field extends up to 19390 m. In contrast, the turbulent layer within the temperature field is less pronounced and less vertically extended. Already at 19320 m the temperature fluctuations diminish and up to 19370 m only very thin layers of turbulent temperature fluctuations appear. Above 19370 m there are no more temperature fluctuations, whereas the wind field is still turbulent. Obviously, both profiles of the wind and temperature fluctuations are quite inhomogeneous as they are characterized by a continuing but unpredictable alternation between turbulent and non-turbulent regions with sharp boundaries in between.
The layered structure has also been detected by earlier observations of e.g. *Sato and Woodman* [1982] and *Barat* [1982a]. But the high sampling rate of LITOS of 0.5 ms and less provides the possibility to observe even the variability within the turbulent layer itself. For instance, Fig. 4.2 shows that the amplitude of the turbulent fluctuations varies strongly and therefore the turbulent layer is highly inhomogeneous. Moreover, based on the high resolution data set, detailed profiles of the energy dissipation rate ε are obtained (see Sect. 4.3 and 4.4).
The non-turbulent region shown in Fig. 4.2 is characterized by small-amplitude fluctuations of 3 mV (wind) and 1 mV (temperature) which are caused by instrumental noise. Analyses of the given data sets reveal that the noise level is constant with altitude. Naturally, the specific value for the noise level depends on each individual sensor and the electronic setup, which has been described in Chap. 3. However, the constant noise level demonstrates, that the changing ambient conditions during the flight do not influence instrument perfor-

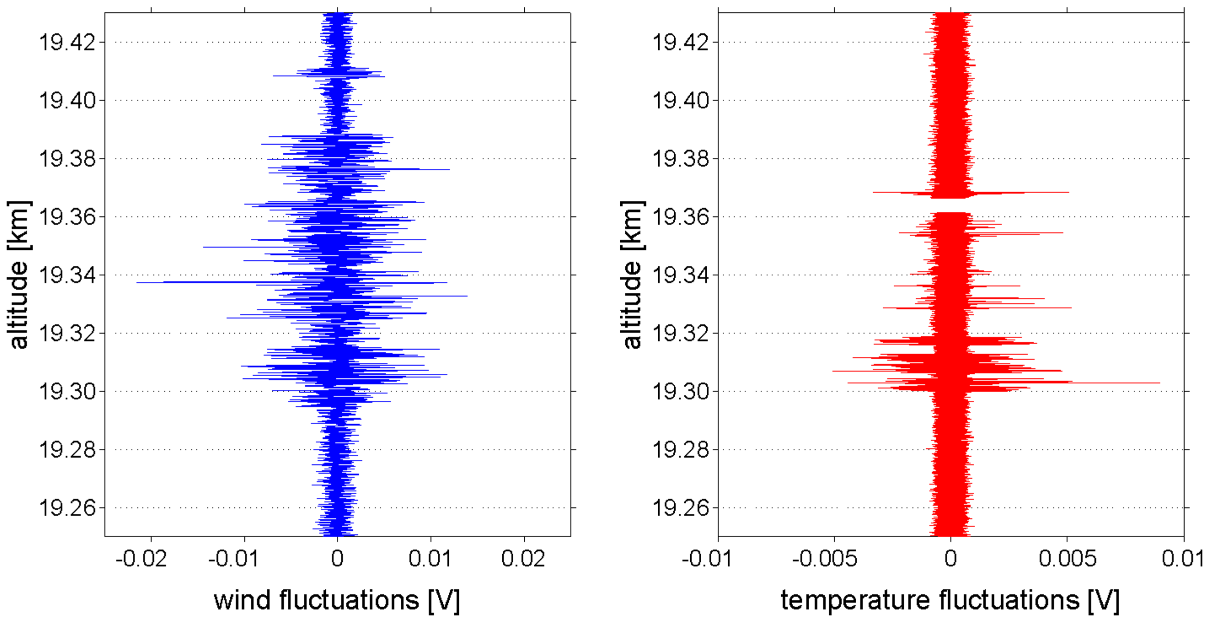

Figure 4.2.: Detailed profile of a single turbulent event observed during the BEXUS 8 flight within the wind (left panel) and temperature field (right panel). Typical of stratospheric turbulence is the sudden change from laminar to turbulent flow clearly visible in both profiles at ~ 19.3 km.

mance. This point emphasizes nicely that LITOS is well suited for small-scale turbulence measurements in the stratosphere. Finally, it should be noted that due to the simultaneous observation of wind and temperature fluctuations it is possible to analyze e.g. the relation between thermal and kinetic energy dissipation. Furthermore potential sources of the observed turbulent layers may be determined. The next Chap. 5 will address these questions.

4.2. Cluster analysis to identify turbulent layers

One major point of interest is the number and vertical expansion of turbulent layers detected with LITOS. Already emphasized in Sect. 4.1, the obtained data set is quite heterogeneous and comprehensive. Thus, an autonomous and effective method is required to analyze the given data profiles. Basically, turbulent layers are characterized by a high variability of the measured wind or temperature values within a certain altitude distance. Hence, an algorithm has been developed detecting such concentrations or clusters of turbulent values within the wind or temperature profile. Before the cluster algorithm can be applied, a preprocessing of the given data set has to be done in order to isolate turbulent data points from non-turbulent data points. Therefore, the noise level has been determined via the power spectrum for each sensor individually. Since the noise level is constant with altitude, this value has been used as a threshold to classify each data point of the signal as turbulent (larger than the threshold) or non-turbulent (smaller than the threshold).[1] After that procedure, the vertical profile of turbulent and non-turbulent points provides the basis for the cluster algorithm. It should be pointed out that data points can be classified as non-turbulent although they are located within a turbulent layer. The reason for this is that not all data points within a turbulent layer are necessarily larger than the noise level. That means, that there are in fact more data points within a turbulent layer than determined by the preprocessing. However, the aim of the cluster algorithm is to identify the beginning and ending of a turbulent layer and not the exact amount of data points within a turbulent layer. In order to determine the altitude for the beginning or ending of a turbulent layer only the data points which are larger than the noise level (provided by the preprocessing) are needed.
Based on the preprocessed data set, the algorithm assigns turbulent data points to one turbulent layer, i.e. cluster, depending on a certain number of adjacent turbulent points within a certain altitude distance. In other words, if a turbulent point has at least n turbulent neighbors within distance d, it is associated with a cluster. If this is not the case the point is considered as an outlier. Therefore the results of the cluster algorithm depend on these two parameters, namely the distance d and the minimum number of turbulent data points n. These parameters are based on the assumption about the density of turbulent points representing turbulent layers. Figure 4.3 shows an example of a turbulent layer (a) and the result of the cluster algorithm (b–d) depending on the values for the distance d and minimum number of neighbors n. In Fig. 4.3/a the measured wind fluctuations have been plotted (blue) together with the turbulent data points (red) determined by the preprocessing. Obviously several turbulent layers with different thicknesses have been detected. For a distance $d = 5\,\mathrm{m}$ and a minimum number of neighbors $n = 100$ (Fig. 4.3/b) one cluster has been identified from 9695 m up to $\sim$ 9740 m, a second cluster from 9750 m up to 9765 m and so on. In total 14 clusters have been identified with this parameter combination. For comparison, $d = 10\,\mathrm{m}$ and $n = 100$ (Fig. 4.3/c) yield only 3 clusters for the same altitude range. For instance, the region between 9800 m and 10130 m has been summarized to one big cluster, while it has been divided into several smaller clusters for the previous parameter combination. The reason is,

[1] Of course, a single data point can not indicate turbulence. But, the term *turbulent data point* is used to mark a data point as potentially belonging to a turbulent layer.

that $d = 10$ m allows a lower concentration of turbulent data points for the same altitude range and therefore clusters with a higher vertical expansion, i.e. thicker turbulent events can result. This is also evident from Fig. 4.3/d, where the distance d has been increased to 15 m and the minimum number of neighbors n is again 100. Now, the whole turbulent region has been merged to one big cluster, i.e. one turbulent layer from 9700 m up to 10130 m.

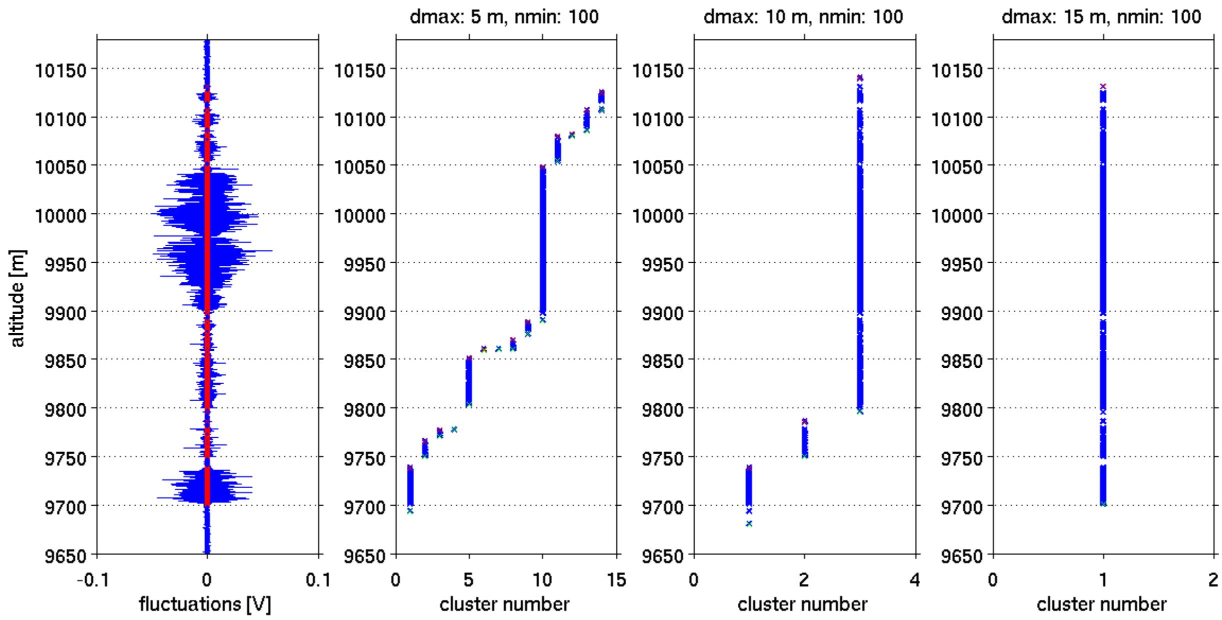

Figure 4.3.: Turbulent region obtained during the BEXUS 6 flight and the result of the cluster algorithm with different parameter combinations. Panel a) shows the fluctuations within the wind field (blue) and the points marked as turbulent by the preprocessing (red). Panels b), c), and d) present the clusters identified for $d = 5$ m and $n = 100$, $d = 10$ m and $n = 100$, and for $d = 15$ m and $n = 100$. For more details see text.

The example demonstrates the difficulty in determining the beginning and ending of a turbulent event. It raises the question of the minimum or maximum possible thickness of a turbulent event or which single turbulent layers belong to the same turbulent event. Answers can only be obtained by relating the cluster results with atmospheric background data provided by e.g. the radiosonde. Such geophysical analyses are the subject of the next Chapt. 5. However, the cluster algorithm is an effective method to get an overview of the turbulent layers within the measured profile of temperature and wind fluctuations. Furthermore, it is important to note that due to the limited knowledge of stratospheric turbulence, the statistics obtained with the cluster algorithm contain completely new insights in e.g. the distribution and depths of turbulent layers as well as the difference between their occurrence in the wind and temperature field.
However, in order to valuate the results of the cluster algorithm, the first step is to investigate

how sensitive are the results of the algorithm to the predefined parameters d and n, i.e. the assumptions made about the density of turbulent points. Hence, the algorithm has been applied to the same data set with different parameter combinations. Figure 4.4 shows the result of the cluster algorithm where the distance parameter d has been kept constant, i.e. 5 m, and only the minimum number of neighbors has been changed from 100 to 1000. Obviously, for all values of n the number of turbulent layers decreases for increasing layer thicknesses. Looking at the single n-classes more thick layers are found at low n-numbers. This is consistent with the fact that for lower values of parameter n less turbulent data points within distance d are needed to form a cluster. Consequently, altitude regions with a lower concentration of turbulent data points can lead to bigger clusters. In other words, the smaller the values of n, the higher the number of thick turbulent layers, i.e. turbulent layers with a thickness of more than 100 m. Accordingly, higher values for parameter n lead to more and thinner turbulent layers. This is also evident from Fig. 4.4, where the number of turbulent layers with a thickness smaller than 10 m increases for higher values of n. In summary, the smaller n, the higher the number of thicker layers and vice versa.

Now the variation due to a varying distance parameter d is examined. In Fig. 4.5 the cluster

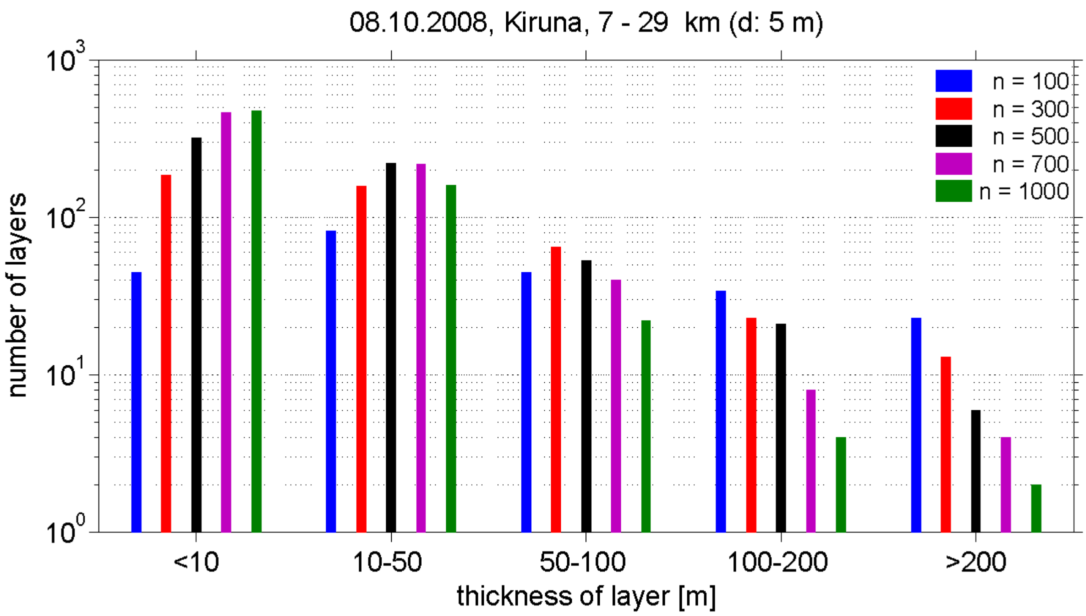

Figure 4.4.: Sensitivity study of the cluster algorithm: The cluster algorithm has been applied with a constant distance parameter d to the complete profile of velocity fluctuations of the BEXUS 6 flight. The results for the different values of parameter n (minimum number of neighbors) are plotted as bars for the classified vertical thickness of identified clusters, i.e. turbulent layers.

results are shown for a constant $n = 300$ and different values for the distance parameter d. The number of identified turbulent layers is plotted against five groups with different vertical thicknesses of the turbulent layers.

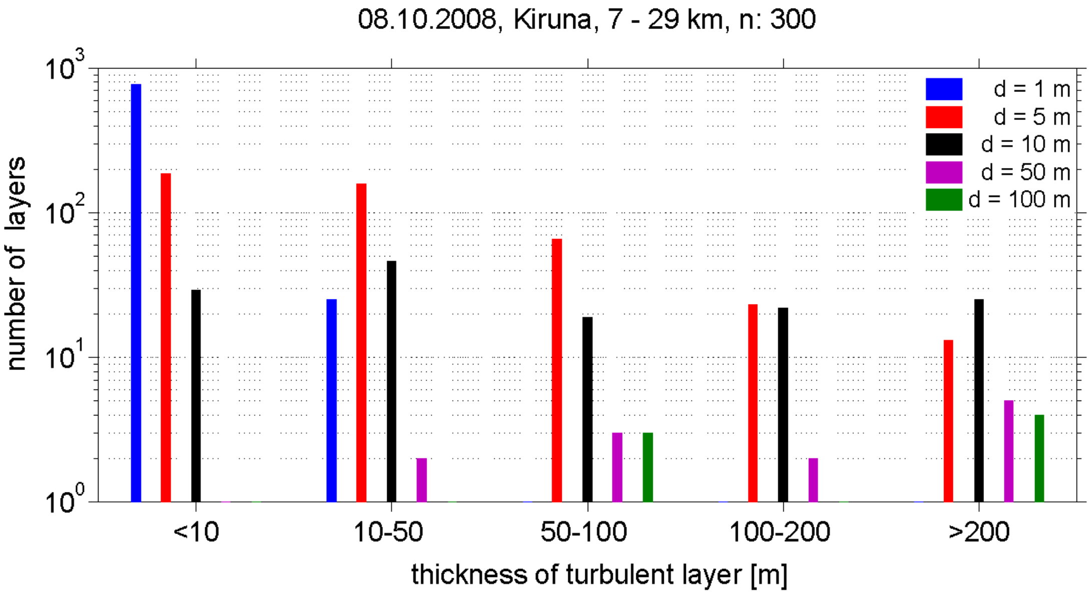

Figure 4.5.: Sensitivity study of the cluster algorithm: Result of the cluster algorithm for a constant minimum number of neighbors (n) and a changing distance parameter d. All clusters (i.e. turbulent layers) identified within the profile of velocity fluctuations of the BEXUS 6 flight where classified depending on their vertical thicknesses.

Obviously, for $d = 1$ m (blue) only turbulent layers with a thickness smaller than 50 m have been classified. That means that the distribution of turbulent points is not that dense to find larger altitude ranges with 300 turbulent points per meter. The most turbulent layers have been identified for a distance parameter of 5 m (red). Here, the cluster algorithm found turbulent layers for all groups of turbulent layers with a thickness from < 10 m and up to > 200 m. A similar amount of layers yields only a distance of 10 m. The higher the distance parameter d, the lower the number of thin turbulent layers. This follows from the fact, that thinner turbulent layers could be merged to thicker turbulent regions for increased values of d. Hence, a distance parameter of 5 m or 10 m seems to be able to cover all five turbulent layer groups. But one question still remains: What is the best combination of d and n to obtain a representative turbulent layer thickness and distribution?
By considering the statistics of turbulent points per meter a nice possibility is found to answer this questions. In a first step, the mean ascent rate of the BEXUS 6 gondola has been calculated, namely $\sim$ 4.45 m/s. Since the voltage signal was sampled at a rate of 2 kHz, 2000 data points were obtained for 4.45 m. Now the amount of data points for the specific distance parameter d is calculated. Table 4.1 shows the result for $d = 1$ m, 5 m, and 10 m. The result of the preprocessing enables the determination of the percentage of data points marked as turbulent of the total amount of data points, namely 49% for the troposphere and 17% for the stratosphere. Using these values, the number of turbulent data points for each individual distance parameter (column 2) has been calculated for the tropospheric and

for the stratosphere region. Since the cluster algorithm should be applied to the complete profile at once and in order to retrieve correct results for the troposphere and stratosphere, the following analyses have been performed with stratospheric values. Hence, the value for the minimum number of neighbors n has been derived from column 4.

Table 4.1.: Based on the mean ascent rate of the BEXUS 6 gondola (4.45 m/s) the number of measured data points within 1 m, 5 m, and 10 m have been assessed by means of the sampling frequency of 2 kHz (i.e. 2000 data points within 4.45 m). The percentage of points marked as turbulent by the preprocessing has been determined individually for the tropospheric region (7–15 km), i.e. 49% and for the stratospheric region (15–29 km), i.e. 17%. These values have been used to calculate the percentage of turbulent data points for both height ranges based on the values in column 2. The results are shown in column 3 and 4 and the last column contains the derived value for the parameter n.

parameter d	data points	turbulent data points troposphere (49%)	turbulent data points stratosphere (17%)	parameter n
1 m	449	220	76	70
5 m	2247	1101	382	300
10 m	4494	2202	763	700

A similar statistic has been compiled for the 8 kHz CCA signal of the BEXUS 8 flight and the results are summarized in Tab. 4.2 for the tropospheric and stratospheric region.

Table 4.2.: Analogous statistic for the temperature sensor BEXUS 8 flight. Based on the mean ascent rate of the gondola ($\sim$ 4.7 m/s) and the sampling rate (8 kHz), the amount of data points for parameter d in column 1 have been determined. During the preprocessing, data points have been marked as turbulent and their percentage have been calculated for the troposphere (8 %) and for the stratosphere (15 %). These values have been adopted to column 2 in order to obtain the turbulent data points for the troposphere (column 3) and stratosphere (column 4). The last column contains the result for the parameter n.

parameter d	data points	turbulent data points troposphere (8%)	turbulent data points stratosphere (15%)	parameter n
d = 1 m	2235	179	335	100
d = 5 m	11173	894	1676	800
d = 10 m	22346	1788	3352	1700

The choice of the parameter combination of d and n used for the following analyses is based on geophysical considerations and on the performed sensitivity studies of the cluster algorithm. A value of 1 m for the distance parameter d leads to depths of the turbulent layers solely smaller than 50 m, while for $d = 100$ no turbulent layers thinner than 50 m and with a thickness between 100 m and 200 m have been identified (see Fig. 4.4). Hence, both values yield only one-sided results for the depths of the turbulent layers. That means that for $d = 1$ m, the distance between the turbulent layers must be quite small (≤ 1 m) in order to get thicker turbulent layers. But measurements performed by e.g. *Barat* [1982a] reveal, that especially in the stratosphere the distance between the turbulent layers is certainly > 1 m. On the other hand, for $d = 100$ more thin turbulent layers have been merged to bigger clusters, even though the distance in between can reach 100 m. Hence, the results are less objective than for a lower value of d. However, based on geophysical considerations and the sensitivity studies, a distance parameter of $d = 5$ m seems to be appropriate to give representative results of the cluster algorithm. As already explained above, the choice of n depends on the statistics presented in Tab. 4.3 and Tab. 4.4. Besides this statistic, the sensitivity study reveals that the value of n is less critical than for d. Hence, n has been set to 300 for BEXUS 6 or 800 for data sampled with 8 kHz during BEXUS 8.

4.2.1. Statistic of turbulent layers observed during BEXUS 6

In the previous section the cluster algorithm has been described as well as the statistical determination of d, the distance parameter and n, the minimum number of adjacent turbulent data points.

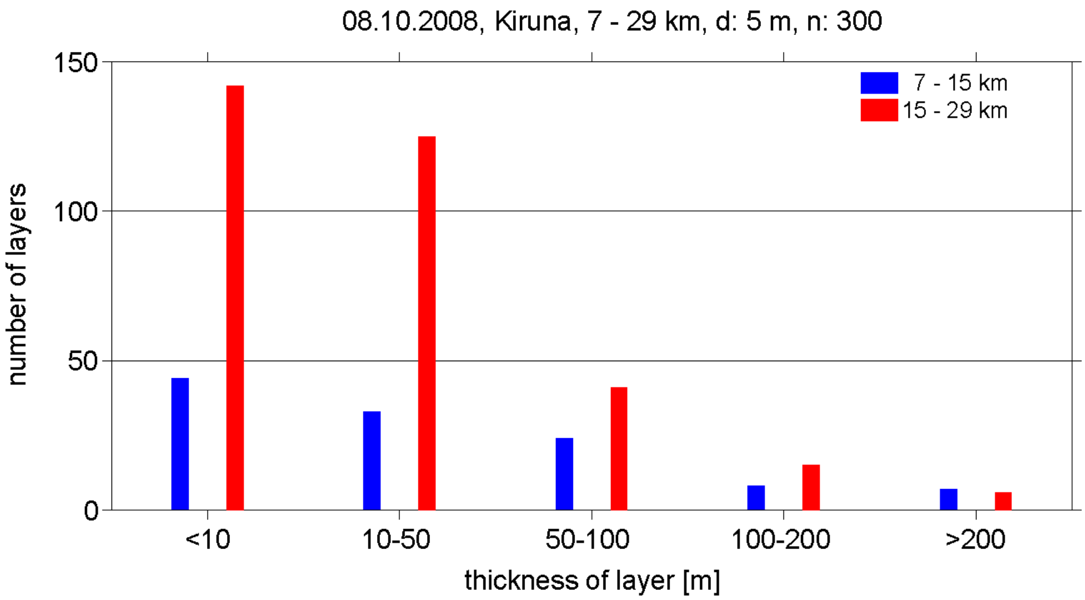

Figure 4.6.: Number of turbulent layers identified within the profile of wind fluctuations during the BEXUS 6 flight. The profile is analyzed separately for the troposphere (blue) and the stratosphere (red). Depending on their vertical thickness, the turbulent layers are classified into 5 groups.

With $d = 5\,\mathrm{m}$ and $n = 300$ the cluster algorithm has been applied to the profile of wind fluctuations of the BEXUS 6 flight. The resulting turbulent layers are divided into five groups depending on their thickness. In Fig. 4.6 these groups are plotted against the number of layers per group. The blue bars show the results for the tropospheric region (7–15 km) and the red bars for the stratosphere (15–29 km). Clear differences appear in the groups for layer thicknesses smaller than 10 m and between 10 m and 50 m, where almost three times more turbulent layers have been found in the stratosphere than in the troposphere. The differences decrease for an increasing layer thickness, so that the smallest difference occurs for turbulence with a vertical thickness of more than 200 m. However, for both regions, considerably more thin layers than thick layers are detected. For the troposphere 115 turbulent layers and for the stratosphere 330 layers are identified, resulting in 445 turbulent layers for the complete profile of wind fluctuations.

Figure 4.7 shows the thickness of all turbulent layers against the altitude where each layer begins. Here, the difference between troposphere and stratosphere is not that easily recognizable as in Fig. 4.6. In the stratosphere above 20 km, a higher number of turbulent layers with a thickness smaller than 50 m have been found. Furthermore, a slightly decreasing number of thicker layers with altitude can be noticed. Besides these findings, turbulent layers with a varying vertical thickness have been detected within the troposphere as well as within the stratosphere. In order to quantify the turbulent layer statistics, the maximum, minimum and mean thickness, as well as the maximum, minimum and mean distance between the layers have been calculated for the troposphere, stratosphere and for the complete altitude profile. Accordingly, Tab. 4.3 shows the result for the wind fluctuations of the BEXUS 6 flight.

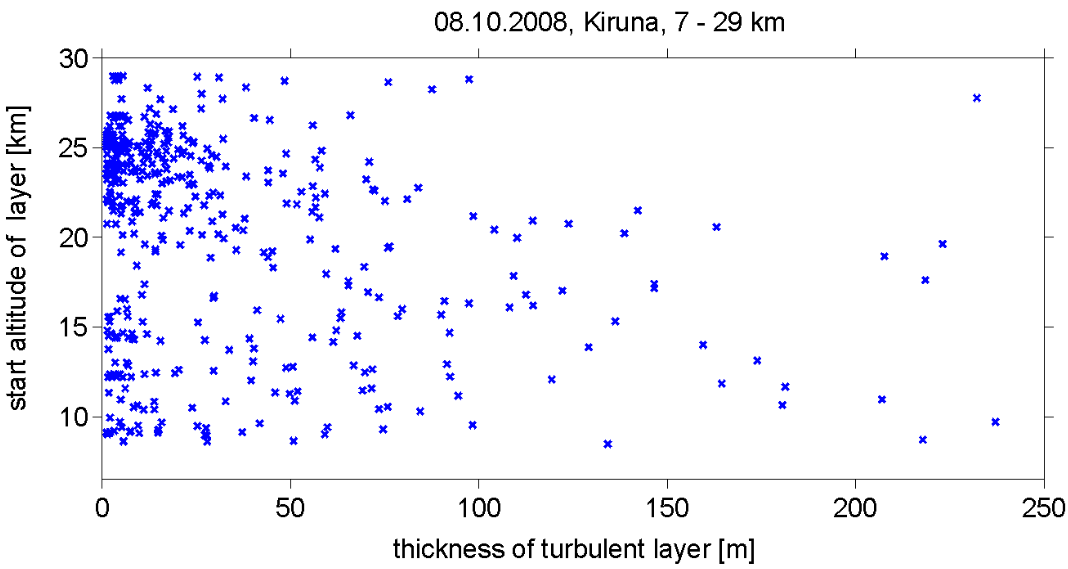

Figure 4.7.: The vertical thickness of all identified turbulent layers within the wind field during BEXUS 6 plotted against the altitude, where each turbulent layer begins.

On average, turbulent layers in the wind field of the BEXUS 6 flight are 38.2 m thick. If the profile is separated into troposphere and stratosphere, thinner layers (29.8 m) have been detected in the stratosphere, while in the troposphere the turbulent layers are 62 m thick on average, i.e. twice as thick. The mean distance of nearly 70 m in the troposphere indicates that the layers are further apart from each other compared to the stratosphere, where a mean distance of 41.9 m has been obtained. The maxima of thickness and distance show a similar behavior. Here the values for the troposphere are about three times higher than in the stratosphere.
Summarizing the results of the cluster algorithm for the BEXUS 6 flight, more turbulent layers have been observed within the stratosphere and they are only half as thick as in the troposphere.

Table 4.3.: Characteristics of the turbulent layers obtained for the wind fluctuations of the BEXUS 6 flight with the cluster algorithm. Maximum, minimum and mean values were determined for the troposphere (column 2), the stratosphere (column 3) and the complete profile (column 4).

	7000–15000 m	15000–29000 m	7000–29000 m
maximum thickness (m)	1464.4	413.3	1464.4
minimum thickness (m)	1.3	1.1	1.1
mean thickness (m)	62.0	29.8	38.2
maximum distance (m)	1474.6	500.7	1474.6
minimum distance (m)	1.7	1.3	1.3
mean distance (m)	68.6	41.9	49.5

4.2.2. Statistic of turbulent layers observed during BEXUS 8

During the BEXUS 8 flight profiles of both wind and temperature fluctuations have been obtained. A statistic for the data sets has been compiled which yields an overview of the detected turbulent layers. Based on Tab. 4.2 the cluster algorithm has been applied with $d = 5$ m and $n = 300$ to the 2 kHz sampled data and $n = 800$ to the 8 kHz sampled data.
Since the wind fluctuations during BEXUS 8 have been measured with two individual CTA sensors (one sampled with 2 kHz and the other with 8 kHz), the cluster algorithm has been applied to both data sets with the appropriate parameters. Only the turbulent layers detected with both sensors have been used for the further analyses. In Fig. 4.8 the resulting number of turbulent layers within the wind field has been plotted against five groups of thickness ranges for the troposphere (blue) and stratosphere (red). Likewise the result of BEXUS 6, a larger number of turbulent layers with a thickness smaller than 50 m have been detected within the stratosphere compared to the troposphere. There are nearly twice as many stratospheric turbulent layers in the group 10 m–50 m than tropospheric layers. Furthermore, one can notice that the thicker the layer gets, the less becomes the number of detections. Within the troposphere 102 and within the stratosphere 178 turbulent layers

have been identified. In total, 280 turbulent layers were measured, which are considerably less than during BEXUS 6. Furthermore, an increase of the number of turbulent layers can be observed between the first group (< 10 m) and the second group (10 m–50 m). The contrary result has been obtained for the BEXUS 6 flight, where the number of layers decreases from the first to the second group of layer thicknesses.

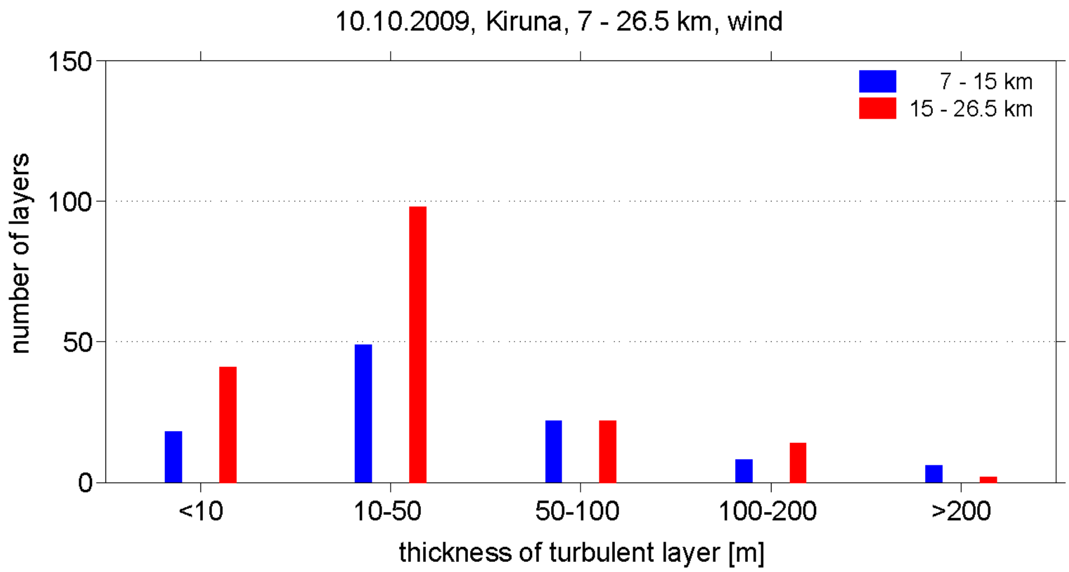

Figure 4.8.: Determined number of turbulent layers within the wind field of the BEXUS 8 flight for the troposphere (blue) and stratosphere (red). The calculated layer thicknesses have been divided in five classes.

Figure 4.9 shows the thickness over the starting altitude of each turbulent layer. Similar to BEXUS 6, a slight tendency towards a decrease of thick layers and towards a higher number of turbulent layers with depths < 50 m above 20 km can be noticed. Furthermore, as Fig. 4.8 has already shown, the number of thin layers is generally higher than the number of thicker layers.

The cluster algorithm has also been applied to the BEXUS 8 profile of temperature fluctuations. Again, the thickness of the turbulent layers has been split into groups and plotted over the number of layers for each group in Fig. 4.10 individually for the troposphere (blue) and stratosphere (red). Obviously, a similar behavior as for the turbulent layers within the wind field can be observed for the temperature field. Within the stratosphere the number of thinner layers is higher compared to the troposphere and only half of the number of turbulent layers smaller than 10 m in the stratosphere have been observed in the troposphere. Generally, there are more stratospheric turbulent layers in all groups than tropospheric layers, but the difference is smaller compared to the results for the wind profiles of BEXUS 6 and BEXUS 8. On the other hand, in contrast to the turbulent layers within the wind field, no turbulent layer with a vertical thickness above 200 m has been identified.

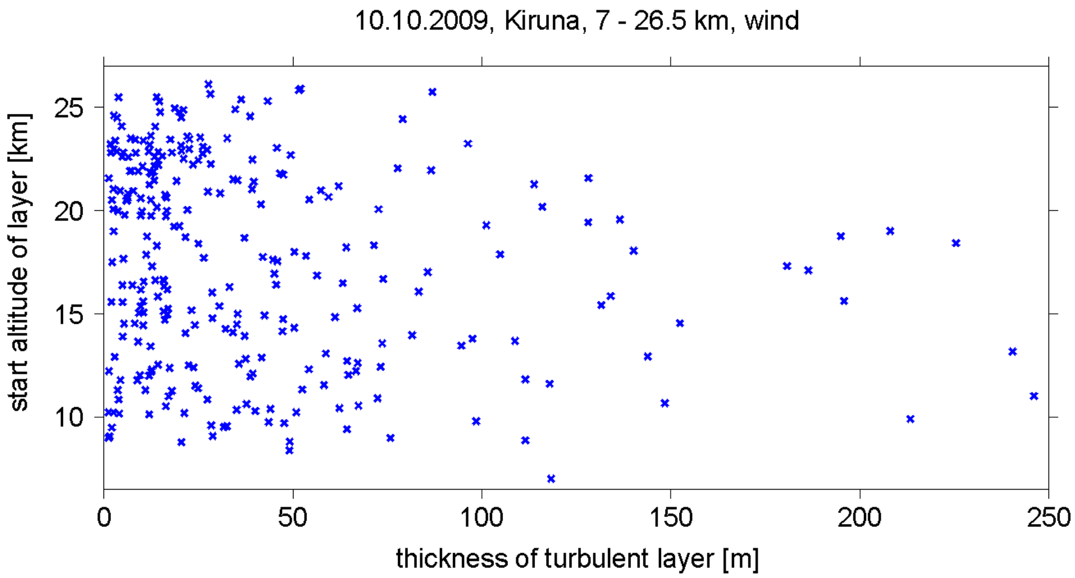

Figure 4.9.: All identified turbulent layers of the BEXUS 8 wind field with their depths against the start altitude of each layer.

The individual thickness of all turbulent layers in the temperature field is plotted against their starting altitude in Fig. 4.11. More or less no variation with altitude can be observed. Furthermore, it can easily be seen that most of the layers are thinner than 50 m and that there are considerably less turbulent layers with a higher vertical thickness. In fact, no turbulent layers thicker than 150 m have been detected. In order to quantify this statement, Tab. 4.4 contains the extremes and mean values for the layer thickness and the distance between the layers for the wind field as well as for the temperature field.

For the turbulent layers within the wind field an averaged depth of 46.4 m has been determined. A splitting into stratosphere and troposphere shows that thinner layers have been found in the stratosphere (36 m) in comparison with the troposphere (64.6 m). Looking at the results for the temperature field, the turbulent layers have been only half as thick as for the wind field, namely 24 m. Furthermore, in contrast to the wind, the mean thickness of turbulent layers in the troposphere (24.9 m) is almost identical with the thickness in the stratosphere (23.4 m). The maximum values are particularly different for both fields. For instance, in the stratosphere wind field turbulent layers with a maximum thickness of 225.6 m have been identified, whereas in the temperature field the turbulent layers are only 139 m thick at maximum. The difference within the troposphere (7 km - 15 km) is even higher. Here the thickest turbulent layer within the temperature field is 146.6 m and the thickest turbulent wind layer 1237.3 m. Comparing the maximum distances between the turbulent layers, one can notice that the turbulent wind layers in the stratosphere are closer together than in the troposphere. Exactly the opposite is the case for the turbulence in the temperature field. Here the higher distance is found in the stratosphere. On average, a distance

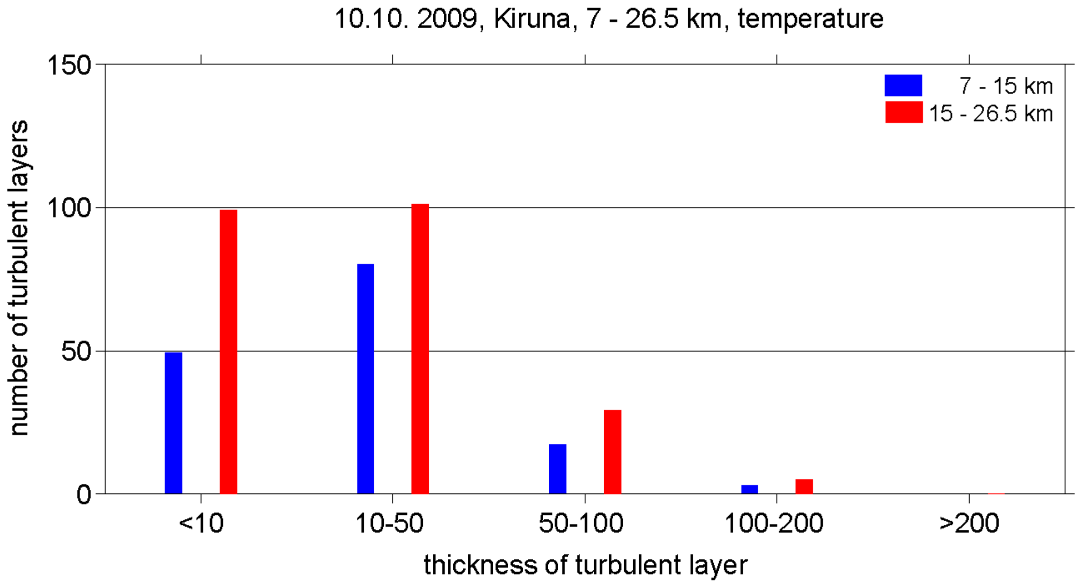

Figure 4.10.: Identified turbulent layers within tropospheric (blue) and stratospheric (red) temperature field of BEXUS 8. Their vertical depths have been classified and the number of layers per group were counted.

of 68.5 m has been obtained for the complete profile of wind fluctuations and 50.9 m for the temperature fluctuations.

Finally, the values for the turbulent layers within the wind field of the BEXUS 8 flight have been compared with the values of the BEXUS 6 flight. During both flights thinner turbulent layers have been observed in the stratosphere and also the distances between the layers were smaller above 15 km. Besides the fact that all individual values for the thicknesses and distances have the same order of magnitude for BEXUS 6 and BEXUS 8, the most remarkable point is the small difference of the mean thicknesses between both flights. For the complete profile of wind fluctuations the mean thickness of the BEXUS 8 flight amounts to 46.4 m and is therewith just $\sim$8 m larger than the mean thickness of the BEXUS 6 flight. In particular, within the troposphere the mean layer thickness of BEXUS 6 differs by only 2.6 m from the BEXUS 8 flight. The similarity between the BEXUS 6 and BEXUS 8 results as well as the difference between the identified temperature and wind layers demonstrate nicely, that the results are no artifacts of the cluster algorithm.

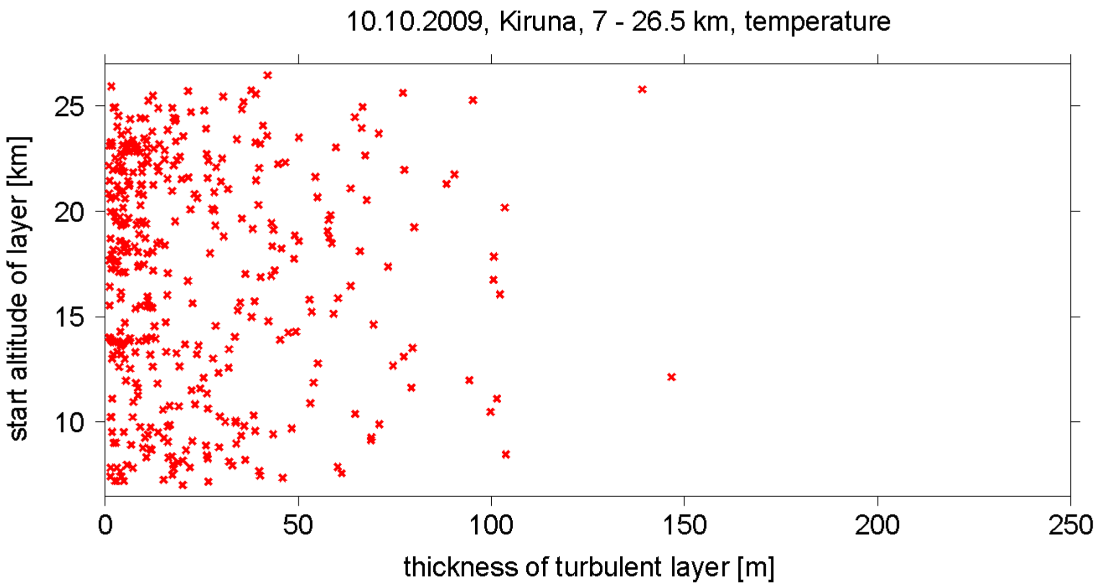

Figure 4.11.: The thickness of the temperature layers observed during BEXUS 8 plotted against the start altitude of the layers.

Table 4.4.: Statistic of the turbulent layers observed within the wind and temperature field during BEXUS 8. Individual values have been determined for the maximum, minimum and mean thicknesses and distances. Column 2 contains the results for the troposphere, column 3 for the stratosphere and column 4 presents the results for the complete profile.

		7000 – 15000 m	15000 – 26500 m	7000 – 26500 m
wind	maximum thickness (m)	1237.3	225.6	1237.3
	minimum thickness (m)	1.3	1.3	1.3
	mean thickness (m)	64.6	36.0	46.4
	maximum distance (m)	1243.8	440.8	1243.8
	minimum distance (m)	1.4	1.3	1.3
	mean distance (m)	79.2	62.6	68.5
temperature	maximum thickness (m)	146.6	139.0	146.6
	minimum thickness (m)	1.1	1.0	1.0
	mean thickness (m)	24.9	23.5	24.0
	maximum distance (m)	252.8	529.0	529.0
	minimum distance (m)	1.7	1.33	1.3
	mean distance (m)	54.2	48.4	50.9

4.2.3. Comparison of the cluster analysis results with other measurements

In the literature only little information is given concerning the vertical thickness of turbulent layers in the stratosphere or the distance between the layers. This means that the results of the cluster algorithm provide not only new insights in the distribution and thicknesses of the turbulent layers but also offer the possibility to compare the occurrence of turbulent layers within the wind and temperature field.
During the 1980s pioneering balloon measurements studying stratospheric turbulence were performed by e.g. *Barat and Aimedieu* [1981]; *Barat* [1982a, b]; *Barat and Genie* [1982]. Their observations reveal vertical depths of the turbulent layers ranging from less than 50 m up to 800 m. Another paper by *Sato and Woodman* [1982] shows radar measurements of thin stratospheric turbulent layers. The thickness were usually less than the altitude resolution of the radar, so that they could only estimate the vertical depth to be less than 150 m. But from a zenith-swinging experiment they got an average value of about 50 m. Additionally, they determined a vertical separation between the turbulent layers from a few to several hundred meters. The measurements obtained with LITOS yield similar results for the vertical thicknesses as well as for the distance between the layers. But in contrast to the earlier observations, a more detailed statistic has been achieved with LITOS.

4.3. Spectral analysis of turbulent fluctuations

In Sect. 4.1 examples of turbulent layers within the temperature and wind field have been shown. However, it needs to be verified that the observed layers in the raw data field are really turbulence and not regions of e.g. increased noise or other instrumental artifacts. In order to answer this question, the spectrum of the fluctuations has been calculated and compared with the turbulent spectrum expected from theory.
Before calculating the individual spectrum, large scale disturbances (e.g. gondola movements) were removed from the raw data signal by subtracting a spline trend. Afterwards, Welch's method has been applied to obtain the power spectral density values [*Welch*, 1967]. Welch's method divides a data segment into overlapping sections, calculates the periodogram of each section and finally averages those periodograms to estimate the power spectral densities of the complete data segment. The great advantage of this method is, that it reduces the variance of the estimation of the power spectral densities and therefore provides results with a higher accuracy compared to other methods like e.g. the Bartlett method. Within spectral analyses a smearing of the signal energy over a wide frequency range could appear, due to the fact, that the sampled section does not end with exactly the same period as it has started. This phenomenon is called spectral leakage and can be reduced by applying window functions. Accordingly, during the calculation of the periodogram of each section a Hann window has been used. As a typical example, Fig. 4.12 presents the spectrum of wind fluctuations for the turbulent region between 19310 m and 19350 m of the BEXUS 8 flight (see Fig. 4.2). The spatial scale L has been derived from $L = 2\pi/k = v_\mathrm{b}/f$ (k = wavenumber, f = frequency, v_b = balloon ascent velocity). An $m^{-5/3}$ slope is well identified between spatial

scales of 10 m and 0.1 m as well as the transition to an m^{-7} slope below 0.08 m. Hence, the observed slopes agree nicely with the slopes expected from theory, which have been discussed in Sect. 2.1.2. The noise level of the CTA system starts at a power spectral density value of $\sim 10^{-7}$ V/s. This demonstrates that LITOS has the required resolution and sensitivity to cover the inertial subrange and part of the viscous subrange. Until now, there is no other instrument known with such a high resolution for wind and temperature measurements in the stratosphere. Consequently, these are the first in-situ measurements of turbulent spectra down to the viscous subrange in the stratosphere!
For comparison, the spectrum of the non-turbulent region between 19250 m and 19280 m (see Fig. 4.2) is shown in Fig. 4.13. In contrast to the turbulent spectrum, the slope does not follow the characteristic $m^{-5/3}$ behavior. The power spectral densities for scales smaller than 3 m are much lower than in the turbulent case and basically show instrumental noise. At small spatial scales ($\lesssim 0.02$ m) there are still some apparent irregularities (in both spectra) presumably due to electronic disturbances. But they do not hamper the spectral analysis. Since the BEXUS gondola is not stabilized, slow rotation occurs (see appendix D). That pendulum and rotation would cause distinct peaks in the spectrum at lower frequencies ($\sim$ 1 Hz). The measured spectra show no significant signal at that frequency.

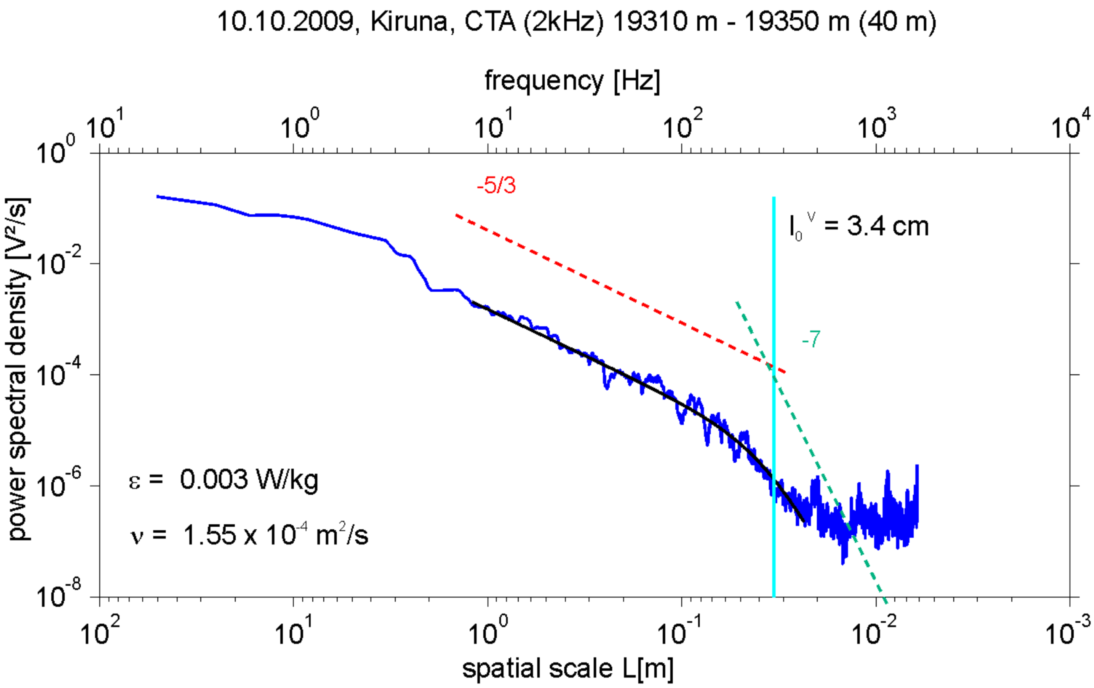

Figure 4.12.: Turbulent spectrum of velocity fluctuations for a 40 m altitude interval obtained during the BEXUS 8 flight. The black line shows the theoretical fit based on the Heisenberg model. An inner scale of 3.4 cm and an energy dissipation rate of 3 mW/kg have been determined.

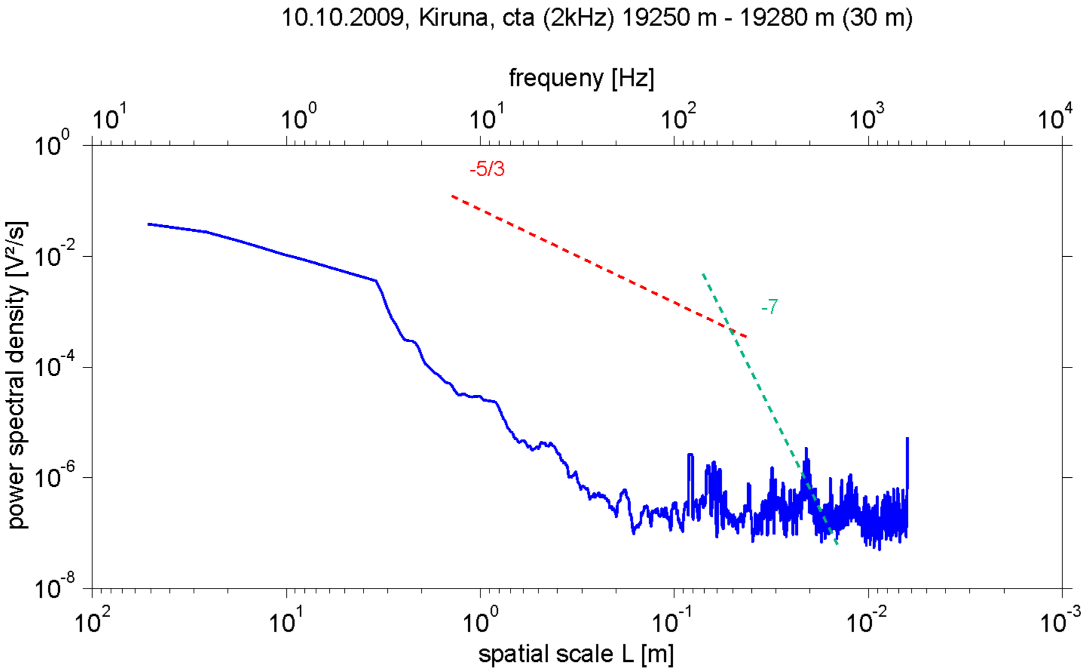

Figure 4.13.: Spectrum of an non-turbulent region of velocity fluctuations during the BEXUS 8 flight. In contrast to the turbulent spectrum (Fig. 4.12) no $m^{-5/3}$ or m^{-7} slope has been observed.

During the BEXUS 8 flight not only wind turbulence but also turbulent structures within the temperature field have been observed. Accordingly, also the spectra of temperature fluctuations have been studied. Figure 4.14 shows an example of a turbulent spectrum of temperature fluctuations, which has been calculated for the altitude region 19300 m to 19313 m (shown in Fig. 4.2). The spectral behavior corresponds very well with the theoretical slope, which has been described in Sect. 2.1.2. Looking at the inertial subrange, an $m^{-5/3}$ slope exists between 2 m and 0.04 m which proceeds to an m^{-7} slope within the viscous subrange, i.e. below 0.02 m. Similar to the velocity spectrum, the instrumental noise starts at a power spectral density value of $\sim 10^{-7}$ V/s, but it apparently shows less disturbances than the noise of the CTA system. Obviously, the CCA system seems to be less susceptible to e.g. movements of the gondola or electronic disturbances by other systems or telemetry. A complete CCA noise spectrum is shown in Fig. 4.15 for a non-turbulent region between 19260 m and 19290 m. As expected, the spectrum does not contain a slope indicating turbulence, i.e. neither an $m^{-5/3}$ slope nor an m^{-7} slope arises in this altitude region.

Based on the spectral analyses one of the most essential turbulence parameter can be determined, namely the energy dissipation rate ε. The energy dissipation rate is normally used to estimate the turbulence effect on e.g. atmospheric dynamics, chemistry and coupling. For the calculation of the energy dissipation rate the method of *Lübken* [1992] and *Lübken et al.* [1993] has been adopted. The mathematical implementation of this method is briefly de-

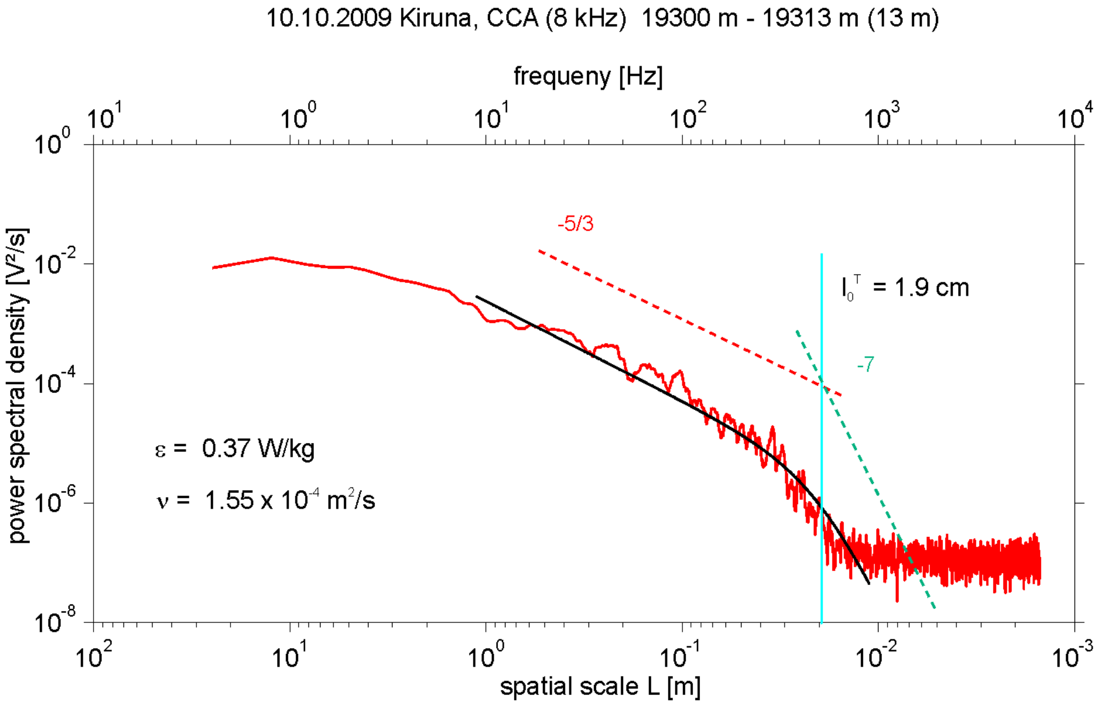

Figure 4.14.: Example of a turbulent spectrum calculated for temperature fluctuations measured during the BEXUS 8 flight. The Heisenberg model has been fitted to the spectrum (black line) in order to determine the inner scale (1.9 cm) and the energy dissipation rate (0.37 W/kg).

scribed here, while the theoretical background is found in Sect. 2.2.5.
In order to obtain ε the Heisenberg model (Eq. 2.24) has been fitted to the measured spectrum using the equation for the inner scale l_0 for velocity fluctuations (Eq. 2.33) or for temperature fluctuations (Eq. 2.41). The kinematic viscosity has been calculated based on the radiosonde data. For the fitting routine, the least mean square method from Matlab (lsqcurvefit) has been applied. The best fitting result yields the inner scale l_0 which in turn determines the turbulent energy dissipation rate ε. As an example the best fit model has been plotted as a black line to the spectrum in Fig. 4.12. The theoretical fit agrees nicely with the measured spectrum and an inner scale l_0 of 3.4 cm has been obtained. Based on this value the energy dissipation rate has been determined as 0.003 W/kg. Similarly, the black line in Fig. 4.14 represents the best fit of the Heisenberg model to the measured spectrum of temperature fluctuations. Again, the model corresponds quite well with the observed spectrum. The result for the inner scale l_0 is 1.9 cm and for the energy dissipation rate $\varepsilon \sim 0.37$ W/kg.

4.3.1. Accuracy of the determination of the energy dissipation rate

The applied method to calculate the energy dissipation rate depends crucially on the accuracy of the determination of l_0. Small errors in l_0 lead to significant uncertainties of ε,

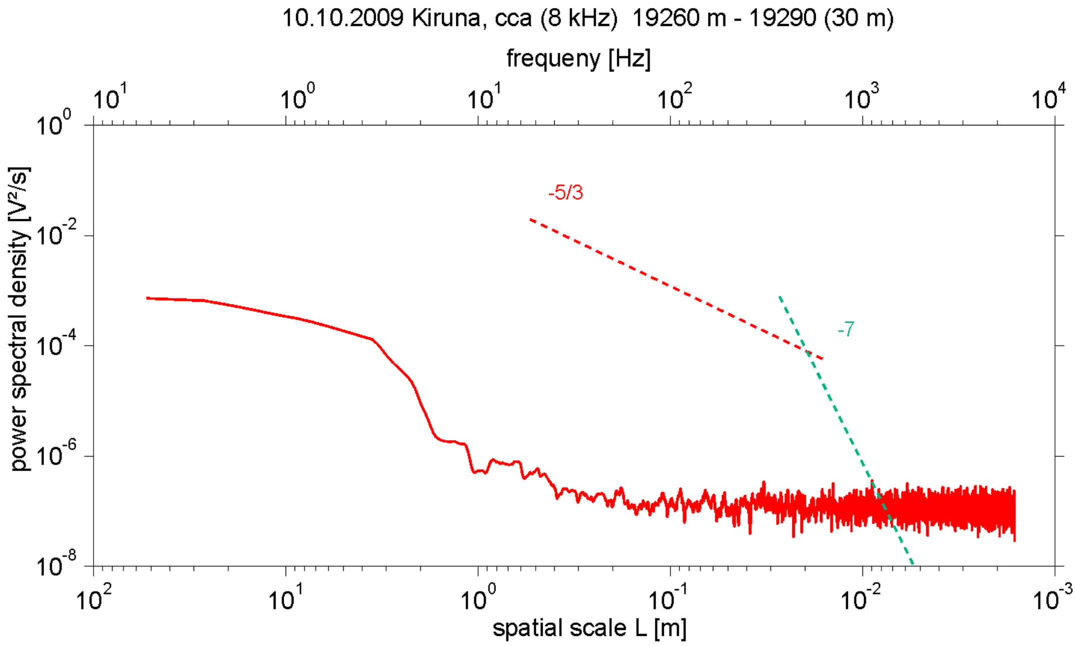

Figure 4.15.: Spectrum of a non-turbulent region within the profile of temperature fluctuations during BEXUS 8. The noise level shows no large disturbances at all.

because $l_0 \propto \varepsilon^{1/4}$. A possible uncertainty within the determination of l_0 is the conversion of frequency scales into spatial scales which can be affected by the relative movement of the gondola. For that reason an accelerometer has been included in the LITOS payload. However, for the conversion the particular ascent rate is used, which is modulated by the relative horizontal wind by the root of the sum of squared velocities (vertical and relative horizontal). For the BEXUS 6 launch an error of the inner scale due to ignorance of relative horizontal wind of ~10% has been estimated resulting in 30–50 % error in ε. This error can possibly be reduced by careful analysis of the acceleration data. A second error source is the fact, that the data sequence taken for a single turbulence spectrum is not necessarily filled with homogeneous turbulence. Typically spectra are calculated from 40–100 m sections of data. The turbulent layer has to fill a large part of this section to produce a clear spectral signal. Inhomogeneous turbulence might result in some smearing of the spectra especially in the transition region of inertial and viscous subrange even for this high resolved observations. By this the determination of the inner scale might be affected and thus also the energy dissipation rate. For turbulent layers thinner than 40–100 m a maximum error of ~ 10 % is assumed for the inner scale, similar to the factor induced by ignoring the relative horizontal wind. Nevertheless, it should be pointed out that in contrast to other methods (e.g. structure function method, see Sect. 2.2.4), the calculation of ε does not depend on absolute spectral densities (which may be affected by changing instrument sensitivities) or more or less unknown "constants", but only on the precise measurement of the temporal variations. The range of ε values which can be observed with LITOS vary between 2.1×10^{-6} W/kg (max-

imum l_0 of 1 m) and 5.3 W/kg (minimum l_0 of 0.025 m). It should be emphasized that this range of energy dissipation rates can be measured by LITOS from the boundary layer up to the middle stratosphere, as the noise level is constant with altitude. Furthermore, up to know a sub-cm measurement resolution has not been achieved within the stratosphere and LITOS therefore provides the possibility to determine the energy dissipation rate with a precision that has not been achieved so far in the stratosphere.
In the next section profiles of the energy dissipation rate for the BEXUS 6 and BEXUS 8 flight will be shown, which have been obtained based on the fitting procedure described here.

4.4. Measured profiles of energy dissipation rate

In order to obtain a complete profile of ε the data set is divided into segments by a moving window of 5 s, i.e. 25 m (assuming a balloon ascent rate of 5 m/s) with an overlap of 2 s, i.e. 10 m. For each segment, the spectrum is calculated based on Welch's Method [*Welch*, 1967], see also Sect. 4.3). After evaluating whether the spectrum is turbulent or not by means of the individual noise characteristic, the Heisenberg model is fitted to the turbulent spectrum. The resulting ε value is assigned to the mean altitude of the segment. For the non-turbulent spectra ε is assigned as zero. Thus, a profile of the energy dissipation rate with a step size of 10 m for the complete altitude profile is obtained. In the following, the ε profile for the BEXUS 6 and BEXUS 8 flight will be presented and discussed in relation to the atmospheric background conditions during each flight.

4.4.1. BEXUS 6

Figure 4.16 shows the energy dissipation rate ε from 7 km up to 29 km for the BEXUS 6 flight on 8 October 2008 from Kiruna. It can easily be seen, that the energy dissipation rate increases with altitude. Accordingly, the lowest value of $1.45 \times 10^{-}6$ W/kg has been measured below 16 km and the highest value of 1.81 W/kg above 25 km, respectively. Hence, the values of the energy dissipation rate cover several orders of magnitude within an height range of $\sim$ 22 km. The linear regression of $\log \varepsilon$ (red line) reveals an exponential increase of the energy dissipation rate with altitude. In order to get a more detailed picture of the individual turbulent regions, Fig. 4.17 shows again the profile of the energy dissipation rate, but this time in linear scale and divided into three altitude ranges. The left panel presents the altitude region between 7 and 14 km, the middle panel between 14 and 22 km, and the right panel shows the altitude region between 22 and 29 km. It should be emphasized, that due to the height variation of the ε values, the ε-axes have been scaled differently for the three plots to visualize individual turbulent layers within the complete altitude region. Now, the intermittency of the turbulent regions is clearly recognizable by the alternation between regions with high ε values, i.e. turbulent layers, and regions with lower values of ε, i.e. calm regions. Up to 10.3 km the predominant part is characterized by very low energy dissipation rates and only a few smaller turbulent layers stand out of the calm background. Above 10.3 km several distinct turbulent regions have been observed. Especially the turbulent layers at 10.3 km, 11 km, and 12.6 km directly become apparent. Also in between these layers as well as above 12.6 km turbulent layers with lower but varying rates of ε have been detected. Hardly no altitude region can be found here, where there is no turbulent layer. Within the middle panel, i.e.,from 14 km up to 22 km, the increase of the energy dissipation rate is again clearly visible. Hence, higher energy dissipation rates can be found above 19.6 km, while below only a few turbulent layers with ε larger than ~ 0.02 W/kg have been detected. On the contrary, the turbulent layer with the highest ε value in this altitude region is located at 20.4 km. The increase of the energy dissipation rate proceeds also in the altitude region from 22 km up to 29 km (right panel). The turbulent region above 27.5 km raises instantly the attention. Here the highest ε values of the complete altitude profile can be found, namely up to 1.8 W/kg. The two thinner separated turbulent layers at 27.7 km and 28 km are followed by a turbulent region with a higher vertical extension. Hence, the thickest clearly defined turbulent layer of the profile is found between 28.6 km and $\sim$28.9 km. Below this strong turbulence region, i.e. below 27.5 km, more turbulent layers can be found even though they are less pronounced. In summary, the BEXUS 6 profile of energy dissipation rates displays nicely the intermittency of the stratospheric turbulence. Moreover, a significant increase of the ε values with altitude is found.

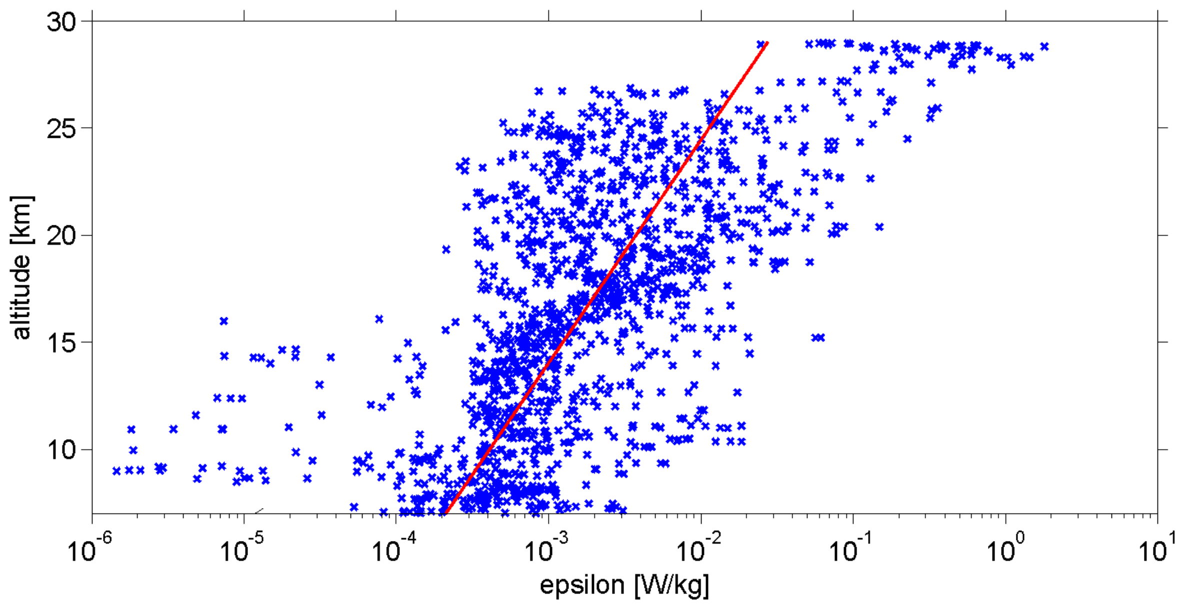

Figure 4.16.: The energy dissipation rate (blue) of the wind fluctuations during BEXUS 6 plotted in a logarithmic scale against the altitude. The red line presents the linear regression of log ε.

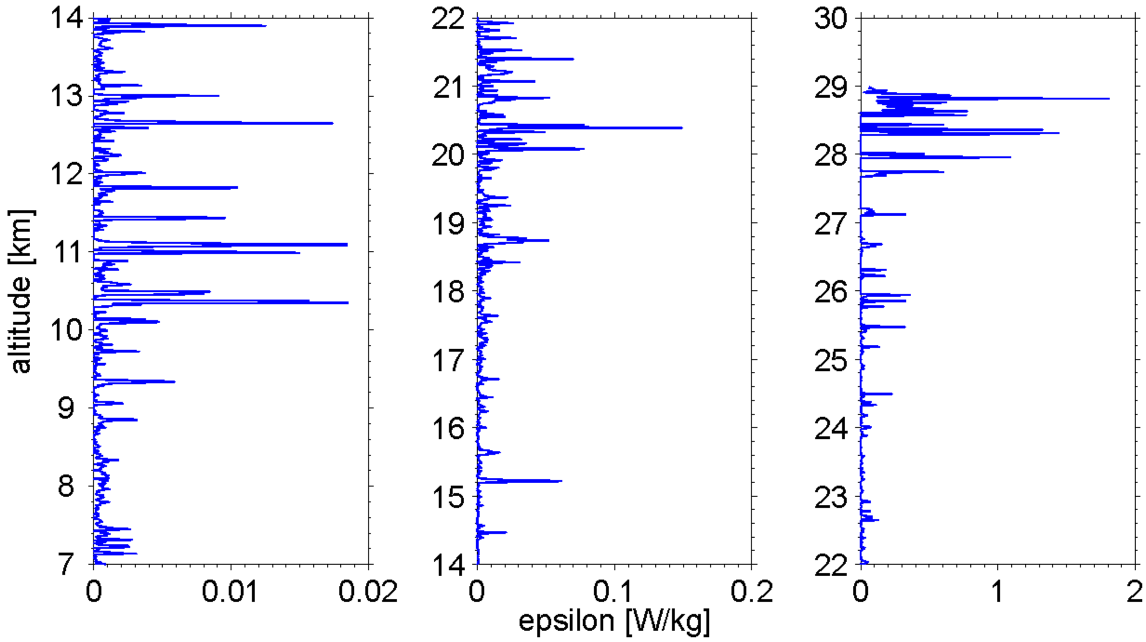

Figure 4.17.: Profile of the energy dissipation rate obtained during BEXUS 6 in a linear scale and divided into three altitude segments to visualize the layered turbulence structure. Due to the high variation of ε, the ε-axes have been scaled different for the three plots.

4.4.2. BEXUS 8

During the BEXUS 8 flight simultaneous measurements of the stratospheric wind and temperature fluctuations have been performed. Accordingly, profiles of the energy dissipation rates for both parameters have been calculated. It should be noted, that two CTA sensors have been used during BEXUS 8 to measure the wind fluctuations and they were located at different corners of the gondola (see Sect. 3.3.3). For the determination of the ε-profile only the turbulent regions detected by both sensors have been included. Figure 4.18 shows the resulting profile for the wind fluctuations. Similar to the BEXUS 6 data, the energy dissipation rate increases with altitude. Thus, the lowest value of 5.12×10^{-6} W/kg has been measured at 7.1 km and the highest value of 0.73 W/kg at 25.8 km, respectively. By means of linear regression analyses of $\log \varepsilon$ (red line), an exponential increase of ε with altitude is manifested which is, however, smaller compared to BEXUS 6. Figure 4.19 shows the energy dissipation rate profile in a linear scale divided into three altitude regions. In the altitude region from 7 to 14 km (left panel) several turbulent layers have been observed. Between 7.5 km and $\sim$ 12.6 km a continuous change between turbulent and non-turbulent region takes place, where the turbulent layers possess different vertical thicknesses. For instance, one of the thickest turbulent layers is located at 10 km, while a more quiet region can be found between 8.6 km and 8.8 km. Longer sections with barely no turbulence have been observed between 11.1 km and 11.6 km and especially between 12.8 km and 13.8 km. The energy dissipation rate within the turbulent layer at ∼13.9 km comprises the highest value within that altitude region. A tendency to higher ε values can also be noticed within the altitude region from 14 to 21 km (middle panel). Furthermore, the intermittency of the detected turbulence can easily be recognized again. Regions with considerably less or even no turbulence dissipation at all (e.g. 16.2— 16.8 km) alternate with turbulent regions (e.g. 18–19 km). Particularly prominent is the turbulent layer just above 16 km, because it has the highest value of ε of 0.42 W/kg (not shown), i.e. nearly eight times higher than almost all other ε values in this altitude range. The right panel shows the measurement section between 21 and 27 km, which is characterized by turbulent layers with much higher energy dissipation rates than in the altitude regions below. In addition, there exist much larger regions without turbulence. For instance, between 21.7 km and 23.2 km not one single turbulent layer has been observed and between 23.4 and 24.4 km only one layer has been detected with a much lower ε value than the other dissipation rates in this section. The turbulent layer with the highest energy dissipation rate is located just below 26 km. Summing up, one can see an increase of ε with altitude. Furthermore, the distance between the individual layers also increases with altitude.

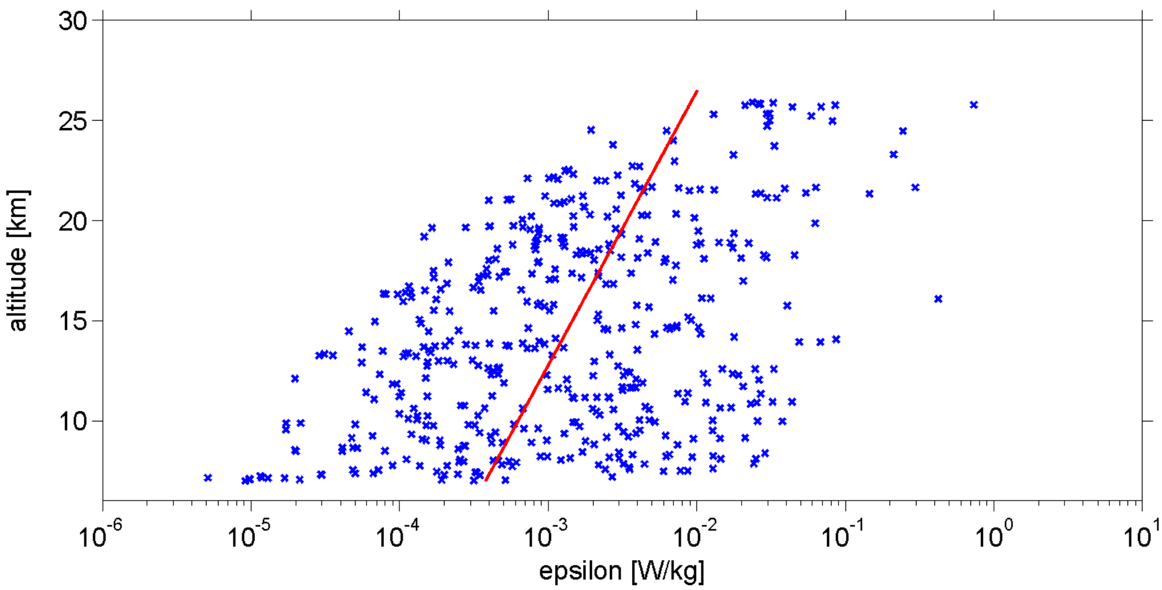

Figure 4.18.: Energy dissipation rate (blue) of the wind fluctuations during BEXUS 8 together with the linear regression (red line). Only turbulent regions detected by both CTA sensors were used to obtain ε.

Also for the temperature fluctuations during the BEXUS 8 flight a profile of the energy dissipation based on the spectral analyses has been determined. Figure 4.20 shows ε as a function of altitude. Strikingly, the values do not show such an increase with altitude like the values for the wind fluctuations of BEXUS 6 and BEXUS 8. Hence, the corresponding linear regression of $\log \varepsilon$ (black line) reveals only a small increase with altitude. Just like before,

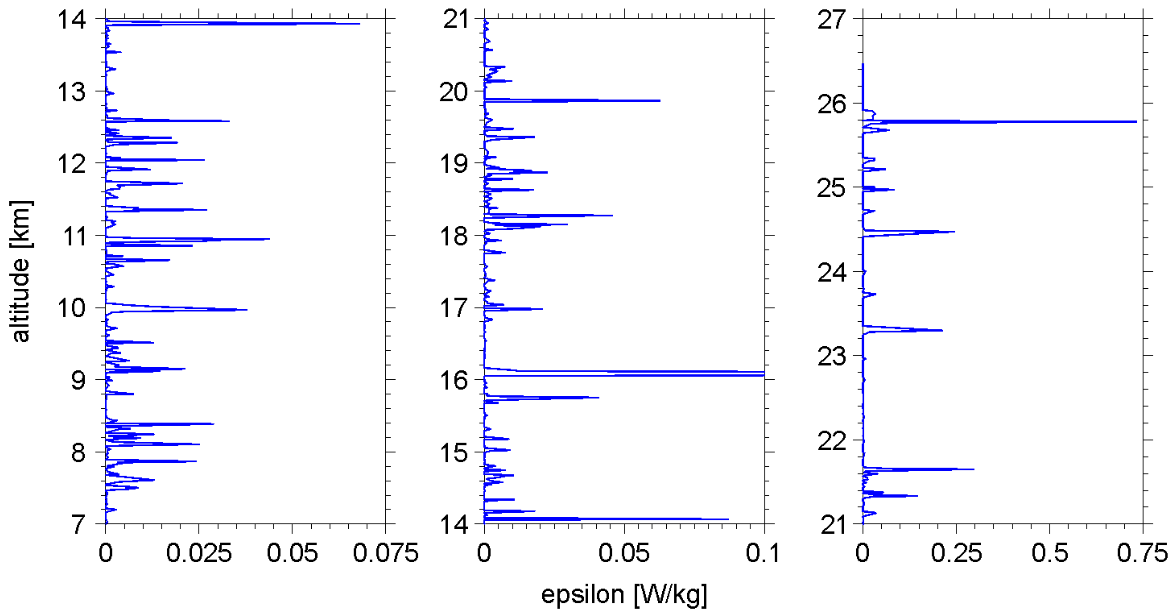

Figure 4.19.: Profile of energy dissipation rate of BEXUS 8 in a linear scale showing turbulent layers with increased ε values.

the ε-profile has been divided in three different altitude regions in order to visualize the individual turbulent layers. The left panel of Fig. 4.21 contains the altitude region between 7 and 14 km. There are only a few turbulent layers with a clear distance in between. However, at 11.8 km the energy dissipation rates increase suddenly significantly by a factor of ~10. Up to an altitude of 12.8 km several turbulent layers with such higher energy dissipation rates occur. This region is in turn followed by a more or less non-turbulent section, which lasts up to 14.2 km. The altitude region between 14 and 22 km is presented in the middle panel. In comparison with the altitude region in the left panel, the profile now possesses considerably more turbulent layers and a continuous alternation between turbulent and calmer regions characterizes this height range. But, in contrast to the wind fluctuations (see Fig. 4.17 and Fig. 4.19), it is not possible to identify an increase of ε values with altitude, though the values vary strongly. In addition, no increasing or decreasing of the distances between the individual turbulent layers can be observed. Similar results have been obtained for the altitude region 22 to 27 km (right panel). Only slightly different characteristics of the turbulent region are found. For instance, between 22 and 23 km the energy dissipation rate is much weaker compared to the region 21–22 km. Between 22.4 and 22.7 km no turbulence has been detected at all. Similar to the observations within the wind field, a turbulent layer with a higher vertical extent has been observed between 25.6 and 26 km. The observed layer within the wind fluctuations has almost the same vertical depth.

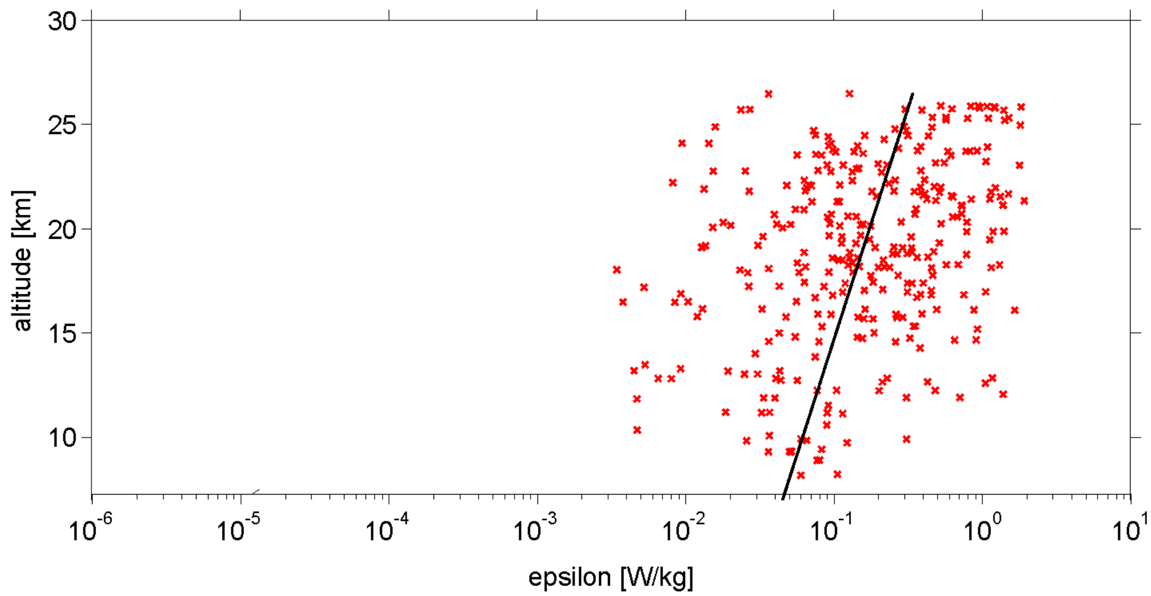

Figure 4.20.: The energy dissipation rate (red) of the temperature fluctuations measured during BEXUS 8. The linear regression is shown by the black line.

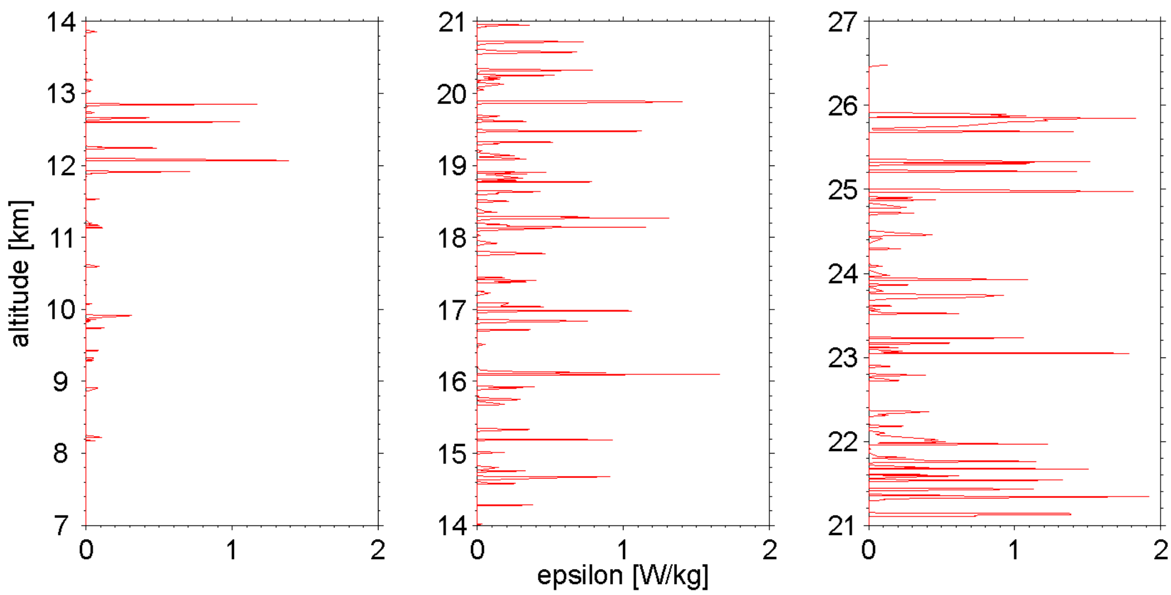

Figure 4.21.: Turbulent layers identified within the temperature field of BEXUS 8 shown by a linear plot of the energy dissipation rate for three altitude segments.

4.4.3. Summary and discussion of the energy dissipation rate

Based on the energy dissipation rate profiles shown above, mean ε values and the corresponding heating rate have been determined. In order to emphasize the large amount of energy which is dissipated into heat within the turbulent layers, the mean values have been determined for the turbulent regions only. Additionally for comparison, mean values have also been calculated for the complete altitude profile including turbulent and non-turbulent regions. Table 4.5 contains the mean values for both BEXUS flights divided into tropospheric and stratospheric region. Clear differences appear between $\varepsilon_{\mathrm{mean}}$ for the turbulent layers and $\varepsilon_{\mathrm{mean}}$ when also the non-turbulent region are taken into account. For almost all altitude regions, the energy dissipation rate is up to one order of magnitude higher within the turbulent layers compared to the sum of turbulent and non-turbulent regions. The higher ε values within turbulent layers point out, that if turbulence occurs in the stratosphere it has indeed the potential to influence e.g. the mixing of trace species.
Similar to the altitude plots of the energy dissipation rate shown in Sect. 4.4.1 and 4.4.2, all values of ε are higher in the stratosphere than in the troposphere. Especially the results for the velocity fluctuations reveal larger differences between both altitude regions. The difference between troposphere and stratosphere occurs regardless of whether only the turbulent regions or the complete altitude regions are considered. The increase of ε is partly caused by the fact that kinematic viscosity increases with altitude. In Sect. 2.2 it is shown that the relation between the energy dissipation rate and the inner scale depends on the kinematic viscosity. An increase of ν therefore influences the energy dissipation rate.
Strikingly, the ε values for temperature fluctuations are always higher than ε for velocity fluctuations. This result is rather unexpected, since it was assumed that the energy dissipation rate within the temperature field should be similar to the wind field. However, so far it is not clear why this difference between temperature and wind appears. Although an error in the determination of ε of 30–50 % has been estimated (see Sect. 4.3.1, this can not explain the fact, that the mean ε values for the temperature profile are almost one to two orders of magnitude higher than the mean values for the velocity profiles. Furthermore it should be noted that also during a further BEXUS flight in in 2011, a difference between the mean energy dissipation rates for temperature and wind has been observed (private communication A. Schneider, IAP). During this flight another temperature sensor has been used and therefore technical reasons causing the difference are excluded. However, further experiments and analyses are needed to confirm the difference between the dissipation rates of temperature and wind.

In order to compare the energy dissipation rates of LITOS with literature values, Tab. 4.6 contains ε values for the troposphere and stratosphere found in the literature. The values range from 1×10^{-6} up to 1.7×10^{-1} W/kg. The lowest values and at the same time the highest variation of ε have been measured by *Clayson and Kantha* [2008] during radiosonde campaigns. Airplane measurements performed in the 1960s result in energy dissipation rates around 10×10^{-2} W/kg, which are the highest values in this list. Pioneering balloon soundings have been carried out by *Barat* [1982a] and *Barat and Bertin* [1984b]. They determined a dissipation rate between 1×10^{-5} and 5×10^{-5} W/kg within the stratosphere. The ε values

Table 4.5.: Overview of the obtained mean energy dissipation rates of the BEXUS 6 and BEXUS 8 flight for the turbulent layers only and for the specific altitude regions including turbulent and non-turbulent regions. The values have been determined for the tropospheric and the stratospheric region as well as for the complete energy dissipation profile.

			only turbulent layers		turbulent and non-turbulent regions	
			[W/kg]	[K/d]	[W/kg]	[K/d]
wind	BEXUS 6	7 - 15 km	1.3×10^{-3}	0.1	9.9×10^{-4}	0.1
		15 - 29 km	3.8×10^{-2}	3.3	2.9×10^{-2}	2.5
		7 - 29 km	3.4×10^{-2}	2.9	1.8×10^{-2}	1.6
	BEXUS 8	7 - 15 km	4.6×10^{-3}	0.4	2.7×10^{-3}	0.3
		15 - 26.5 km	1.9×10^{-2}	1.6	6.9×10^{-3}	0.6
		7 - 26.5 km	1.1×10^{-2}	1.0	5.0×10^{-3}	0.4
temp	BEXUS 8	7 - 15 km	1.8×10^{-1}	15.6	1.6×10^{-2}	1.4
		15 - 26.5 km	3.7×10^{-1}	32.0	7.5×10^{-2}	6.5
		7 - 26.5 km	3.4×10^{-1}	29.4	5.3×10^{-2}	4.6

obtained with LITOS in the stratosphere are higher compared to the values of *Barat* [1982a] and *Barat and Bertin* [1984b]. This can be related to the fact, that due to technical progress a much higher measurement resolution is achieved with LITOS compared to earlier balloon soundings. On the other hand, especially the radiosonde results of *Clayson and Kantha* [2008] show strongly varying energy dissipation rates. Overall, the energy dissipation rates of LITOS agree nicely with the rates specified in the literature.

Table 4.6.: List of measured energy dissipation rates in the troposphere and stratosphere found in the literature.

author	year of measurement	measurement location	measurement method	altitude region	energy dissipation rate [W/kg]
[*Lilly et al.*, 1974]	1964 – 1968	HICAT (all over the globe)	airplane	14 – 21 km	$6.6\times10^{-2}-1.7\times10^{-1}$
[*Barat*, 1982a]	1978	CNES at Aire-sur adour & Gap Tallard, France	balloons	$\sim$ 25 – 28 km	$1.4\times10^{-5}-3.9\times10^{-5}$
[*Sato and Woodman*, 1982]	1978 – 1981	Arecibo, Puerto Rico	radar	5–30 km	2×10^{-4}
[*Barat and Bertin*, 1984b]	1978	CNES at Aire-sur adour & Gap Tallard, France	balloons	$\sim$ 25 – 28 km	$1\times10^{-5}-5\times10^{-5}$
[*Alexander and Tsuda*, 2008]	1995	Shigaraki, Japan	MU radar	UTLS region	UT: $\sim 0.5\times10^{-3}$ LS: $\sim 0.7\times10^{-3}$
[*Clayson and Kantha*, 2008]	1997	FASTEX, North Atlantic	radiosondes	$\leq$ 30 km	$10^{-6}-10^{-2}$
[*Clayson and Kantha*, 2008]	2005	Tallahassee, Florida & Denver, Colorado	radiosondes	$\leq$ 30 km	$10^{-6}-10^{-2}$
[*Kantha and Hocking*, 2011]	2007	Ontario, Canada	radar & radiosondes	radar: $\leq$ 11 km, radiosonde: $\leq$ 34 km	$10^{-4}-10^{-2}$
[*Zhang et al.*, 2012]	1998 – 2008	Miramar Nas, California	radiosondes	2 – 30 km	2 – 10 km: 2×10^{-4} 12 – 18 km: $>6\times10^{-4}$ > 20 km: $<4\times10^{-4}$
this work	2008 &2009	Kiruna, Sweden	balloons	0 – 30 km	7 – 15 km: $9.9\times10^{-4}-1.6\times10^{-2}$ 15 – $\sim$28 km: $6.9\times10^{-3}-7.5\times10^{-2}$

Chapter 5

Relation to the atmospheric background field

Within this chapter, the turbulence observations of LITOS are related to the background conditions of the atmosphere during BEXUS 6 and BEXUS 8. The general atmospheric conditions during both flights are briefly described with the help of the radiosonde data in the Sect. 5.1. In Sect. 5.2 the classical relation between the Richardson number as an indicator for the stability of the atmosphere and the occurrence of turbulence is discussed. An increasing number of observations and theoretical investigations cast doubts on the direct relation of Ri to turbulence. Hence, the measurements of LITOS provide an substantial contribution to this discussion. Finally possible sources of the observed turbulent layers are studied in Sect. 5.3.

5.1. Geophysical background conditions during flight

5.1.1. BEXUS 6

In order to study the atmospheric background conditions during flight, a radiosonde has been integrated into the BEXUS 6 gondola. The radiosonde measurements provide altitude profiles with a resolution of ~ 2 s, i.e. ~ 10 m. Figure 5.1 shows the profile for the temperature in the left panel and the meridional (black) and zonal (blue) wind components are plotted in the right panel. The horizontal black line marks the tropopause, which has been determined according to the WMO definition (temperature gradient decreases to $\leq 2\,^\circ$C/km). Starting around $0\,^\circ$C the temperature decreases down to a minimum of $\sim -64\,^\circ$C around 27 km. Obviously, the temperature decreases slightly further in the lower stratosphere, instead of increases above the tropopause altitude at ~ 10 km. Above the tropopause, one can regularly find short altitude ranges, where a positive temperature gradient is observed, e.g. at ~ 12 km and ~ 20 km. However, a slight tendency to small negative temperature gradients is prevailing and therefore more or less instable regions inducing turbulence can be expected. The right panel of Fig. 5.1 contains the profiles for the meridional and zonal wind component. Up to the tropopause, the meridional wind v decreases down to a minimum value of -26.6 m/s while the zonal wind component u increases up to 31 m/s. Therewith the jet stream is clearly visible at an altitude of ~ 10 km, i.e.at the tropopause. Above 10 km the zonal wind decreases slowly but remains positive, i.e. in eastward direction, up to maximum altitude of this profile and higher than 8 m/s. An increase of u arises again above 27 km. The profile of v shows an increase with altitude, but does not achieve values higher than -2 m/s. Since the meridional wind component is negative, a wind flow in southward directions dominates. No clear wave signature can be observed within the wind profiles, but further studies will follow in Sect. 5.3.1.

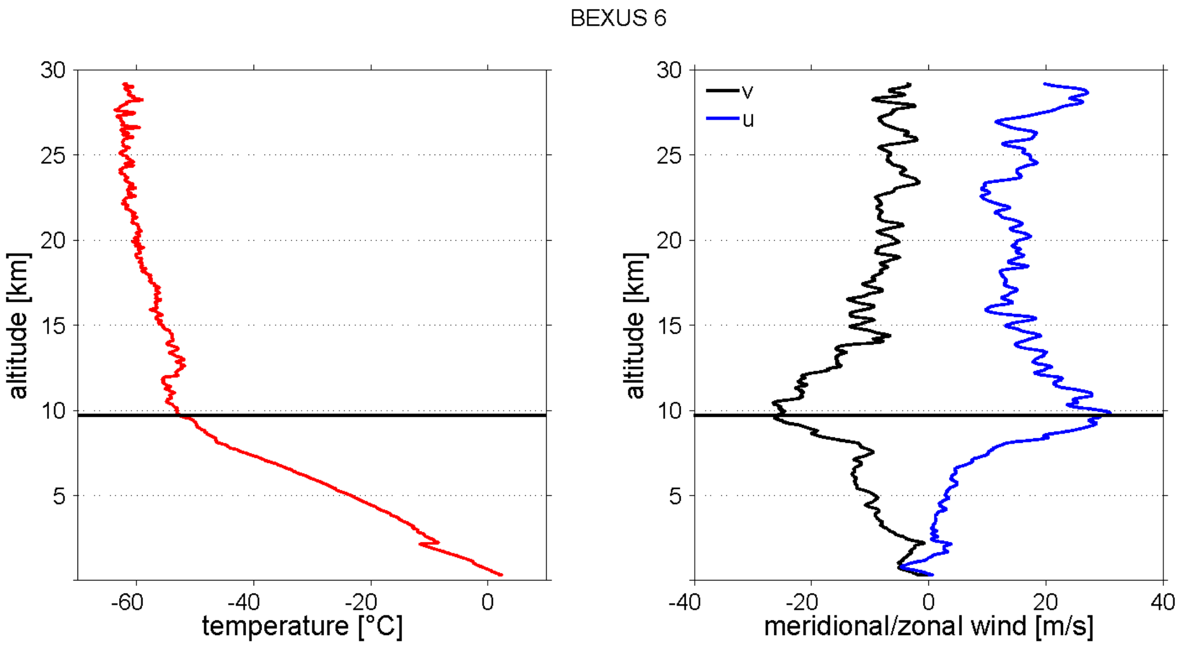

Figure 5.1.: Radiosonde data from the BEXUS 6 flight. The left panel shows the temperature profile and the right panel the meridional(black) and zonal (blue) wind velocity. The tropopause height is presented by the black line.

5.1.2. BEXUS 8

Similarly to BEUXS 6, a radiosonde has been part of the BEXUS 8 gondola to gain more information about the atmospheric background conditions. The results of that radiosonde are shown in Fig. 5.2. The left panel contains the temperature profile and the right panel the meridional and zonal wind component. The tropopause altitude is presented by the black line. Compared with the BEXUS 6 flight, the temperature profile shows a similar behavior with altitude. The temperature decreases within the troposphere, until it reaches a local minimum at an altitude of ~ 8 km, i.e. defining the tropopause. Above 8 km the temperature rises slowly more or less up to 15 km, before it starts to decrease again up to 20 km. From 20 km up to 27 km the profile is characterized by regions with increasing and regions with decreasing temperature values. Finally, above 27 km the temperature increases again. Due to the multiple changes in the temperature gradient with altitude, there exist several instable regions providing necessary conditions for turbulence.

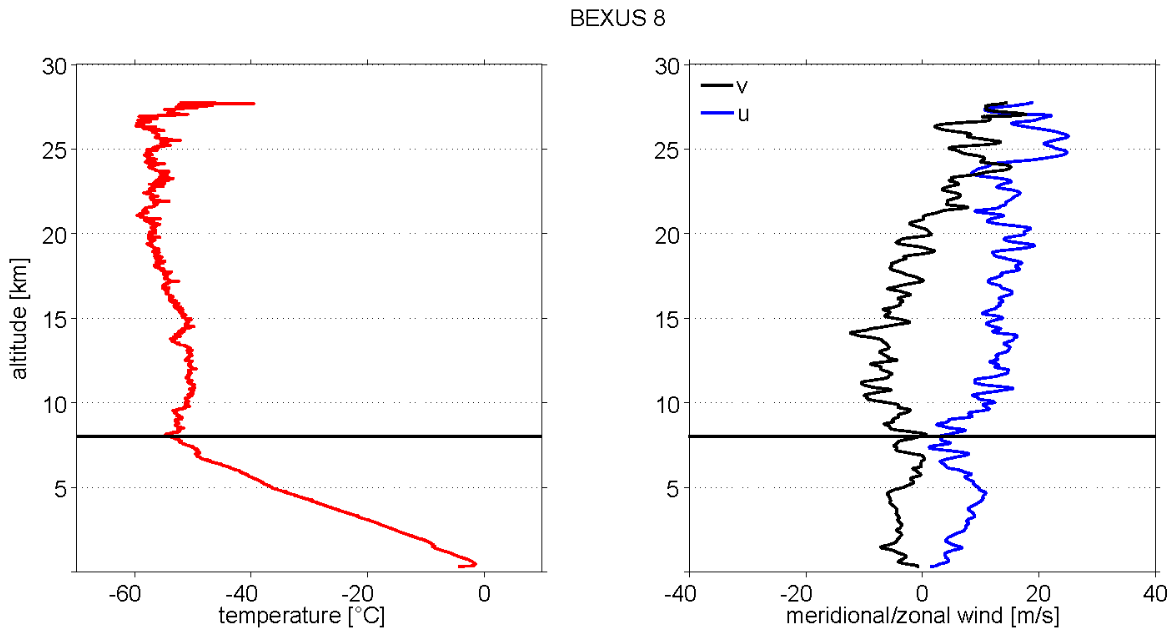

Figure 5.2.: Profiles of the radiosonde temperature during BEXUS 8 in the left panel. The right panel contains the meridional (black) and zonal (blue) wind velocity. The black line marks the tropopause height.

Figure 5.2 presents the profiles of the zonal (blue) and meridional (black) wind. Up to 20 km the values for the meridional wind component are negative, i.e. corresponding to a meridional wind flow in southward directions. Only a slight tendency towards positive values of v can be observed at tropopause height. Above 20 km the radiosonde reveals that the meridional wind component changes to northward directions. The zonal wind component remains positive, i.e. an eastward wind flow dominates in the entire profile. In the height of the tropopause u decreases slightly but stays positive and increases again up to 24 km. Above 24 km, u shows more variation and reaches a maximum value of 24.9 m/s around 25 km. The profiles of u and v do not show a clear indication for gravity waves. However, further examinations of gravity wave activity will follow in Sect. 5.3.1.

5.2. Relation to the Richardson number

A classical approach to analyze the relation of turbulence to the atmospheric background conditions, is the determination of the Richardson number Ri. As already explained in Sect. 2.1.1, Ri is the ratio of the Brunt-Väisälä frequency to the wind shear, i.e. the ratio of the buoyant consumption or production of turbulence to the kinetic production of turbulence. Hence, the Richardson number is used commonly as an indicator for the stability of the atmosphere. Additionally, the so called critical Richardson number Ri_c defines the threshold where the atmosphere changes from stability to turbulence, i.e. the laminar flow becomes turbulent. From linear theory Ri_c is suggested to be 1/4. However, an ongoing discussion questions the existence of such a critical Richardson number or rather the relation of the Richardson number to the occurrence of turbulence regions. An increasing number of observations and also theoretical simulations reveal a more complex and not straightforward relation of Ri_c to turbulent flows [*Achatz*, 2005, 2007; *Mauritzen and Svensson*, 2007; *Galperin et al.*, 2007; *Balsley et al.*, 2008]. The different analyses lead to three main assumptions:

1. suggestion of hysteresis: laminar air flow must drop below $Ri_c = 1/4$ to become turbulent, but turbulent flow can exist up to $Ri = 1.0$ before becoming laminar [*Galperin et al.*, 2007; *Balsley et al.*, 2008]

2. scale-dependent problem: the distribution of Ri depends strongly on scale size and Ri_c may exist if sufficiently small scales are examined [*Balsley et al.*, 2008]

3. Ri_c does not exist: extensive body of experimental, observational and theoretical results points to the fact that a single-valued Ri_c at which turbulence is suppressed totally and laminarized, simply does not exist and turbulence can survive in flows with Ri far exceeding unity [*Achatz*, 2005, 2007; *Galperin et al.*, 2007]

It is examined whether the turbulence results of LITOS show a correlation with the Richardson number or not. The radiosonde measurements are used to obtain Ri with the method proposed by *Balsley et al.* [2008]. That means, that the vertical gradient of the linear fits of the wind and potential temperature profiles are determined over a certain height increment, which is shifted in 5 m steps along the whole altitude profile. Afterwards Ri is calculated following Eq. 2.3. In order to investigate the scale dependence of the Richardson number, different height increments for the determination of the vertical gradients are used. The resulting Ri profiles are compared with the profiles of the energy dissipation rate ε measured with LITOS.

Figure 5.3 shows an altitude section of the energy dissipation rate profile (left panel) and the Richardson number Ri (right panel) of the BEXUS 6 flight. The critical Richardson number Ri_c is plotted as a red line, indicating the theoretical threshold under which Ri is supposed to fall in order to enable the development of turbulence. This condition is given around 12 km, where Ri is smaller than 1/4. Accordingly, a turbulent layer, i.e. an increase of the energy dissipation rate ε is observed around 12 km.

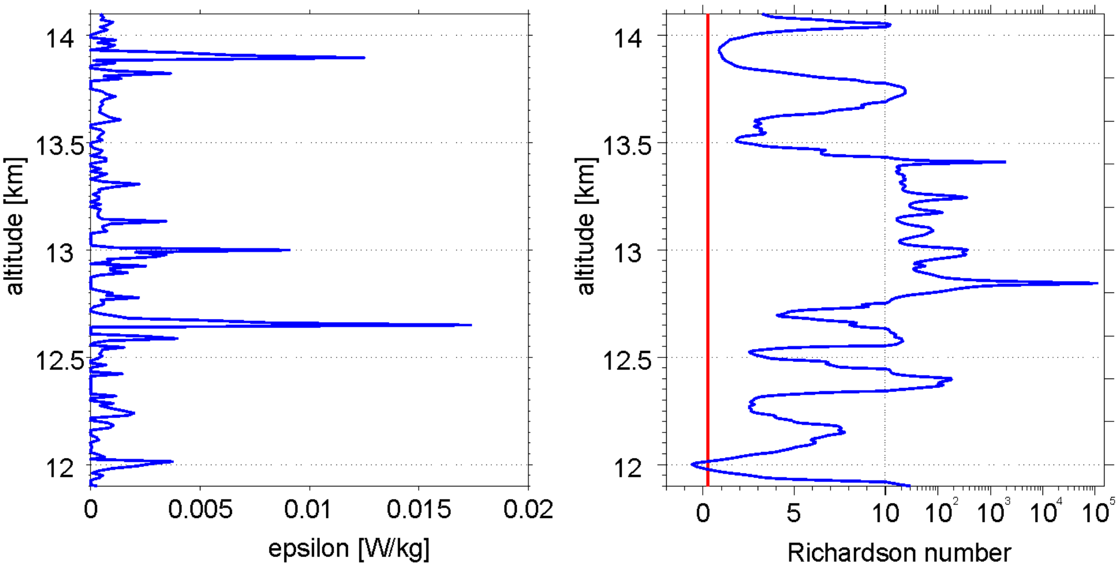

Figure 5.3.: Left panel: The obtained profile of the energy dissipation rate between 11.9 km and 14.1 km during the BEXUS 6 flight. Right panel: The Richardson number for the same altitude region. The red line marks $Ri_c = 1/4$. For a better presentation the x-axis scale is split into a linear part up to 10 and a logarithmic scale up 10^5.

However, this clear correlation expected from theory between Ri_c and ε is not observed again within the shown altitude section. Instead, even though Ri tends to 1/4 at 13.5 km no distinct turbulent layer can be identified, i.e. absolutely no increase of ε has been detected. On the other hand, turbulent layers have been observed, where Ri is far beyond any critical number. For instance, at 13 km a turbulent layer is well identified, while the values for Ri exceed 100. Similarly, the distinctive turbulent layer shortly above 12.6 km occurs in a region where Ri is between 5 and 10, i.e. larger than Ri_c. The altitude section from 11.9 km to 14.1 km illustrates well the observations with LITOS during both BEXUS flights.
By looking at the profiles of ε and Ri no clear relation has been obtained. The first assumption mentioned above suggests that Ri must drop below 1/4 before turbulence can occur and that turbulence can exist until Ri becomes 1. The profiles of the energy dissipation rate and the Richardson number of the BEXUS 6 flight shown in Fig. 5.3 clearly do not confirm this suggestion. Turbulent layers have been observed at Ri far beyond 1. In fact, only one turbulent layer (12 km) can be associated with a Richardson number smaller than 1/4 and one turbulent layer while Ri is smaller than 1 (13.9 km). In contrast, at 13 km a turbulent layer has been detected while the Richardson number reaches a value of nearly 200.
The second assumption implies a scale-dependent problem, i.e. the relation between Ri and ε depends on the scale at which both profiles have been obtained. That means that, in order to resolve turbulent layers with vertical depths of only some 10 meters, Ri has to be determined at approximately the same scale. That means, that the lower limit of the Ri scale is

given by the thickness of the turbulent layers. If Ri is calculated over even smaller scales, there would be no more difference between turbulence and the scales where turbulence is produced. Based on the radiosonde observations which provide data at ~ 10 m steps, Ri has been calculated for different altitude increments. In Fig. 5.4 an example of a turbulent layer with a thickness of 62 m observed during the BEXUS 6 flight is plotted. The Richardson number has been calculated over 10 m, 70 m, and 200 m, and the profiles are shown in panel b), c), and d), respectively. The red line marks the critical Richardson number Ri_c. Obviously, if Ri is calculated over 10 m or 70 m, the occurrence of the turbulent layer corresponds to a region where Ri is smaller than Ri_c. Whereas, if the Richardson number has been determined with a scale of 200 m, its values do not drop below 1/4 but rather remain larger than 6. Even though Ri tends to small values between 24.25 km and 24.42 km, this region would have been declared as non-turbulent which is contradictory to the observed turbulent layer within the wind field.

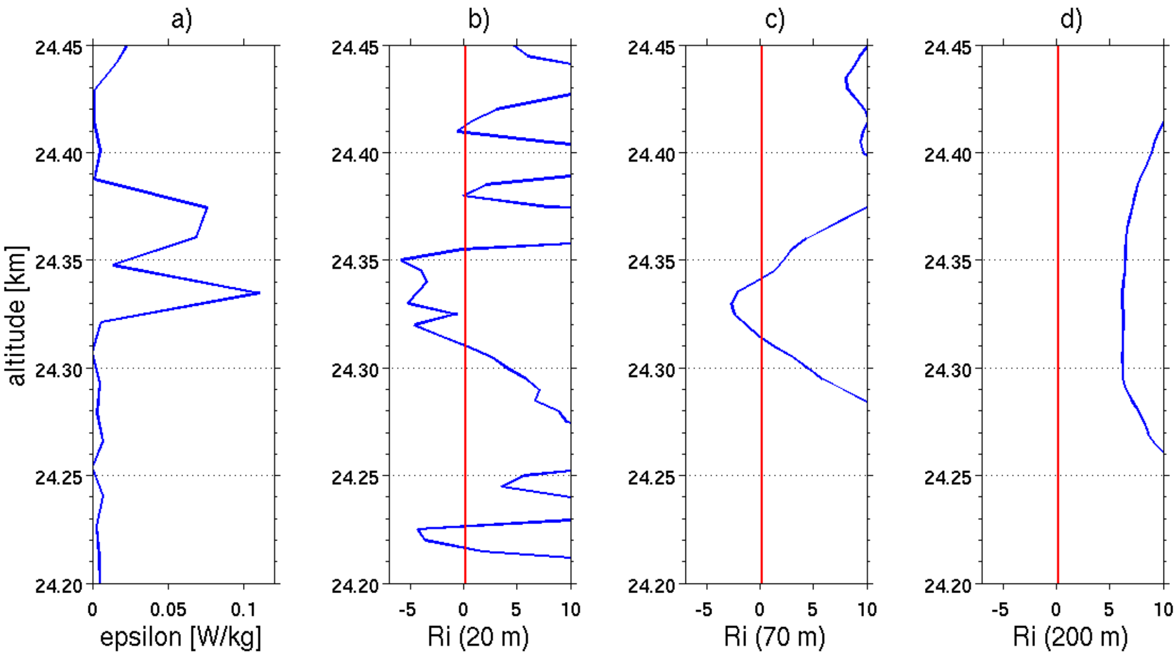

Figure 5.4.: Example of a 62 m thick turbulent layer observed during BEXUS 6 and the corresponding scale dependent Richardson number Ri. The ε profile (a) has been determined with a moving average over 25 m. In order to investigate the scale dependence of Ri, the profiles have been calculated over 20 m (b), 70 m (c), and 200 m (d). The red line presents the critical Richardson number $Ri_c = 1/4$.

However, the relation between Ri and ε seems to depend on the scale over which Ri has been calculated. For further investigations, Ri has been plotted as a function of the obtained energy dissipation rates of BEXUS 6 and BEXUS 8. Figure 5.5 shows the Richardson number of the BEXUS 6 flight determined for 10 m (top panel), 70 m (middle panel), and 200 m (bottom panel) against the ε values. It should be noted, that only energy dissipation rates

above zero have been used for this analysis. Surprisingly, even for rather small scales like 10 m or 70 m, the majority of Ri values are larger than 1. That means that turbulence has been observed although Ri indicates stability. For 10 m and 70 m only a few cases arise, where the theoretical criterium for instability (i.e. $Ri < 1/4$ or <1) is fulfilled and turbulence has actually been observed. For a scale of 200 m Ri is in fact always higher than 1.
A similar result has been obtained for the BEXUS 8 flight. Figure 5.6 shows the result for the wind fluctuations and Fig. 5.7 for the temperature fluctuations. Again, a strikingly low number of turbulent events occur at Ri smaller than 1 for a scale of 10 m and 70 m. For a Richardson number calculated over 200 m even none of the turbulent layers have been observed below Ri_c neither for wind fluctuations nor for temperature fluctuations. Instead the Richardson number is highly variable. Values of up to $\sim 10^5$ have been obtained during both BEXUS flights. Obviously, the Richardson number can not be directly related to the occurrence of turbulence. Even though high values of Ri have been measured, turbulence has been detected within the wind and temperature field. Additionally, the comparison of the ε profiles also reveals regions where Ri is smaller than Ri_c but no increase of the energy dissipation rate, i.e. no turbulent layer has been found. That means, regardless of the scale over which the Richardson number has been calculated, it can not be used as a reliable indicator for turbulence. Consequently, the common assumption to use Ri as an indicator for turbulence must be questioned.

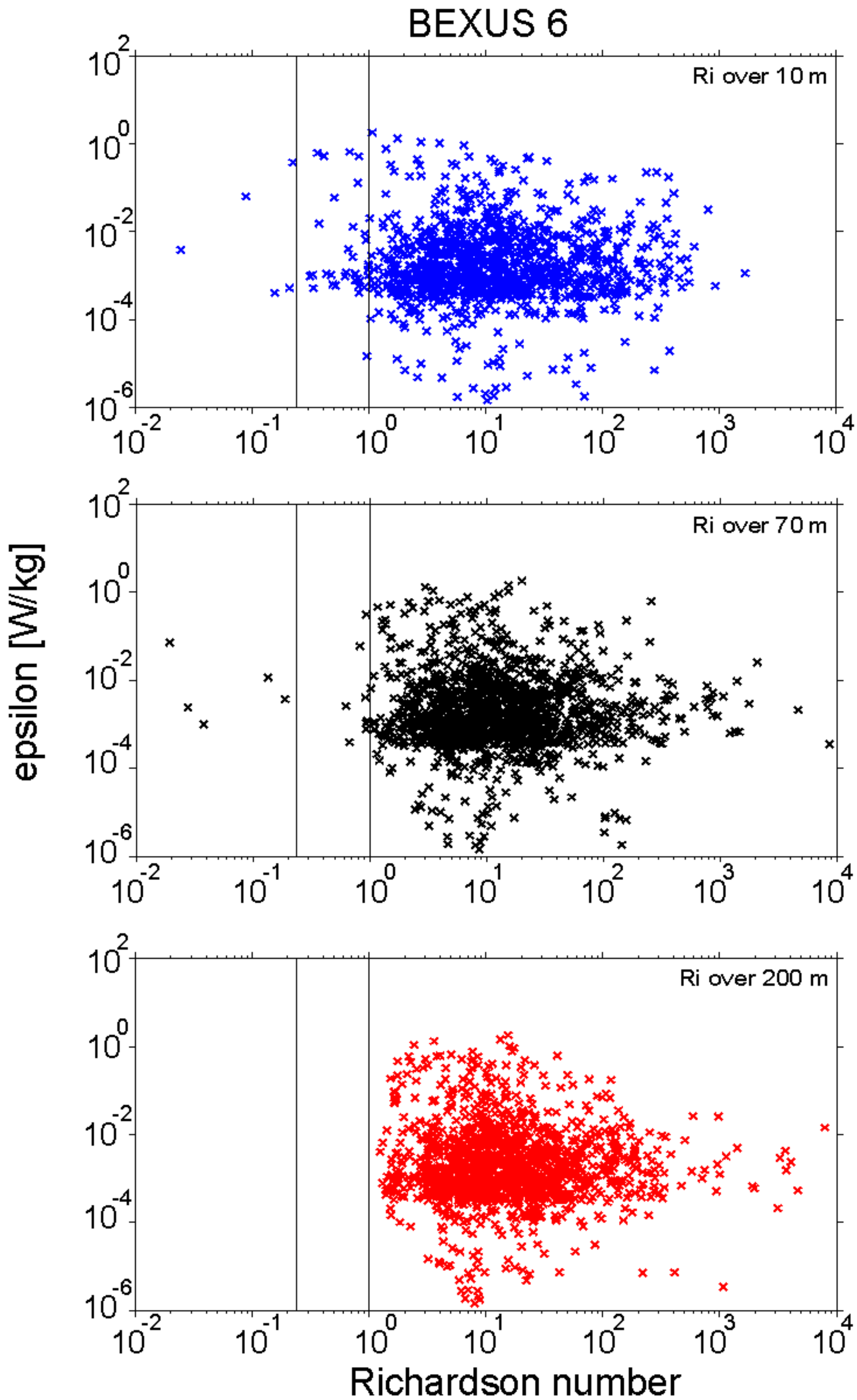

Figure 5.5.: Energy dissipation rates of the BEXUS 6 flight plotted against the Richardson number Ri which has been scaled over 10 m (top panel), 70 m (middle panel), and 200 m (bottom panel). The black lines present $Ri_c = 1/4$ and Ri=1 as the stability criterium. For more details see text.

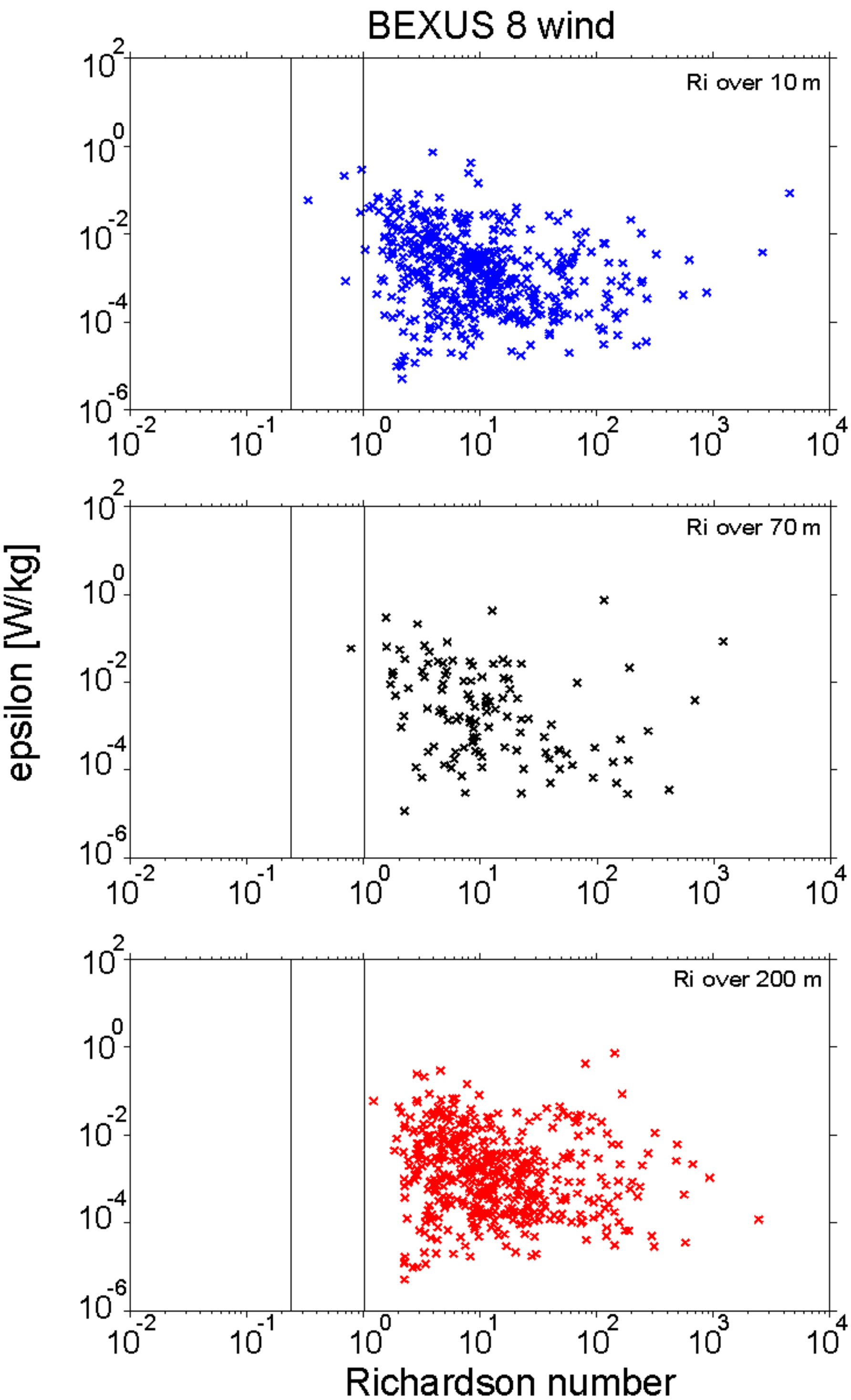

Figure 5.6.: The obtained energy dissipation rates for the wind fluctuations of BEXUS 8 have been plotted against Ri. The Richardson number has been calculated for 10 m (top panel), 70 m (middle panel), and 200 m (bottom panel). Ri=1/4 and Ri=1 are shown by the black lines.

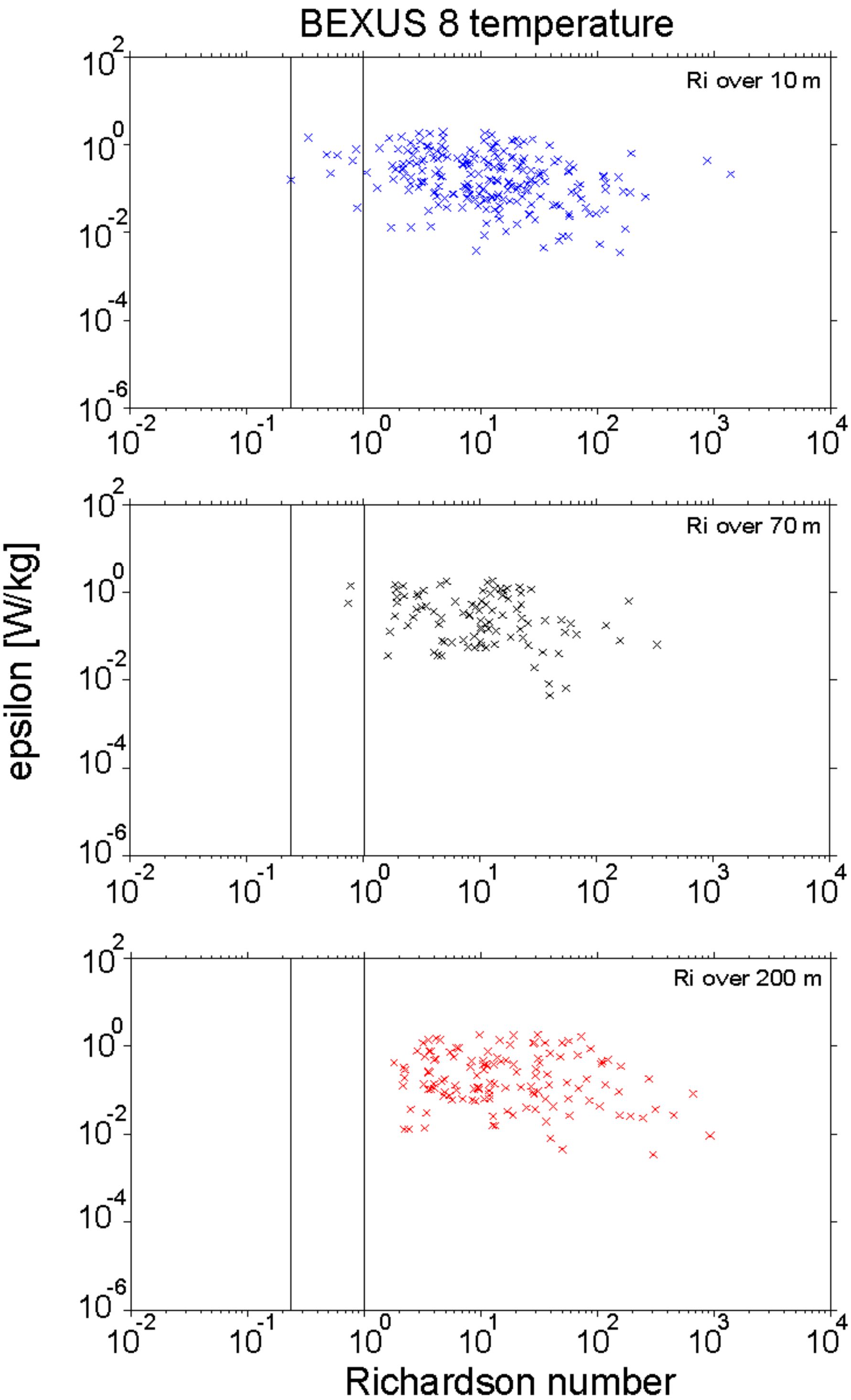

Figure 5.7.: Same as above, but for the temperature fluctuations of the BEXUS 8 flight.

5.3. Possible sources of turbulence observations

The two main turbulence sources in the stratosphere are Kelvin-Helmholtz instabilities (KHI) and the breaking of gravity waves, even though different sources can coexist and reinforce each other [*Sharman et al.*, 2012]. Due to the complexity of the dynamic processes of gravity waves and KHI, a theoretical description of the sources is not given here. Instead, the characteristics of turbulent layers caused by gravity wave breaking and KHI are shortly outlined and compared with the observations of LITOS.

5.3.1. Gravity wave breaking

The restoring force for gravity wave oscillations is the buoyancy force. Gravity waves are important for the transport of energy and momentum into the middle atmosphere and therefore strongly influence the atmospheric circulation, structure, and variability [e.g., *Fritts and Alexander*, 2003; *Holton*, 2004]. The main gravity wave sources are topography, convection, and wind shear. These waves then propagate from the troposphere into the middle atmosphere with a growing amplitude. Different factors can cause a breaking of the wave (already in the stratosphere) and therewith induce turbulence. A detailed overview of gravity wave characteristics, sources, and breaking processes is found in *Fritts and Alexander* [2003]. The theoretical simulations of *Fritts et al.* [2003] regarding the formation of turbulent layers due to gravity wave breaking shall be shortly outlined here. Following these simulations, turbulence and mixing occur within the unstable phase of the gravity wave. Because the gravity wave continuously propagates vertically, the induced turbulent layers are rather transient phenomena. Only at the beginning of the turbulent layer formation, strong thermal gradients can be observed at the edge regions of the layer, while at later times, the gradients disappear and a more uniform structure dominates. Furthermore, there is no specific point where maxima of thermal and kinetic energy dissipation are found during the wave propagation.
Due to the facts that the turbulent layers caused by gravity wave breaking are transient and dissipation maxima occur in different phases of the wave, it is rather difficult to relate directly the turbulence observations of LITOS to breaking gravity waves. The Scandinavian mountain ridge has a sufficient width to induce gravity waves and generally gravity waves can occur above Kiruna [*Dörnbrack et al.*, 2001]. Therefore, in order to examine whether breaking gravity waves might be a source for the turbulence observations or not, the profiles of the meridional and zonal wind components obtained by the radiosonde have been used for hodographic analyses. None of the hodographs, neither for BEXUS 6 nor for BEXUS 8, shows a elliptical rotation being indicative of a single monochromatic gravity wave (see App. F). Figure 5.8 shows the hodograph (top) and the meridional and zonal wind profile with their fluctuations (bottom) between 20 and 27 km of the BEXUS 8 flight. No distinct ellipse can be found in the hodograph and also no clear wave signature appears within the profiles of u' and v'. Instead, the figures indicate a variety of superimposing waves of generally small amplitude. It is not possible to identify a specific wave vanishing at a particular altitude and by this inducing turbulence. Consequently, the observed turbulence during both BEXUS

flights can not be clearly attributed to gravity wave breaking. Therefore, within the next section, it is studied whether Kelvin-Helmholtz instabilities are the source for the observed turbulent layers.

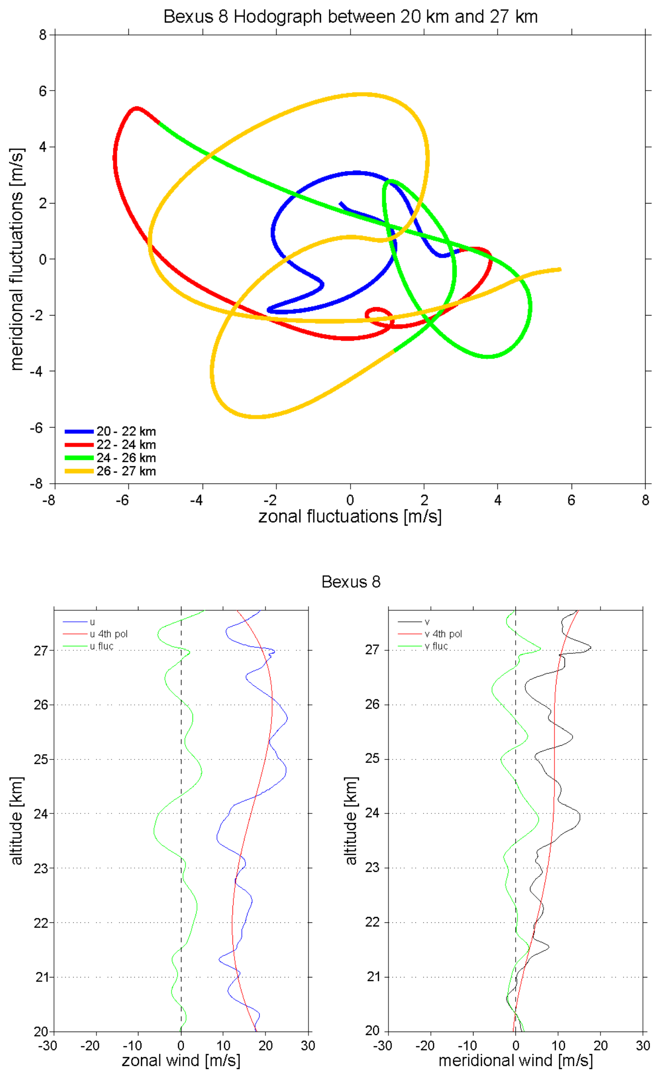

Figure 5.8.: Top: Hodograph of the altitude region between 20 km and 27 km of the BEXUS 8 flight. Bottom: Profiles of the wind component u (blue), left panel, and v (black), right panel, together with the 4th order polynomial (red) and the profiles of u' and v' (green).

5.3.2. Kelvin-Helmholtz instabilities

In the case of strong wind shear the statically stable layering in the stratosphere can become instable and Kelvin-Helmholtz instabilities (KHI) arise forming billow structures. Those wavelike oscillations grow in amplitude and consequently break, which leads to turbulence. Following the theoretical simulations performed by *Fritts et al.* [2003], stratospheric turbulence due to KHI is longer lasting compared to turbulence induced by gravity wave breaking. Furthermore, the formation of a turbulent layer caused by KHI occurs in different time steps. *Fritts et al.* [2003] obtained profiles of temperature, velocity, Richardson number, and the thermal and viscous dissipation during the development of a turbulent layer, which are illustrated in Fig. 5.9. In the beginning of the formation process, alternating gradients of temperature and velocity at the edge regions are visible. Also the profiles of the mechanical and thermal dissipation show initially a similar behavior at the boundary of the layer. But soon afterwards, the two dissipation fields separate themselves and vigorous turbulent mixing of the billow cores takes place. The thermal gradients are destroyed and thus the thermal dissipation inside the layer is reduced. At the end, the largest mechanical dissipation occurs in the center of the turbulent layer and the largest thermal energy dissipation in the strongly stratified edge regions. Due to the fact, that in-situ observations of stratospheric turbulence are rare, the simulations of *Fritts et al.* [2003] are confirmed by only a few experimental studies so far. For instance, *Barat and Bertin* [1984b] report C_T^2 maxima near the boundaries of turbulent layers and smaller values in the interior of the layers. Another example has been cited by *Fritts et al.* [2003]. The radiosonde measurements of *Coulman et al.* [1995] reveal a series of turbulent layers with sharp temperature gradients and C_T^2 maxima at the edges and C_T^2 minimum within the layer. Hence, the profiles of temperature, wind shear, Richardson number, and energy dissipation rate obtained with LITOS have been analyzed in order to find KHI structures.

During both BEXUS flights Kelvin-Helmholtz instabilities have been detected and their structure has been found in the measured profiles. Figure 5.10 shows an example of a KHI between ~ 25.28 km and ~ 26.08 km for the BEXUS 6 flight. The left panel contains the energy dissipation rate of the wind field and the middle panel the temperature profile and the wind shear profile. The right panel shows the Richardson number calculated over 25 m and over 200 m. Within the last section, the reliability of *Ri* as an indicator for turbulence has been questioned. However, it has been shown, that in some cases the relation between *Ri* and the occurrence of turbulence depends on the scale over which *Ri* has been determined. Accordingly, the profile of *Ri* will be shown here for different scales in order to enable a comparison with the simulations of *Fritts et al.* [2003].

The Kelvin-Helmholtz instability is clearly recognizable by the expected structure within the temperature profile between 25.28 km and 26.08 km. The beginning and ending of the KHI is characterized by increased fluctuations, while inside the layer the temperature is isothermal. This observed behavior agrees nicely with the simulations of *Fritts et al.* [2003] shown in Fig. 5.9. Obviously, the measurements of LITOS show an early state during the development of a turbulent layer. As described by *Fritts et al.* [2003], especially at the beginning of the formation an alternating temperature gradient can be observed at the edge regions.

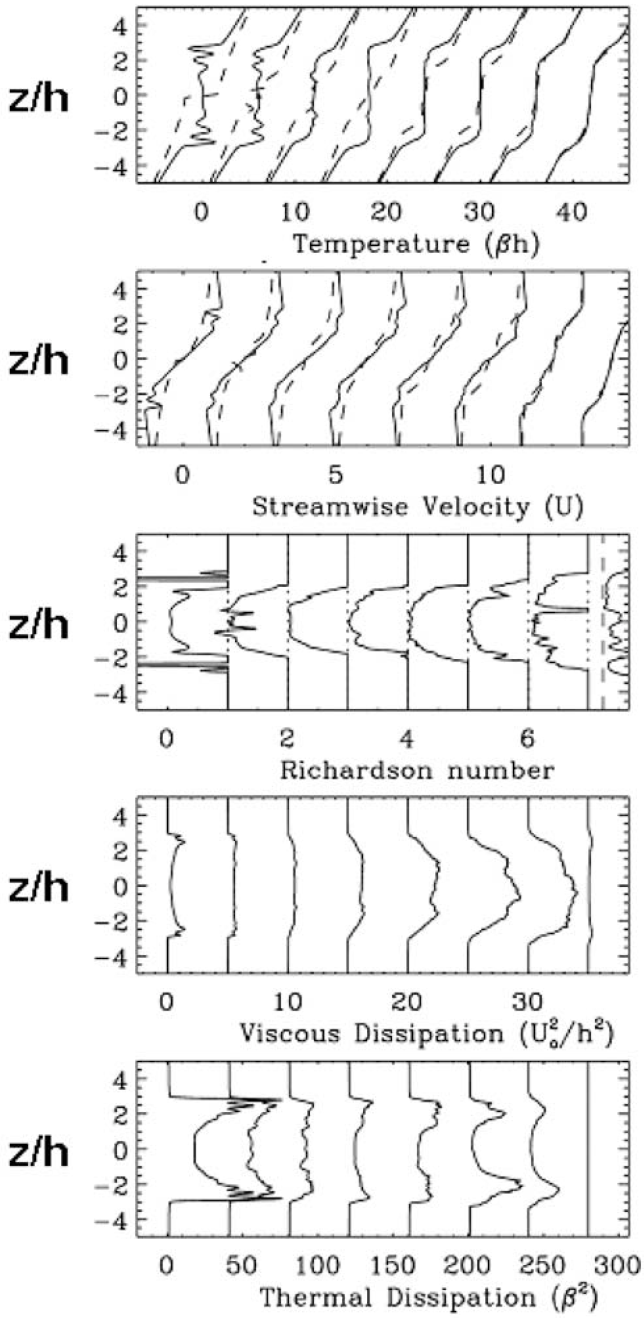

Figure 5.9.: Profiles of temperature, velocity, *Ri*, thermal dissipation, and viscous dissipation during a Kelvin-Helmholtz billow at the different time steps of turbulent layer development[from *Fritts et al.*, 2003]. The solid lines represent the billow center of a KHI and the dashed lines the braid between adjacent billows. The profiles have been obtained with idealized high-resolution simulations.

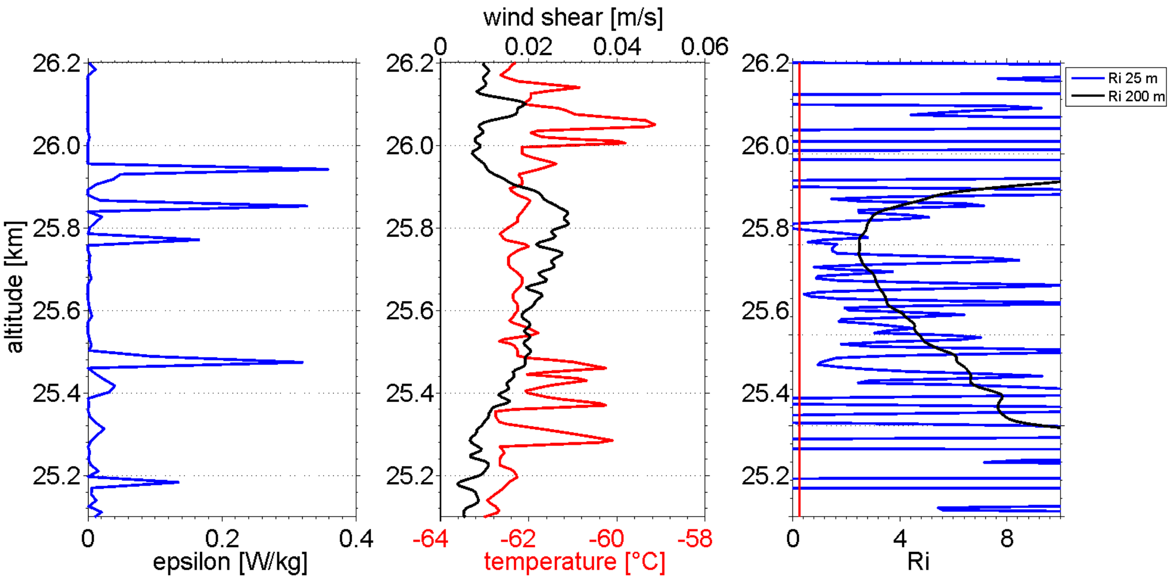

Figure 5.10.: Example of a Kelvin-Helmholtz instability between 25.28 km and 26.08 km observed during BEXUS 6. The profiles of temperature (red) and wind shear (black) in the middle panel show the expected structures of a Kelvin-Helmholtz billow. The energy dissipation rate (left panel) increases inside the layer, while Ri (right panel) tends to smaller values. The red line marks Ri_c.

Also the measured dissipation profile shows increased values at the boundaries and smaller values inside the layer, similar to the simulated profile in Fig. 5.9. Looking at the Richardson number calculated over 20 m, it drops actually below the critical value inside the billow at 25.8 km but also outside the layer. If the profile of Ri is scaled over 200 m, it shows a local minimum related to the billow core which corresponds to the theoretical results.

Also during the BEXUS 8 flight, KHI have been observed. But compared to BEXUS 6 they have been measured less frequent. Figure 5.11 presents the profiles of the energy dissipation rates, temperature, wind shear, and Richardson number for a KHI between 12 km and 12.5 km. Again, the structure of the temperature profile, i.e.,the fluctuations at the edge regions, agree nicely with the simulated profile of *Fritts et al.* [2003] (see Fig. 5.9). The energy dissipation rate profiles display a structure indicating an advanced development of the KHI. Both profiles show increased values not only at the edge region of the layer but also inside the layer. The simulations of *Fritts et al.* [2003] reveal an increase of the viscous dissipation also inside the billow core at a later state (e.g. fourth profile in Fig. 5.9) in combination with a decrease of the thermal dissipation at the edges. Similar observations were made in the shown example of BEXUS 8. Additionally, instead of one distinct minimum inside the core of the KHI, the Richardson number profile shows several regions with smaller values. Whereas more regions with values tending to $Ri_c = 1/4$ are determined if Ri is calculated over 25 m compared to a scale of 200 m. However, following the simulations of *Fritts et al.* [2003], the varying Ri profile points to a later state of the turbulent layer formation. Furthermore, also the less pronounced temperature gradients at the boundaries of the KHI layer characterize an advanced development compared to the KHI observed during BEXUS 6 (see Fig. 5.10). Summarizing, Kelvin-Helmholtz instabilities have been clearly identified as a source for some of the turbulent layers which have been detected during BEXUS 6 and BEXUS 8.

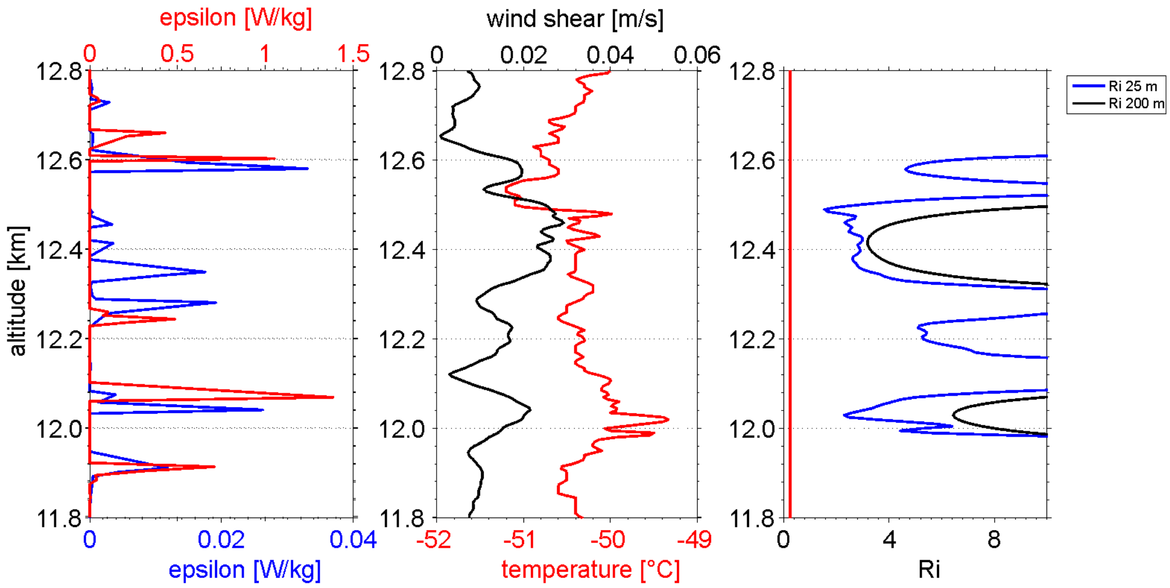

Figure 5.11.: Kelvin-Helmholtz instability observed during BEXUS 8 between 12 km and 12.5 km, clearly recognizable at the temperature profile (red) in the middle panel. The energy dissipation rates of the temperature fluctuations (red) and velocity fluctuations (blue) in the left panel exhibit increased values at the edges of the billow as well as inside the layer. Also the Richardson number in the right panel shows smaller values related to the billow, but stays larger than Ri_c (red line).

Chapter 6

Summary and outlook

Within this study turbulence observations in the stratospheric wind and temperature field with unprecedented temporal and spatial resolution are obtained with a special designed balloon-borne instrument called LITOS. Based on the observation analyses new insights in stratospheric turbulence have been gained. The following sections summarize the main results of the study.

Instrument development

LITOS is a new light-weight, compact balloon-borne instrument which has been developed to investigate small-scale turbulent fluctuations in the temperature and wind field of the stratosphere. Due to the very high spatial measurement resolution of typically 2.5 mm, the entire turbulence spectrum down to the viscous subrange in the stratosphere is studied for the first time. The instrument has been successfully launched several times from the institute site in Kühlungsborn as a stand-alone payload. Additionally, LITOS has been flown two times as part of the BEXUS campaigns in 2008 and 2009 from Kiruna (67 °N, 21 °E).
The applied CTA and CCA techniques have never been used before on balloon platforms. Therefore, their properties are completely unknown for stratospheric conditions and extensive laboratory measurements within a climate and a vacuum chamber have been performed. The results of these measurements reveal that the CTA and the CCA systems are well suitable for balloon soundings.

Turbulence observations

During both BEXUS flights turbulence has been detected with LITOS. The observations show an alternation between turbulent and non-turbulent regions and a quite abrupt and distinct transition between both regions. This intermittent structure has also been detected by earlier observations, but with the high sampling rate of LITOS it is now possible to observe even the variability within turbulent layers themselves.
One major point of interest is the number and vertical thickness of the observed turbulent layers. The obtained data set is quite heterogeneous and comprehensive, therefore an autonomous and effective method is needed to analyze the given data profiles and to determine the characteristics of the turbulent layers. Basically, turbulent layers are characterized by a high variability of the measured wind or temperature values within a certain altitude

distance. Hence, an algorithm has been developed which detects such concentrations or clusters of turbulent values within the wind or temperature profile. The results of the cluster algorithm reveal that during both BEXUS flights more turbulent layers in the wind and temperature field have been observed within the stratosphere (above 15 km) compared to the tropospheric region (7-15 km). The turbulent layers within the stratospheric wind field of BEXUS 6 and BEXUS 8 are thinner on average and also the distances between the layers are smaller than below 15 km. For the complete profile of wind fluctuations the mean turbulent layer thickness of the BEXUS 8 flight amounts to 46.4 m and is therewith just $\sim$8 m larger than the mean thickness of the BEXUS 6 flight (38.2 m). In contrast to the wind, the mean thickness of turbulent layers within the temperature field in the troposphere is almost identical with the thickness in the stratosphere. The mean thickness for the entire temperature profile is 24.0 m.
It is important to note that due to the limited knowledge of stratospheric turbulence, the statistics obtained with the cluster algorithm contain completely new insights in e.g. the distribution and depths of turbulent layers as well as the difference between their occurrence in the wind and temperature field.

Geophysical results

Based on the high resolution data set, the energy dissipation rate ε, one of the most essential turbulence parameter, has been determined with high precision and detailed profiles of ε are obtained. For the calculation of the energy dissipation rate the method of *Lübken* [1992] and *Lübken et al.* [1993] formulated for density fluctuations has been adopted. The method includes the fitting of the theoretical Heisenberg model to the measured turbulent spectrum and from the best fit ε is obtained. Since velocity and temperature fluctuations are measured with LITOS, the method has been recalculated in order to adapt it to velocity and temperature fluctuations. The profiles of the energy dissipation rate for velocity fluctuations of the BEXUS 6 and BEXUS 8 flight show a significant increase of ε with altitude. In contrast, the ε profile for the temperature fluctuations of the BEXUS 8 flight shows more or less no increase with altitude. Additionally, the mean ε values for the temperature profile are almost one to two orders of magnitude higher than the mean values for the velocity profiles for unknown reasons. The values for ε obtained with LITOS show high variability. Nevertheless, these findings are in general agreement with the values found in the literature.
Another main aspect within this study is the relation of the observed turbulent layers to the atmospheric background conditions. A classical approach to analyze this relation is the determination of the Richardson number Ri as an indicator for the stability of the atmosphere. However, the direct relation of small Richardson numbers to the occurrence of turbulence is recently questioned. The analyses of the BEXUS 6 and BEXUS 8 flight reveal that it is in fact not straightforward to find a direct correlation between low values of Ri and ε. Turbulence has been detected in regions with high values of Ri as well as in regions with low values of Ri regardless of the scale over which the Richardson number has been calculated. Consequently, following the results of this study, Ri does not seem to be a reliable indicator for the occurrence of turbulence.

Finally, possible sources of the turbulent layers have been examined. The two main turbulent sources in the stratosphere are Kelvin-Helmholtz instabilities (KHI) and the breaking of gravity waves. The profiles of the meridional and zonal wind components obtained by the radiosonde have been used for hodographic analyses. None of the hodographs, neither for BEXUS 6 nor for BEXUS 8, show distinct gravity wave activity. Hence, the observed turbulence during both BEXUS flights can not be attributed to gravity wave breaking. On the other hand, during both BEXUS flights Kelvin-Helmholtz instabilities have been detected. The temperature and wind shear profiles agree nicely with the theoretical simulations of *Fritts et al.* [2003] and show different stages of the turbulent layer formation due to Kelvin-Helmholtz instabilities. Therefore, it is evident from the observations, that Kelvin-Helmholtz instabilities are the main source for some of the turbulent layer detected during BEXUS 6 and BEXUS 8.

Outlook

One of the future plans concerning the instrumental development of LITOS is to improve the attitude control of the small LITOS gondola during flight using e.g. a suitable combination of wind vanes. Therewith disturbances within the measured stratospheric turbulence spectra can significantly be reduced. This would enable more flexible possibilities to launch LITOS e.g. from different atmospheric research stations.
Besides the technical improvements, additional launches are planned during specific geophysical conditions and different seasons. This would enable e.g. analyses of the turbulent sources or the investigation of possible seasonal difference in the occurrence of turbulent layers. However, the existing data set still provide further interesting topics to be investigated. For instance, there have been a floating phase of the BEXUS 6 and BEXUS 8 balloon which have been excluded from this study. However, the data from floating phase can also be checked for turbulent layers. Furthermore, within oceanographic studies, the Thorpe displacement is usually determined based on potential temperature profiles in order to determine the energy dissipation rate. Here, a statistical approach has been used for the calculation of ε, however, it is worthwhile to compare both methods. It should be emphasized, that the unique combination of wind- and temperature measurements on sub-cm scale with LITOS offers an excellent possibility to examine the theoretical statements concerning the differences between thermal and kinetic energy and the formation of turbulent layers. Especially, the observed unexpected difference between thermal and kinetic energy dissipation motivates further experiments and analyses.

Appendix A

Determination of inner scale for temperature fluctuations

The 1-dimensional Heisenberg spectrum [*Lübken*, 1993, p. 43, Eq. 3.109] is given by:

$$W(\omega) = \frac{\Gamma(5/3)\sin(\pi/3)}{2\pi v_b} \cdot C_T^2 \cdot \frac{(\frac{\omega}{v_b})^{-\frac{5}{3}}}{\left\{1 + (\omega/v_b k_0)^{\frac{8}{3}}\right\}^2} \tag{A.1}$$

where C_T^2 is the structure function constant, ω is the frequency and v_b the balloon velocity. (A normalization factor f_α is mistakenly used in the original equation of *Lübken* [1993]. As it will be seen later, this factor will be applied in Eq. A.10 and thus must be omit in the equation of the Heisenberg spectrum.)
The breakpoint between the asymptotic form of $W(\omega)$ in the inertial and viscous subrange is defined as k_0. With $B := \Gamma(5/3)\sin(\pi/3) \cdot C_T^2$ Eq. A.1 forms to:

$$W(\omega) = \frac{B}{2\pi v_b} \cdot \frac{(\frac{\omega}{v_b})^{-\frac{5}{3}}}{\left\{1 + (\omega/v_b k_0)^{\frac{8}{3}}\right\}^2} \tag{A.2}$$

The 1-dimensional frequency spectrum $W(\omega)$ is related to the 3-dimensional spectrum $\Phi(k)$ by [*Lübken* [1993], p. 31, Eq. 3.53 and *Tatarskii* [1971], p. 35]:

$$\Phi(k) = -\frac{v_b^2}{2\pi k} \cdot \frac{d}{d\omega} W(\omega) \tag{A.3}$$

Inserting Eq. A.2 in Eq. A.3 gives:

$$\Phi(k) = -\frac{v_b^2}{2\pi k} \cdot \frac{B}{2\pi v_b} \cdot \frac{d}{d\omega} \left(\frac{(\frac{\omega}{v_b})^{-\frac{5}{3}}}{\left\{1 + (\omega/v_b k_0)^{\frac{8}{3}}\right\}^2} \right) \tag{A.4}$$

$$\Phi(k) = -\frac{B v_b}{4\pi^2 k} \cdot \frac{d}{d\omega} \left(\frac{(\frac{\omega}{v_b})^{-\frac{5}{3}}}{\left\{1 + (\omega/v_b k_0)^{\frac{8}{3}}\right\}^2} \right) \tag{A.5}$$

Calculation of the derivative:

$$\frac{d}{d\omega}\left(\frac{\frac{\omega}{v_b}^{-\frac{5}{3}}}{\left\{1+(\omega/v_bk_0)^{\frac{8}{3}}\right\}^2}\right) = \frac{\left(-\frac{5}{3}(\frac{\omega}{v_b})^{-\frac{8}{3}}\frac{1}{v_b}\right)\cdot\left(\left\{1+(\omega/v_bk_0)^{\frac{8}{3}}\right\}^2\right)-\left((\frac{\omega}{v_b})^{-\frac{5}{3}}\right)\cdot\left(2\left\{1+(\omega/v_bk_0)^{\frac{8}{3}}\right\}\frac{8}{3}(\omega/v_bk_0)^{\frac{5}{3}}\frac{1}{v_bk_0}\right)}{\left\{1+(\omega/v_bk_0)^{\frac{8}{3}}\right\}^4}$$

$$= \frac{\left(-\frac{5}{3}(\frac{\omega}{v_b})^{-\frac{8}{3}}\frac{1}{v_b}\right)\cdot\left(1+(\omega/v_bk_0)^{\frac{8}{3}}\right)-\left((\frac{\omega}{v_b})^{-\frac{5}{3}}\right)\cdot\left(2\cdot\frac{8}{3}(\omega/v_bk_0)^{\frac{5}{3}}\frac{1}{v_bk_0}\right)}{\left\{1+(\omega/v_bk_0)^{\frac{8}{3}}\right\}^3}$$

with $k = w/v_b$

$$= \frac{\frac{1}{v_b}\left[\left(-\frac{5}{3}k^{-\frac{8}{3}}\right)\cdot\left(1+(k/k_0)^{\frac{8}{3}}\right)-\left(k^{-\frac{5}{3}}\right)\cdot\left(2\cdot\frac{8}{3}(k/k_0)^{\frac{5}{3}}\frac{1}{k_0}\right)\right]}{\left\{1+(k/k_0)^{\frac{8}{3}}\right\}^3} = \frac{\frac{1}{v_b}\left[\left(-\frac{5}{3}k^{-\frac{8}{3}}-\frac{5}{3}k^{-\frac{8}{3}}\cdot(k/k_0)^{\frac{8}{3}}\right)-\left(\frac{16k^{-\frac{5}{3}}}{3k_0}(k/k_0)^{\frac{5}{3}}\right)\right]}{\left\{1+(k/k_0)^{\frac{8}{3}}\right\}^3}$$

$$= \frac{\frac{1}{v_b}\left[-\frac{5}{3}k^{-\frac{8}{3}}-\frac{5}{3}k_0^{-\frac{8}{3}}-\frac{16k_0^{-\frac{5}{3}}}{3k_0}\right]}{\left\{1+(k/k_0)^{\frac{8}{3}}\right\}^3} = \frac{\frac{1}{v_b}\left[-\frac{5}{3}k^{-\frac{8}{3}}-\frac{5}{3}k_0^{-\frac{8}{3}}-\frac{16}{3}k_0^{-\frac{8}{3}}\right]}{\left\{1+(k/k_0)^{\frac{8}{3}}\right\}^3} = \frac{\frac{1}{v_b}k^{-\frac{8}{3}}\left[-\frac{5}{3}-\frac{21}{3}(k/k_0)^{\frac{8}{3}}\right]}{\left\{1+(k/k_0)^{\frac{8}{3}}\right\}^3}$$

$$\rightarrow \frac{d}{d\omega}W(\omega) = \frac{-\frac{5}{3}\frac{1}{v_b}k^{-\frac{8}{3}}\left[1+\frac{21}{5}(k/k_0)^{\frac{8}{3}}\right]}{\left\{1+(k/k_0)^{\frac{8}{3}}\right\}^3} \tag{A.6}$$

Inserting Eq. A.6 in Eq. A.5 gives:

$$\Phi(k) = -\frac{Bv_b}{4\pi^2 k}\cdot\left(-\frac{5}{3}\frac{k^{-\frac{8}{3}}}{v_b}\frac{1+\frac{21}{5}(k/k_0)^{\frac{8}{3}}}{\left\{1+(k/k_0)^{\frac{8}{3}}\right\}^3}\right) \tag{A.7}$$

Thus the 3-dimensional spectrum for the Heisenberg spectrum is given by:

$$\Phi(k) = \frac{B}{4\pi^2}\cdot\frac{5}{3}k^{-\frac{11}{3}}\cdot\frac{1+\frac{21}{5}(k/k_0)^{\frac{8}{3}}}{\left\{1+(k/k_0)^{\frac{8}{3}}\right\}^3} \tag{A.8}$$

The 3-dimensional spectrum Φ must obey the condition [*Lübken* [1993], p. 43, Eq. 3.108 and *Tatarskii* [1971], p.65]:

$$\frac{d^2}{dr^2}\mathrm{D}(0) = \frac{8\pi}{3}\int_0^\infty \Phi(k)k^4\,\mathrm{d}k \tag{A.9}$$

The structure function D for temperature fluctuations in the viscous subrange is given by [*Lübken* [1993], p.38 and *Tatarskii* [1971], p. 63]:

$$\mathrm{D}(r) = \frac{1}{f_\alpha}\frac{1}{3}\frac{N}{D}r^2 \tag{A.10}$$

where N represents the amount of inhomogeneity which disappears per unit time due to molecular diffusion and D is the molecular diffusion coefficient. The factor f_α takes into account the different normalization used for the inhomogeneity. In the case of temperature fluctuations f_α is taken as 2 [see *Lübken*, 1993, p. 27].

With Eq. A.10 Eq. A.9 forms to:

$$\frac{d^2}{dr^2}\mathrm{D}(0) = \frac{1}{f_\alpha}\frac{2}{3}\frac{N}{D} = \frac{8\pi}{3}\int_0^\infty \Phi(k)k^4\,\mathrm{d}k \tag{A.11}$$

Inserting Eq. A.8 in Eq. A.11 gives:

$$\frac{1}{f_\alpha}\frac{2}{3}\frac{N}{D} = \frac{8\pi}{3}\int_0^\infty \frac{B}{4\pi^2}\cdot\frac{5}{3}k^{-\frac{11}{3}}\cdot\frac{1+\frac{21}{5}(k/k_0)^{\frac{8}{3}}}{\left\{1+(k/k_0)^{\frac{8}{3}}\right\}^3}\cdot k^4\,\mathrm{d}k \tag{A.12}$$

$$\frac{1}{f_\alpha}\frac{2}{3}\frac{N}{D} = \frac{8\pi}{3}\frac{B}{4\pi^2}\cdot\frac{5}{3}\int_0^\infty \frac{1+\frac{21}{5}(k/k_0)^{\frac{8}{3}}}{\left\{1+(k/k_0)^{\frac{8}{3}}\right\}^3}\cdot k^{\frac{1}{3}}\,\mathrm{d}k = \frac{10\,B}{9\,\pi}\int_0^\infty \frac{1+\frac{21}{5}(k/k_0)^{\frac{8}{3}}}{\left\{1+(k/k_0)^{\frac{8}{3}}\right\}^3}\cdot k^{\frac{1}{3}}\,\mathrm{d}k \tag{A.13}$$

By substituting $s = k/k_0$ ($\mathrm{d}s = \mathrm{d}k/k_0 \rightarrow \mathrm{d}k = k_0\,\mathrm{d}k$) one finds:

$$\frac{1}{f_\alpha}\frac{2}{3}\frac{N}{D} = \frac{10\,B}{9\,\pi}\int_0^\infty \frac{1+\frac{21}{5}s^{\frac{8}{3}}}{\left\{1+s^{\frac{8}{3}}\right\}^3} k_0 (k_0 s)^{\frac{1}{3}}\,\mathrm{d}s \tag{A.14}$$

$$\frac{1}{f_\alpha}\frac{2}{3}\frac{N}{D} = \frac{10\,B}{9\,\pi}\cdot k_0^{\frac{4}{3}}\int_0^\infty \frac{1+\frac{21}{5}s^{\frac{8}{3}}}{\left\{1+s^{\frac{8}{3}}\right\}^3} s^{\frac{1}{3}} ds \tag{A.15}$$

After integration it follows:

$$\frac{1}{f_\alpha}\frac{2}{3}\frac{N}{D} = \frac{10\,B}{9\,\pi}\cdot k_0^{\frac{4}{3}}\cdot\frac{27\pi}{80} \tag{A.16}$$

$$k_0^{\frac{4}{3}} = \frac{2N}{3f_\alpha D}\cdot\frac{9\pi}{10B}\cdot\frac{80}{27\pi} = \frac{16N}{9f_\alpha BD} \tag{A.17}$$

with $B = \Gamma(5/3)\sin(\pi/3)\cdot C_T^2$

$$k_0^{\frac{4}{3}} = \frac{16\,N}{9\,f_\alpha\,\Gamma(5/3)\,\sin(\pi/3)\,C_T^2\,D} \tag{A.18}$$

The structure function constant for temperature fluctuations is defined as $C_T^2 = \alpha^2 N/\varepsilon^{1/3}$ [*Lübken* [1993], p. 37 and *Tatarskii* [1971], p. 66] where α is a numerical constant and N the inhomogeneity dissipation rate. Inserting in Eq. A.18 gives:

$$k_0^{\frac{4}{3}} = \frac{16\,\varepsilon^{\frac{1}{3}}}{9\,f_\alpha\,\Gamma(5/3)\,\sin(\pi/3)\,\alpha^2\,D} \tag{A.19}$$

With the molecular Prandtl number $Pr^{mol} = \nu/D$:

$$k_0^{\frac{4}{3}} = \frac{16\,Pr^{mol}\,\varepsilon^{\frac{1}{3}}}{9\,f_\alpha\,a^2\,\Gamma(5/3)\,\sin(\pi/3)\,\nu} \tag{A.20}$$

$$\frac{1}{k_0} = \left(\frac{9\,f_\alpha\,\alpha^2\,\Gamma(5/3)\,\sin(\pi/3)}{16\,Pr^{mol}}\cdot\frac{\nu}{\varepsilon^{\frac{1}{3}}}\right)^{\frac{3}{4}} \tag{A.21}$$

with $l_0 = 2\pi/k_0$

$$l_0 = 2\pi \cdot \left(\frac{9\, f_\alpha\, \alpha^2\, \Gamma(5/3)\, \sin(\pi/3)}{16\, Pr^{mol}} \cdot \frac{\nu}{\varepsilon^{\frac{1}{3}}} \right)^{\frac{3}{4}} \tag{A.22}$$

$$l_0 = 2\pi \cdot \left(\frac{9\, f_\alpha\, \alpha^2\, \Gamma(5/3)\, \sin(\pi/3)}{16\, Pr^{mol}} \right)^{\frac{3}{4}} \left(\frac{\nu^3}{\varepsilon} \right)^{\frac{1}{4}} \tag{A.23}$$

With $\alpha^2 = 1.74$, $\Gamma(5/3) = 0.9027$, $f_\alpha = 2$ and $Pr^{mol} = 0.73$ (calculation of Pr^{mol} [see *Lübken*, 1993, Appendix A] one gets:

$$l_0 = 10.9 \cdot \left(\frac{\nu^3}{\varepsilon} \right)^{\frac{1}{4}} \tag{A.24}$$

Appendix B

Determination of inner scale for velocity fluctuations

The structure function D for velocity fluctuations in the viscous subrange is given by [*Tatarskii*, 1971, p.49]:

$$\mathrm{D_{ii}}(r) = \frac{1}{f_\alpha}\frac{1}{3}\frac{\varepsilon}{\nu}r^2 \tag{B.1}$$

where ε is the energy dissipation rate and ν is the kinematic viscosity. The factor f_α takes into account the different normalization used for the inhomogeneity. In the case of velocity fluctuations the inhomogeneity in a volume V is equivalent to the kinetic energy per unit mass and f_α is taken as 1 [see *Lübken*, 1993, p. 27]. D_{ii} is the sum of the transversal component D_{tt} and the longitudinal component D_{rr} of velocity fluctuations. It is defined as: $D_{ii}(r) = 2D_{tt} + D_{rr}$.

Thus Eq. A.9 forms to:

$$\frac{d^2}{dr^2}\mathrm{D}(0) = \frac{1}{f_\alpha}\frac{2}{3}\frac{\varepsilon}{\nu} = \frac{8\pi}{3}\int_0^\infty \Phi(k)k^4\,\mathrm{d}k \tag{B.2}$$

Inserting Eq. A.8 in Eq. B.2 gives:

$$\frac{1}{f_\alpha}\frac{2}{3}\frac{\varepsilon}{\nu} = \frac{8\pi}{3}\int_0^\infty \frac{B}{4\pi^2}\cdot\frac{5}{3}k^{-\frac{11}{3}}\cdot\frac{1+\frac{21}{5}(k/k_0)^{\frac{8}{3}}}{\left\{1+(k/k_0)^{\frac{8}{3}}\right\}^3}\cdot k^4\,\mathrm{d}k \tag{B.3}$$

$$\frac{1}{f_\alpha}\frac{2}{3}\frac{\varepsilon}{\nu} = \frac{8\pi}{3}\frac{B}{4\pi^2}\cdot\frac{5}{3}\int_0^\infty \frac{1+\frac{21}{5}(k/k_0)^{\frac{8}{3}}}{\left\{1+(k/k_0)^{\frac{8}{3}}\right\}^3}\cdot k^{\frac{1}{3}}\,\mathrm{d}k = \frac{10\,B}{9\,\pi}\int_0^\infty \frac{1+\frac{21}{5}(k/k_0)^{\frac{8}{3}}}{\left\{1+(k/k_0)^{\frac{8}{3}}\right\}^3}\cdot k^{\frac{1}{3}}\,\mathrm{d}k \quad \text{(B.4)}$$

By substituting $s = k/k_0$ ($\mathrm{d}s = \mathrm{d}k/k_0 \rightarrow \mathrm{d}k = k_0\,\mathrm{d}s$) one finds:

$$\frac{1}{f_\alpha}\frac{2}{3}\frac{\varepsilon}{\nu} = \frac{10\,B}{9\,\pi}\int_0^\infty \frac{1+\frac{21}{5}s^{\frac{8}{3}}}{\left\{1+s^{\frac{8}{3}}\right\}^3}k_0(k_0 s)^{\frac{1}{3}}\,\mathrm{d}s \quad \text{(B.5)}$$

$$\frac{1}{f_\alpha}\frac{2}{3}\frac{\varepsilon}{\nu} = \frac{10\,B}{9\,\pi}\cdot k_0^{\frac{4}{3}}\int_0^\infty \frac{1+\frac{21}{5}s^{\frac{8}{3}}}{\left\{1+s^{\frac{8}{3}}\right\}^3}s^{\frac{1}{3}}\,\mathrm{d}s \quad \text{(B.6)}$$

After integration it follows:

$$\frac{1}{f_\alpha}\frac{2}{3}\frac{\varepsilon}{\nu} = \frac{10\,B}{9\,\pi}\cdot k_0^{\frac{4}{3}}\cdot\frac{27\pi}{80} \quad \text{(B.7)}$$

$$k_0^{\frac{4}{3}} = \frac{1}{f_\alpha}\frac{2\varepsilon}{3\nu}\cdot\frac{9\pi}{10B}\cdot\frac{80}{27\pi} = \frac{16\,\varepsilon}{9B\,f_\alpha\nu} \quad \text{(B.8)}$$

with $B = \Gamma(5/3)\sin(\pi/3)\cdot C_V^2$

$$k_0^{\frac{4}{3}} = \frac{16\,\varepsilon}{9\,f_\alpha\,\Gamma(5/3)\,\sin(\pi/3)\,C_V^2\,\nu} \quad \text{(B.9)}$$

The structure function constant for velocity fluctuations is defined as $C_V^2 = 4\alpha\cdot\varepsilon^{2/3}$ [*Barat and Bertin*, 1984b]. Consequently

$$k_0^{\frac{4}{3}} = \frac{16\,\varepsilon}{9\,f_\alpha\,\Gamma(5/3)\,\sin(\pi/3)\,4\alpha\,\varepsilon^{2/3}\,\nu} \quad \text{(B.10)}$$

$$\frac{1}{k_0} = \left(\frac{9\,f_\alpha\,\alpha\,\Gamma(5/3)\,\sin(\pi/3)\,\nu}{4\,\varepsilon^{1/3}}\right)^{\frac{3}{4}} \quad \text{(B.11)}$$

with $l_0 = 2\pi/k_0$

$$l_0 = 2\pi \cdot \left(\frac{9\, f_\alpha\, \alpha\, \Gamma(5/3)\, \sin(\pi/3)}{4} \cdot \frac{\nu}{\varepsilon^{\frac{1}{3}}} \right)^{\frac{3}{4}} \tag{B.12}$$

$$l_0 = 2\pi \cdot \left(\frac{9\, f_\alpha\, \alpha\, \Gamma(5/3)\, \sin(\pi/3)}{4} \right)^{\frac{3}{4}} \left(\frac{\nu^3}{\varepsilon} \right)^{\frac{1}{4}} \tag{B.13}$$

Since velocity fluctuations are considered, f_α is taken as 1 *Lübken* [1992, 1993]. The empirical constant α is taken as 0.5 [*Bertin et al.*, 1997; *Antonia et al.*, 1981] and with $\Gamma(5/3) = 0.9027$ one gets:

$$l_0 = 5.7 \cdot \left(\frac{\nu^3}{\varepsilon} \right)^{\frac{1}{4}} \tag{B.14}$$

Appendix C

Discussion of CTA sensitivity

The laboratory results shown in Sect. 3.2.1 and 3.2.2 reveal a non-linear dependence of the sensor sensitivity $\Delta voltage/\Delta velocity$ with respect to pressure and furthermore a decreasing sensitivity of the sensor response with decreasing pressure. In addition, the sensor sensitivity also varies for different wind velocities. In other words, the sensor sensitivity depends not only on pressure but also on the relative background wind. Since relative wind velocities up to 2 m/s are observed with LITOS, the measurements are in the region with the largest influence of pressure and relative background wind. The question arises whether this could influence our turbulence measurements, i.e. the slope of the turbulence spectrum. Thus, voltage fluctuations between 26 550 and 26 650 m are exemplarily normalized to the relative background wind measured simultaneously by the radiosonde. Due to the lower sampling rate of the radiosonde data (1 s) the values are interpolated to the sampling rate of the measured voltage fluctuations (0.5 ms) and therewith derived a value of the relative background wind for each value of the fluctuations. Based on the 100 hPa curve (Fig. 3.11) an individual correction factor for the sensor sensitivity of each value along the data sequence according to the relative wind at 26 550 m, i.e. the first value of the sequence is determined. In fact, by using the 100 hPa curve for this sequence, the influence of the relative background wind is overestimated. As can be seen from Fig. 3.11, the sensitivity change decreases with decreasing pressure, so at an altitude of 26 550 m (about 18 hPa) it is very likely that the sensitivity varies less than at 100 hPa. Unfortunately, due to technical limitation of the wind calibration unit, no measurements of pressure values below 100 hPa could be obtained. (The 50 hPa values are omitted due to remaining ambiguities.) Nevertheless, by applying the individual correction factor (obtained at 100 hPa) to the measured voltage fluctuations in the sequence, the influence of the background relative wind is eliminated. Figure C.1 shows the uncorrected signal (black) and the corrected signal (red) together with the relative wind measured by the radiosonde (blue). The influence of the relative background wind is obviously rather small. Furthermore the spectra of the corrected and uncorrected signals are quite similar (Fig. C.2). Here the largest deviations appear at larger spatial scales and decrease down to smaller scales. The resulting energy dissipation rates for the corrected and uncorrected spectra deviate by $\sim$2 %. Thus it is well justified to use the uncorrected signal for the determination of turbulence parameters.

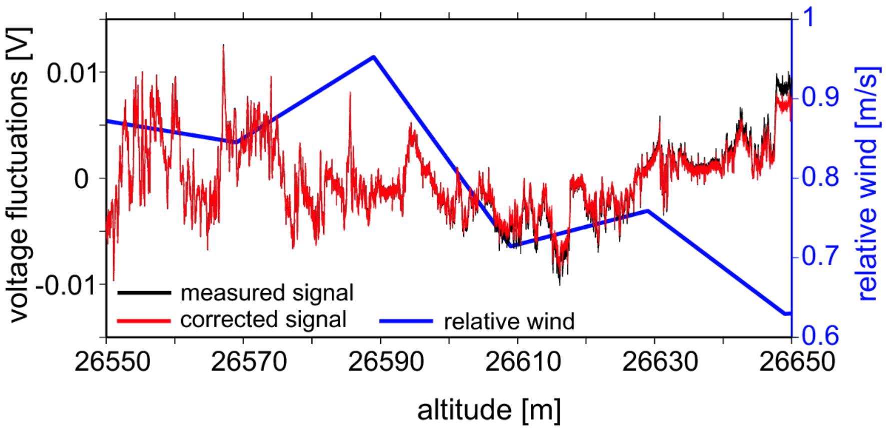

Figure C.1.: Voltage fluctuations for the altitude region of 26 550 m–26 650 m. The black line shows the measured fluctuations and the red line shows the fluctuation corrected for changes of background relative wind. The blue line presents the relative wind measured by radiosonde (used for the correction).

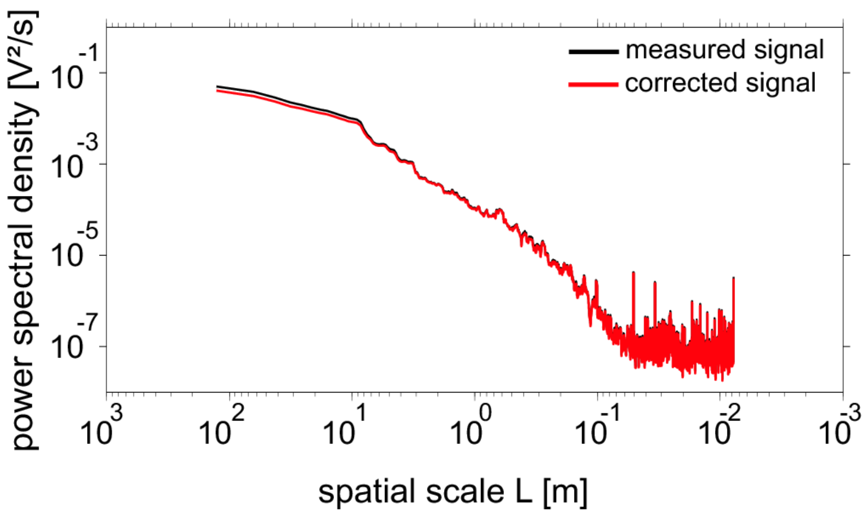

Figure C.2.: Spectra of the corrected (red) and uncorrected (black) voltage fluctuations from Fig. C.1.

Appendix D

Analyses of gondola movements

In order to estimate the gondola movements during the flight, a housekeeping device measuring the rotation and pendulum motion displacement has been integrated into the LITOS payload. The data have been kindly provided by A. Schneider (IAP). Figure D.1 resents the gondola movements of the small LITOS gondola during a test flight between 12 and 12.3 km. During this flight, only one wind vane has been mounted to the payload box to stabilize the gondola. The profile of the pendulum motion shows fast and frequent movements of the gondola. The rotation profile shows a varying azimuth angle (i.e. rotation) of the gondola of up to 100 ° below 12.15 km and even complete turns of the gondola within a short period of time above this altitude. Those motions strongly influence the turbulence measurements of LITOS and further improvements of the attitude control of the gondola have to be made. Figure D.2 shows the gondola movements during a flight from Kühlungsborn with an improved configuration of wind vanes. Now, the fast and frequent pendulum motion could be reduced to a slower motion of the gondola. Also the rotation of the gondola has been significantly reduced. Only slow rotation over several ten degrees occurs. In comparison, Fig. D.3 shows the movements of the bigger BEXUS 8 gondola. It is clearly visible, that the gondola moves less compared to Kühlungsborn. Especially, the pendulum motion varies less then 1 °. The gondola rotates quite slowly. These slow movements are easily removed from the measured signal and do not hamper the turbulence analyses. Therefore this study focuses on the results of the Kiruna flights. Further improvements of the attitude control of the small gondola are planned.

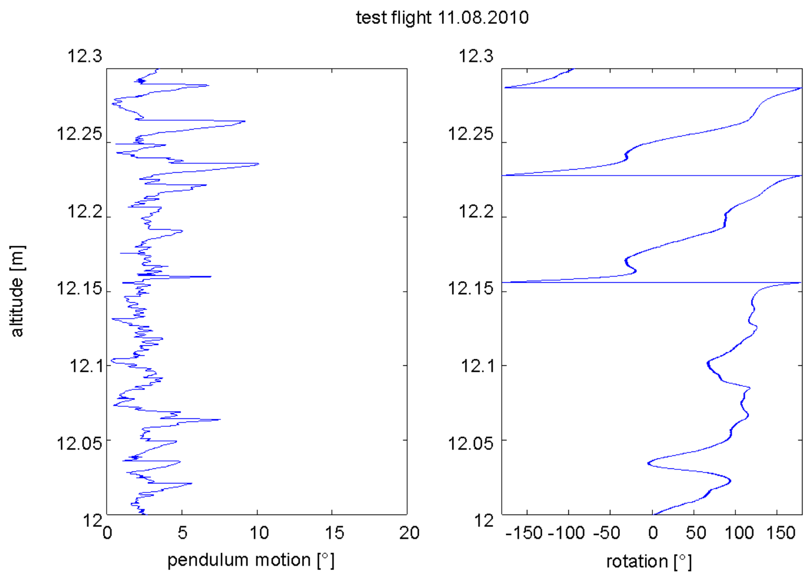

Figure D.1.: Pendulum motion and rotation of the small LITOS gondola with one wind vane.

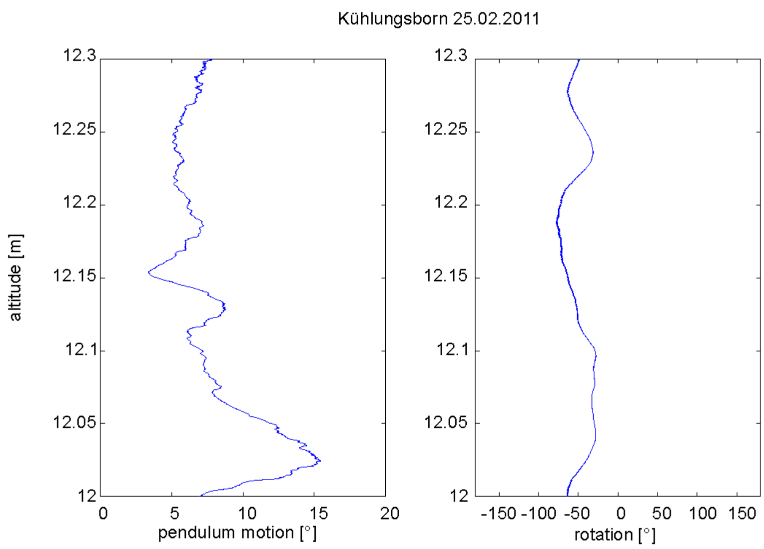

Figure D.2.: Pendulum motion and rotation of the small LITOS gondola in Kühlungsborn with improved wind vane combination.

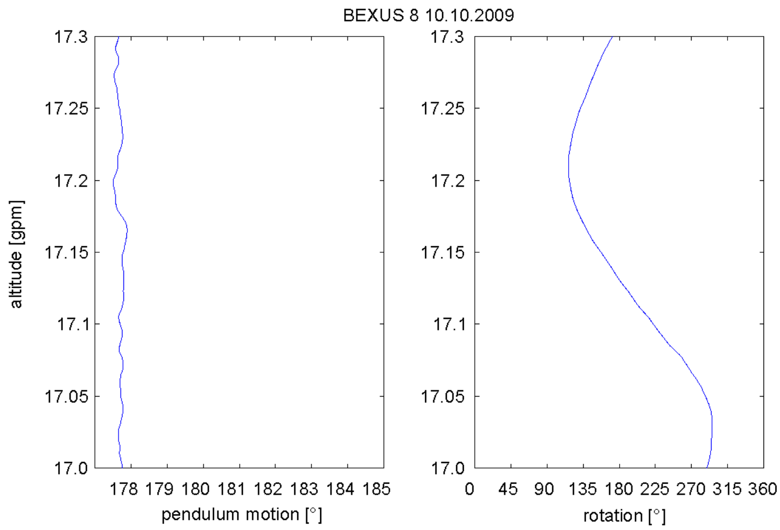

Figure D.3.: Pendulum motion and rotation of the BEXUS 8 gondola during flight.

Appendix E

Radiosonde data

E.1. BEXUS 6

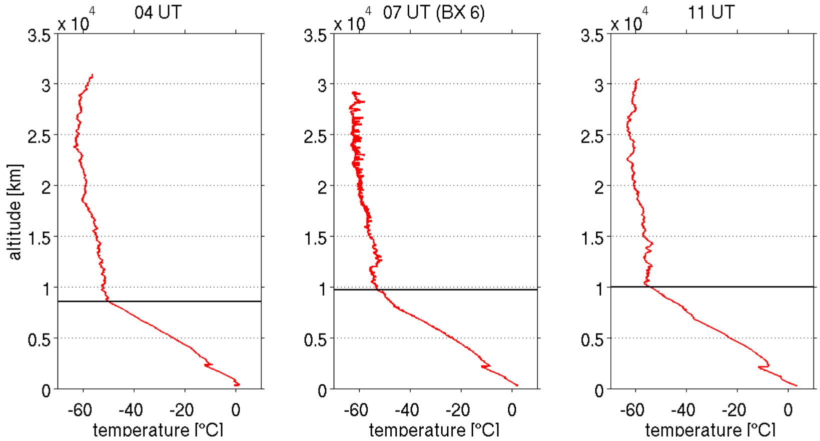

Figure E.1.: Temperature profiles of the radiosondes during the BEXUS 6 campaign.

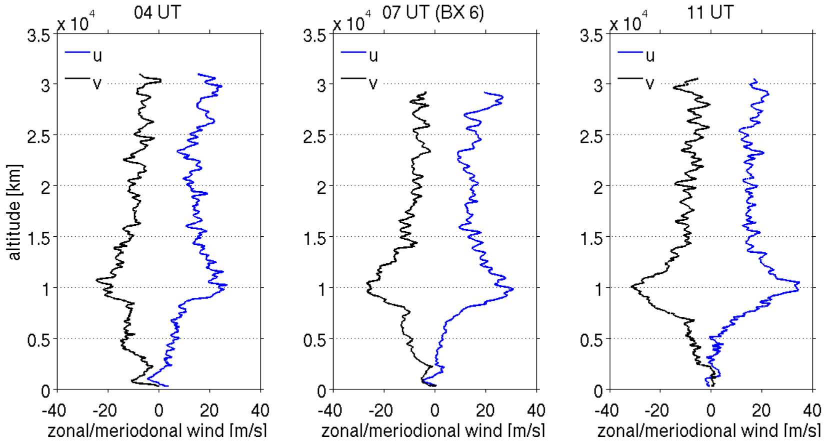

Figure E.2.: Meridional and zonal wind profiles of the radiosondes during the BEXUS 6 campaign.

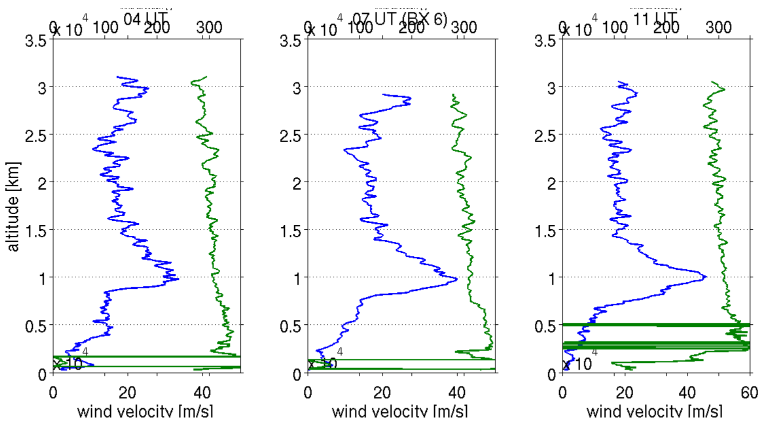

Figure E.3.: Wind speed and wind direction profiles of the radiosondes during the BEXUS 6 campaign.

E.2. BEXUS 8

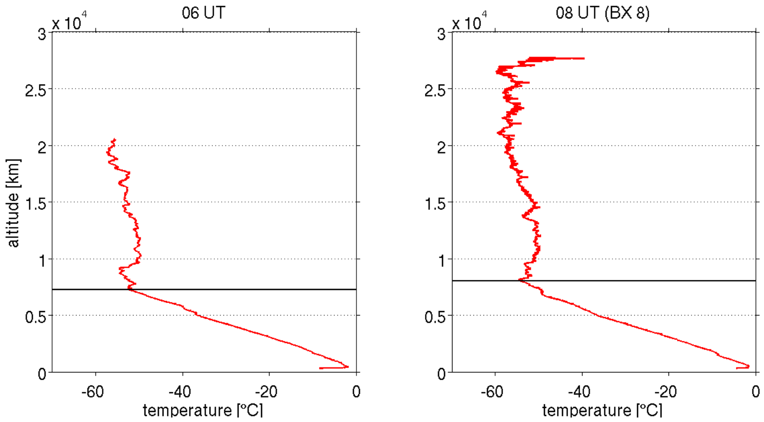

Figure E.4.: Temperature profiles of the radiosondes during the BEXUS 8 campaign.

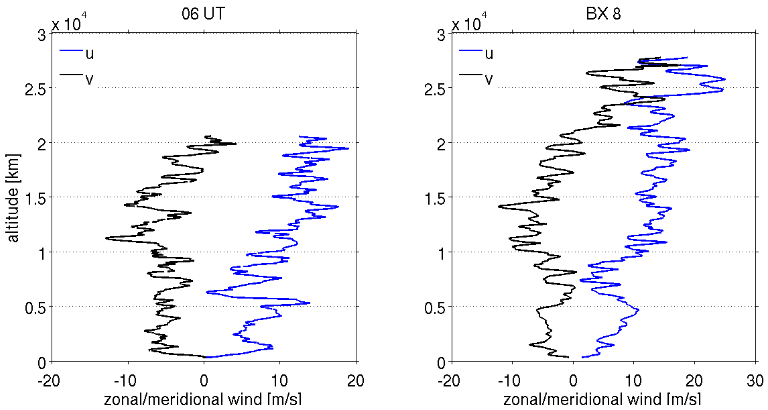

Figure E.5.: Meridional and zonal wind profiles of the radiosondes during the BEXUS 8 campaign.

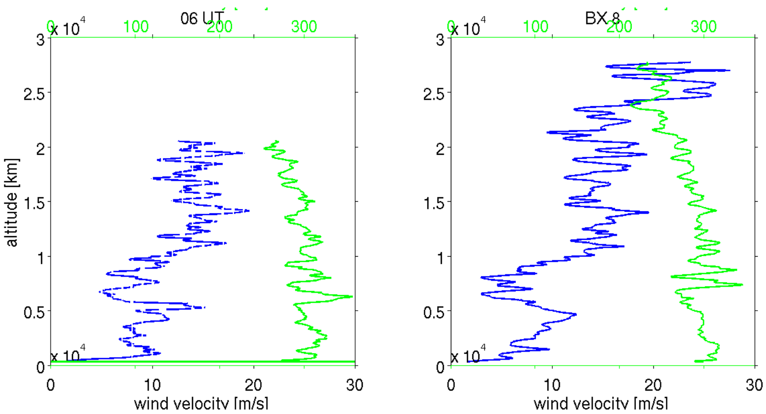

Figure E.6.: Wind speed and wind direction profiles of the radiosondes during the BEXUS 8 campaign.

Appendix F

Gravity wave analyses

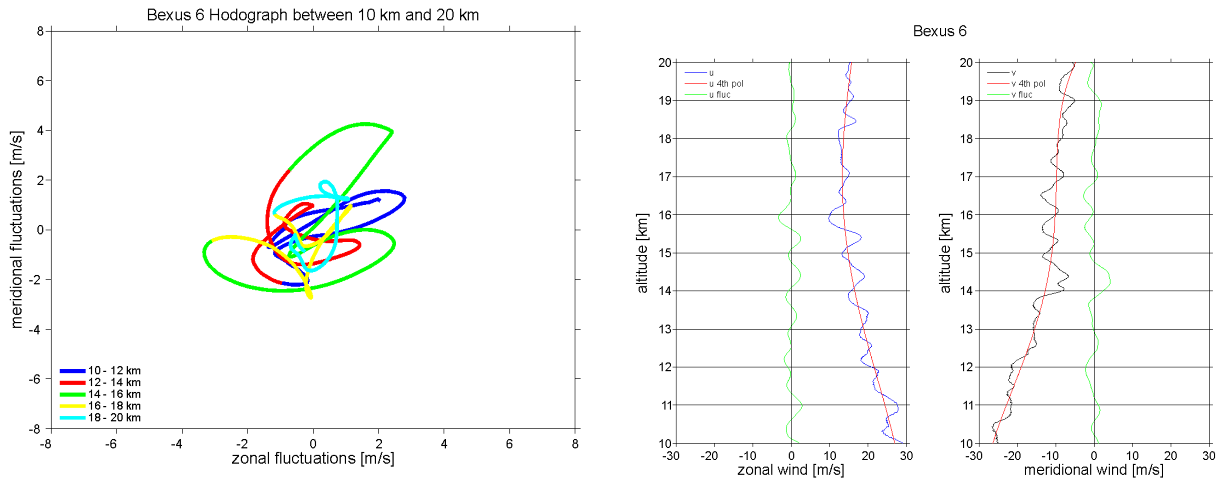

Figure F.1.: Top: Hodograph of the altitude region between 10 km and 20 km of the BEXUS 6 flight. Bottom: Profiles of the wind component u (blue), left panel, and v (black), right panel, together with the 4th order polynomial (red) and the profiles of u' and v' (green).

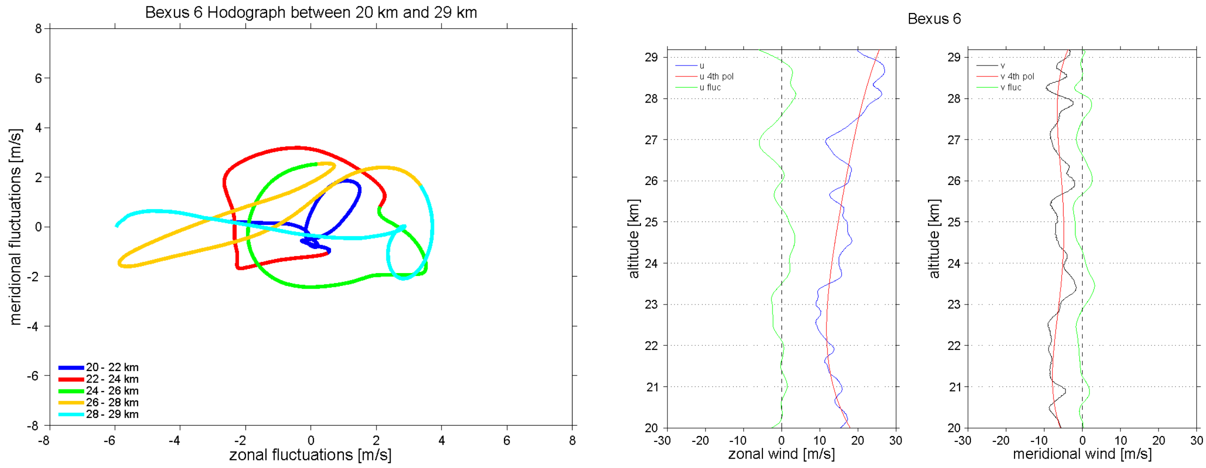

Figure F.2.: Top: Hodograph of the altitude region between 20 km and 29 km of the BEXUS 6 flight. Bottom: Profiles of the wind component u (blue), left panel, and v (black), right panel, together with the 4th order polynomial (red) and the profiles of u' and v' (green).

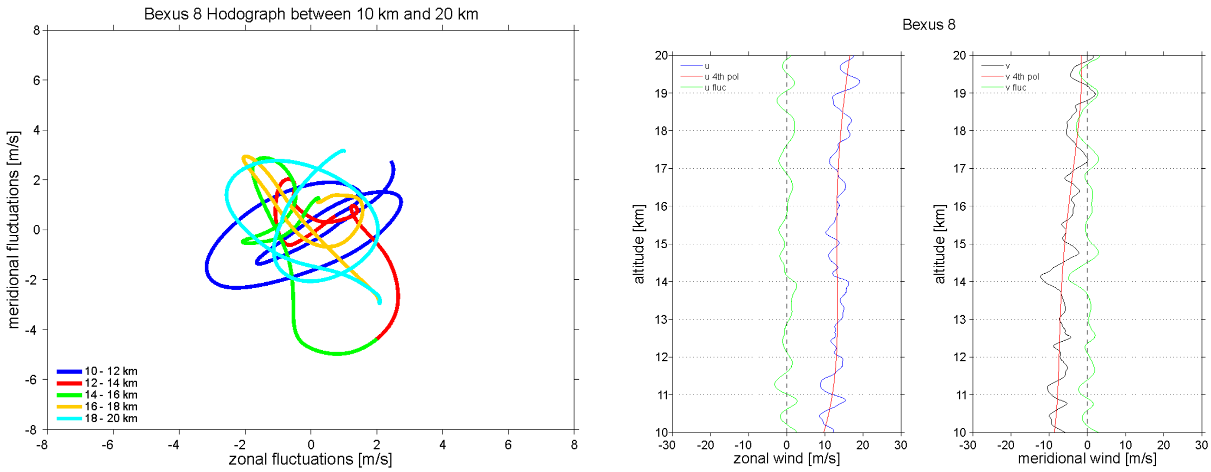

Figure F.3.: Top: Hodograph of the altitude region between 10 km and 20 km of the BEXUS 8 flight. Bottom: Profiles of the wind component u (blue), left panel, and v (black), right panel, together with the 4th order polynomial (red) and the profiles of u' and v' (green).

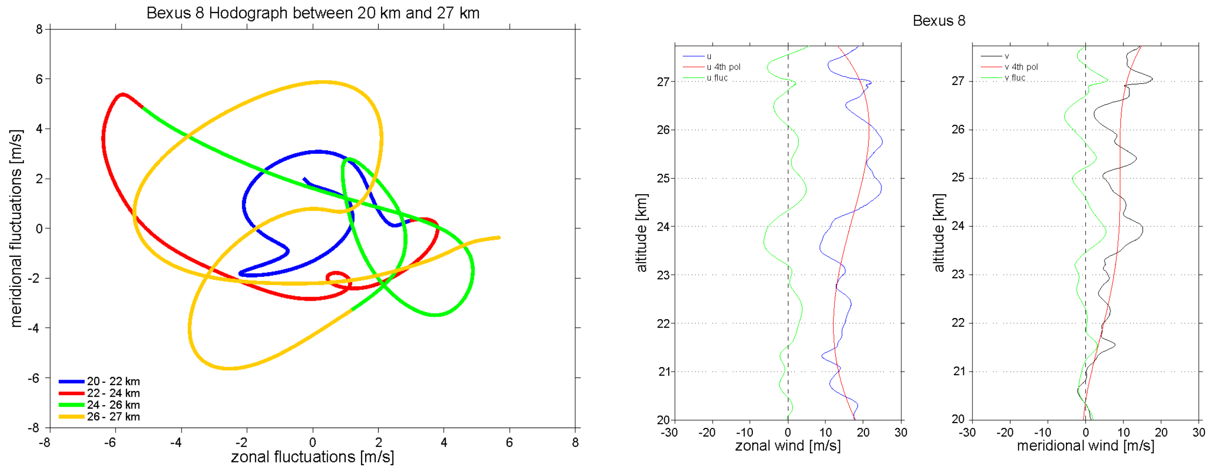

Figure F.4.: Top: Hodograph of the altitude region between 20 km and 27 km of the BEXUS 8 flight. Bottom: Profiles of the wind component u (blue), left panel, and v (black), right panel, together with the 4th order polynomial (red) and the profiles of u' and v' (green).

Bibliography

Achatz, U., On the role of optimal perturbations in the instability of monochromatic gravity waves, *Phys. FLuids*, *17 (9)*, 094,107, 2005.

Achatz, U., The primary nonlinear dynamics of modal and nonmodal perturbations of monochromatic inertia-gravity waves, *J.Atmos*, *64*, 74 – 95, 2007.

Alexander, S., and T. Tsuda, High-resolution radio acoustic sounding system observations and analysis up to 20 km, *J. Atmos. Oceanic Technol.*, *25*, 1383 – 1396, 2008.

Antonia, R., A. Chambers, and B. Satyaprakash, Kolmogorv constants for structure functions in turbulent shear flows, *Quart. J. R. Met. Soc.*, *107*, 579–589, 1981.

Assmann, R., Über die existenz eines wärmeren luftstromes in der höhe von 10 bis 15 km., *Sitzungsber. K. Preuss. Akad. Wiss*, *24*, 1–10, 1902.

Baldwin, M. P., M. Dameris, and T. G. Shepherd, How will the stratosphere affect climate change, *Science*, *316*, 1576 – 1577, 2007.

Balsley, B. B., G. Svensson, and M. Tjernström, On the scale-dependence of the gradient richardson number in the residual layer, *Bound.-Layer Meteor.*, *127*, 57–72, 2008.

Barat, J., Some characteristics of clear air turbulence in the middle stratosphere, *J. Atmos. Sci.*, *39*, 2553–2564, 1982a.

Barat, J., Initial results from the use of ionic anemometers under stratospheric balloons: Application to the high resolution analysis of stratospheric motions, *J. Appl. Meteor.*, *21*, 1489–1496, 1982b.

Barat, J., The fine structure of the stratosphere flow revealed by differential sounding, *J. Geophys. Res.*, *88*, 5219–5228, 1983.

Barat, J., and P. Aimedieu, The external scale of clear air turbulence derived from the vertical ozone profile: Application to vertical transport measurements, *J. Appl. Meteor.*, *20*, 275 – 280, 1981.

Barat, J., and F. Bertin, On the contamination of stratospheric turbulence measurements by wind shear, *J. Atmos. Sci.*, *41*, 819–827, 1984a.

Barat, J., and F. Bertin, Simultaneous measurements of temperature and velocity fluctuations within clear air turbulence layers: Analysis of the estimates of dissipation rate by remote sensing techniques, *J. Atmos. Sci.*, *41*, 1613–1619, 1984b.

Barat, J., and C. Cot, Simultaneous measurements of wind shear and temperature gradient spectra in the stratosphere, *Geophys. Res. Lett.*, *16*, 1161–1164, 1989a.

Barat, J., and C. Cot, Spectral analysis of high resolution temperature profiles in the stratosphere, *Geophys. Res. Lett.*, *16*, 1165–1168, 1989b.

Barat, J., and C. Cot, Wind shear rotary spectra in the stratosphere, *Geophys. Res. Lett.*, *19*, 103–106, 1992.

Barat, J., and C. Cot, Accuracy analysis of rubsonde-gps wind sounding system, *J. Appl. Meteor.*, *34*, 1123–1132, 1995.

Barat, J., and J. Genie, A new tool for the three-dimensional sounding of the atmosphere: The heliosonde, *J. Appl. Meteor.*, *21*, 1497–1505, 1982.

Barat, J., C. Cot, and C. Sidi, On the measurement of the turbulence dissipation rate from rising balloons, *J. Atmos. Oceanic Technol.*, *1*, 270–275, 1984.

Batchelor, G. K., *The theory of homogeneous turbulence*, Cambridge University Press, 1993.

Bertin, F., J. Barat, and R. Wilson, Energy dissipation rates, eddy diffusivity, and the prandtl number: An in situ experimental approach and its consequences in radar estimate of turbulent parameters, *Radio Sci.*, *32*, 791–804, 1997.

Brewer, A., Evidence for a world circulation provided by the measurements of helium and water vapor distribution in the stratosphere, *Qua*, *75*, 351 – 363, 1949.

Bruun, H., *Hot-wire anemometry - principles and signal analysis*, Oxford Science Publication, 1995.

Bruun, H. H., Interpretation of a hot wire signal using a universal calibration law, *J. Phys. E: Sci. Instrum.*, *4*, 225–231, 1970.

Bruun, H. H., M. A. Khan, H. H. Al-Kayiem, and A. A. Fardad, Velocity calibration relationships for hot-wire anemometry, *J. Phys. E: Sci. Instrum.*, *21*, 225–232, 1988.

Cardell, G., A note on the temperature-dependent hot-wire calibration method of cimbala and park, *Exp. Fluids*, *14*, 283–285, 1993.

Cimbala, J. M., and W. J. Park, A direct hot-wire calibration technique to account for ambient temperature drift in incompressible flow, *Exp. Fluids*, *8*, 299–300, 1990.

Clayson, C. A., and L. Kantha, On turbulence and mixing in the free atmosphere inferred from high-resolution soundings, *J. Atmos. Oceanic Technol.*, *25*, 833–852, 2008.

Collis, D. C., and J. Williams, Two-dimensional convection from heated wires at low reynolds numbers, *J. Fluid Mech.*, *6*, 357–389, 1959.

Comte-Bellot, G., Hot-wire anemomentry, *Annu. Rev. Fluid Mech.*, *8*, 209–231, 1976.

Coulman, C. E., J. Vernin, and A. Fuchs, Optical seeing-mechanism of formation of this turbulent laminae in the atmosphere, *Appl. Opt.*, *34*, 5461 – 5474, 1995.

Dalaudier, F., and C. Sidi, Direct evidence of 'sheets' in the atmospheric temperature field, *J. Atmos. Sci.*, *51*, 237–248, 1994.

Dalaudier, F., M. Crochet, and C. Sidi, Direct comparison between in situ and radar measurements of temperature fluctuation spectra: A puzzling result, *Radio Science*, *24*, 311–324, 1989.

Devienne, F. M., Low-density heat transfer, *Advances in Heat Transfer*, *2*, 271–356, 1965.

Dobson, G., Origin and distribution of the polyatomic molecules in the atmosphere, *Proc. Roy. Soc. Lond. A*, *236*, 187 – 193, 1956.

Dörnbrack, A., R. J. Leutbecher, M., A. Behrendt, K.-P. Müller, and G. Baumgarten, Relevance of mountain wave cooling for the formation of polar stratospheric clouds over scandinavia: Mesoscale dynamics and observations for january 1997, *J. Geophys. Res.*, *106*, 1569 – 1581, 2001.

Durst, F., *An Introduction to the Theory of Fluid Flows*, Springer-Verlag Berlin, 2008.

Durst, F., S. Noppenberger, M. Sill, and H. Venzke, Influence of humidity on hot-wire measurements, *Meas. Sci. Technol.*, *7*, 1517–1528, 1996.

Eckermann, S., Hodographic analysis of gravity waves: relationships among stokes parameters, rotary spectra and cross-spectral methods, *J. Geophys. Res.*, *101*, 19,169 – 19,174, 1996.

Engel, A., et al., Age of stratospheric air unchanged within uncertainties over the past 30 years, *Nature Geoscience*, *2*, 28 – 31, 2009.

Engler, N., R. Latteck, B. Strelnikov, W. Singer, and M. Rapp, Turbulent energy dissipation rates observed by doppler mst radar and by rocket-borne instruments during the midas/macwave campaign 2002, *Ann. Geophys.*, *23*, 1147–1156, 2005.

Frehlich, R., Y. Meillier, M. L. Jensen, and B. Balsley, Turbulence measurements with the cires tethered lifting system during cases - 99: calibration and spectral analysis of temperature and velocity, *J. Atmos. Sci.*, *60*, 2487 – 2495, 2003.

Frisch, U., *Turbulence - The legacy of A.N. Kolmogorov*, Cambridge University Press, 1995.

Fritts, D., and M. Alexander, Gravity wave dynamics and effects in the middle atmosphere, *Rev. Geophys.*, *41*, 1003, doi:10.1029/2001RG000106, 2003.

Fritts, D., C. Bizon, J. Werne, and C. Meyer, Layering accompanaying turbulence generation due to shear instability and gravity-wave breaking, *J. Geophys. Res.*, *108*, 2003.

Gadsden, M., and W. Schöder, *Noctilucent clouds*, Springer-Verlag Berlin, 1989.

Galperin, B., S. Sukoriansky, and P. Anderson, On the critical richardson number in stably stratified turbulence, *Atmos. Sci. Let.*, *8*, 65–69, 2007.

Gavrilov, N., H. Luce, M. Crochet, F. Dalaudier, and S. Fukao, Turbulence parameter estimations from high-resolution balloon temperature measurements of mutsi-2000 campaign, *Ann.Geophys.*, *23*, 2401–2413, 2005.

Gerber, E., et al., Assessing and understanding the impact of stratospheric dynamics and variability on the earth system, *Bull. Am. Meteorol. Soc.*, *93*, 845–859, 2012.

Gerding, M., J. Höffner, J. Lautenbach, M. Rauthe, and F.-J. Lübken, Seasonal variation of nocturnal temperatures between 1 and 105 km altitude at 54°N observed by lidar, *Atmos. Chem. Phys.*, *8*, 7465–7482, 2008.

Gerding, M., A. Theuerkauf, O. Suminska, T. Köpnick, and F.-J. Lübken, Balloon-borne hot wire anemometer for stratospheric turbulence soundings, *Proceedings of the 19th ESA Symposium on European Rocket and Balloon Programmes and Related Research*, *SP-671*, 175–180, 2009.

Gurvich, A. S., and V. L. Brekhovskikh, Study of the turbulence and inner waves in the stratosphere based on the observations of stellar scintillations from space: a model of scintillation spectra, *Waves in Random and Complex Media*, *11*, 163–181, 2001.

Heisenberg, W., Zur statistischen theorie der turbulenz, *Z. Phys.*, *124*, 628–657, 1948.

Hinze, J., *Turbulence - An introduction to its mechanism and theory*, McGraw-Hill book company, 1959.

Hocking, W., Turbulence in the region 80-120 km, *Adv. Space Res.*, *10*(12), 153–161, 1990.

Hocking, W., The dynamical parameters of turbulence theory as they apply to middle atmosphere studies, *Earth, Planets Space*, *51*, 525–541, 1999.

Hocking, W., and P. K. L. Mu, Upper and middle tropospheric kinetic energy dissipation rates from measurements of c_n^2 - review of theories, in-situ investigations, and experimental studies using the buckland park atmospheric radar in australia, *J. Atmos. Solar-Terr. Phys.*, *59*, 1779–1803, 1997.

Hocking, W., and J. Röttger, The structure of turbulence in the middle and lower atmosphere seen by and deduced from mf, hf and vhf radar, with special emphasis on small-scale features and anisotropy, *Ann.Geophys.*, *19*, 933–944, 2001.

Holton, J. R., *An introduction to dynamic meteorology*, Elsevier Academic Press, 2004.

Hugo, R. J., S. R. Nowlin, F. D. Eaton, K. P. Bishop, and K. A. McCrae, Hot-wire calibration in a non-isothermal incompressible pressure variant flow, *Proceedings of the SPIE symposium "Airborne Laser Advanced Technlogy II"*, *3706*, 11–23, 1999.

Jaeger, E., and M. Sprenger, A northern hemispheric climatology of indices for clear air turbulence in the tropopause region derived from era40 reanalysis data, *J. Geophys. Res.*, *112*, D20,106, 2007.

Jörgensen, F., *How to measure turbulence with hot-wire anemometers - a practical guide*, Publication 9040U6151, Dantec Dynamics A/S, Skovlunde, Denmark, 2002.

Kantha, L., and W. Hocking, Dissipation rates of turbulence kinetic energy in the free atmosphere: Mst radar and radiosondes, *J. Atmos. Solar-Terr. Phys.*, *73*, 1043–1051, 2011.

King, J. V., On the convection of heat from a small cylinder in a stream of fluid: determination of the convection constant of small platinum wires with application to hot-wire anemometry, *Phil. Trans. R. Soc.*, *214*, 373–432, 1914.

Koch, S., et al., Turbulence and gravity waves within an upper-level front, *J. Atmos. Sci.*, *62*, 3885–3908, 2005.

Labitzke, Temperature changes in the mesosphere and stratosphere connected with circulation changes in winter, *J.Atm*, *29*, 756–766, 1972.

Labitzke, K., and H. van Loon, *The stratosphere*, Springer-Verlag Berlin, 1999.

Larsen, S. E., and N. E. Busch, Hot-wire measurements in the atmosphere. part i: Calibration and response characteristics, *Technical report, DISA information*, *16*, 5–34, 1974.

Lesieur, M., *Turbulence in Fluids*, 1997.

Lilly, D. E., D. E. Waco, and S. I. Adelfang, Stratospheric mixing from high-altitude turbulence measurements, *J. Appl. Meteor.*, *13*, 488–493, 1974.

Lindborg, E., Can the atmospheric kinetic energy spectrum be explained by two-dimensional turbulence?, *J. Fluid Mech.*, *388*, 259–288, 1999.

Lübken, F., Experimental results on the role of turbulence for the heat budget of the upper atmosphere, Ph.D. thesis, 1993.

Lübken, F., M. Rapp, and P. Hoffmann, Neutral air turbulence and temperatures in the vicinity of polar mesosphere summer echoes, *J. Geophys. Res.*, *107*, 4273–4277, 2002.

Lübken, F.-J., On the extraction of turbulent parameters from atmospheric density fluctuations, *J. Geophys. Res.*, *97*, 20,385–20,395, 1992.

Lübken, F.-J., W. Hillert, G. Lehmacher, and U. von Zahn, Experiments revealing small impact of turbulence on the energy budget of the mesosphere and lower thermosphere, *J. Geophys. Res.*, *98*, 20,369–20,384, 1993.

Luce, H., S. Fukao, M. Yamamoto, C. Sidi, and F. Dalaudier, Validation of winds measured by mu radar with gps radiosondes during the mutsi campaign, *J. Atmos. Oceanic Technol.*, *18*, 817–829, 2001.

Luce, H., S. Fukao, F. Dalaudier, and M. Crochet, Strong mixing events observed near the tropopause with the mu radar and high resolution balloon techniques, *J. Atmos. Sci.*, *59*, 2885–2896, 2002.

Mauritzen, T., and G. Svensson, Observations of stably stratified shear-driven atmospheric turbulence at low and high richardson numbers, *J. Atmos. Sci.*, *64*, 645–655, 2007.

Nastrom, G., and K. Gage, A climatology of atmospheric wave number spectra of wind and temperature observed from commercial aircraft, *J.Atmos.Sci.*, *42*, 950–960, 1985.

Ottertsen, H., Atmospheric structure and radar backscattering in clean air, *Radio Science*, *4*, 1179–1193, 1969.

Phillips, O. M., The generation of clear-air turbulence by the degradation of internal waves, in *Proceedings of the International Colloqium "Atmospheric turbulence and radio wave propagation"*, pp. 130–138, 1967.

Pope, S. B., *Turbulent flows*, Cambridge University Press, 2006.

Quante, M., Turbulenz in cirruswolken mittlerer breiten, Ph.D. thesis, University Hamburg, 2006.

Ralph, F., and P. J. Neiman, Lidar observations of a breaking mountain wave associated with extreme turbulence, *Geophys. Res. Lett.*, *42*, 663–666, 1997.

Rauthe, M., M. Gerding, and F.-J. Lübken, Seasonal changes in gravity wave activity measured by lidars at mid-latitudes, *Atmos. Chem. Phys.*, *8*, 6775–6787, 2008.

Sato, T., and R. Woodman, Fine altitude resolution observations of stratospheric turbulent layers by the arecibo 430 mhz radar, *J. Atmos. Sci.*, *39*, 2546–2552, 1982.

Scherhag, R., Die explosionsartigen stratosphärenerwärmungen des spätwinters 1951/52, *Ber. Dtsch. Wetterdienstes U.S. Zone*, *6*, 51–38, 1952.

Sharman, R., S. Trier, T. Lane, and J. Doyle, Sources and dynamics of turbvulence in the upper troposphere and lower stratosphere: a review, *Geophys. Res. Lett.*, *39*, L12,803, 2012.

Sheih, C., Optimal choice of parameters for the measurement of small-scale atmospheric turbulence with an airborne hot-wire anemometer, *J. Appl. Meteor.*, *11*, 81–84, 1972.

Siebert, H., K. Lehmann, and R. Shaw, On the use of hot-wire anemometers for turbulence measurements in clouds, *J. Atmos. Oceanic Technol.*, *24*, 980–993, 2007.

Smalikho, I., F. Kopp, and S. Rahm, Measurement of atmospheric turbulence by 2-μm doppler lidar, *J. Atmos. Oceanic Technol.*, *22*, 1733–1747, 2005.

Sofieva, V. F., A. S. Gurvich, F. Dalaudier, and V. Kan, Reconstruction of internal gravity wave and turbulence parameters in the stratosphere using gomos scintillation measurements, *J. Geophys. Res.*, *112*, D12,113, 2007.

Sofieva, V. F., F. Dalaudier, R. Kivi, and E. Kyrö, On the variability of temperature profiles in the stratosphere: implications for validation, *Geophys. Res. Lett*, *35*, L23,808, 2008.

Sreenivasan, K., and R. Antonia, the phenomenology of small-scale turbulence, *Annu. Rev. Fluid Mech.*, *29*, 435–472, 1997.

Stainback, P. C., and K. A. Nagabushana, Review of hot-wire anemometry techniques and the range of their applicability, *Symposium on Thermal Anemometry, ASME FED*, *167*, 93–134, 1993.

Tatarskii, V. I., *Wave propagation in a turbulent medium*, McGraw-Hill, New York, 1961.

Tatarskii, V. I., *The effects of the turbulent atmosphere on wave propagation*, Israel Program for Scientific Translations, 1971.

Taylor, G., Statistical theory of turbulence, *Pro*, *151*, 421 – 444, 1938.

Teisserenc de Bort, L., Variations de la temperature de l'air libre dans la zone comprise entre 8 km et 13 km d'altitude, *C. R. Acad. Sci., Paris*, *134*, 987–989, 1902.

Tennekes, and Lumley, *A first course in turbulence*, The MIT Press, Cambridge, 1985.

Theuerkauf, A., M. Gerding, and F.-J. Lübken, First results of high resolution balloon-borne turbulence measurements in the stratosphere, *Proceedings of the 19th ESA Symposium on European Rocket and Balloon Programmes and Related Research*, *SP-671*, 501–505, 2009.

van Dijk, A., and F. T. M. Nieuwstadt, The calibration of (multi-) hot – wire probes: 1.temperature calibration, *Exp. Fluids*, *36*, 540–549, 2004.

Vukoslavcevic, J. M., P. V.and Wallace, The simultaneous measurement of velocity and temperature in heated turbulent air flow using thermal anemometry, *Meas. Sci. Technol.*, *13*, 1615–1624, 2002.

Waugh, D., The age of stratospheric air, *Nature*, *2*, 14 – 16, 2009.

Waugh, D., and T. Hall, Age of stratospheric air: theory, observations, and models, *Re*, *40 (4)*, 1 010, 2002.

Weber, B. L., and D. B. Wuertz, Comparison of rawinsonde and wind profiler radar measurements, *J. Atmos. Oceanic Technol.*, *7*, 157–174, 1990.

Weinstock, J., Vertical wind shears, turbulence and non-turbulence in the troposphere and stratosphere, *Geophys. Res. Lett.*, *7*, 749–752, 1980.

Welch, P. D., The use of fast fourier transform for the estimation of power spectra: A method based on time averaging over short, modified periodograms, *IEEE T. Acoust. Speech*, *AU-15*, 70–73, 1967.

Wilson, R., F. Dalaudier, and F. Bertin, Estimation of the turbulent heat flux in the lower stratosphere from high resolution radar measurements, *Geophys. Res. Lett.*, *32*, ?, 2005.

Wu, Y., J. Xu, W. Yuan, H. Chen, and J. Bian, Spectral analysis of 10-m resolution temperature profiles from balloon soundings over beijing, *Ann.Geophys.*, *24*, 1801–1808, 2006.

Wyngaard, J., Measurement of small-scale turbulence structure with hot wires, *J. Scientific Instruments*, *1*, 1105–1108, 1968.

Wyngaard, J., Atmospheric turbulence, *Annu. Rev. Fluid Mech.*, *24*, 205–234, 1992.

Yamanaka, M., and H. Tanaka, Meso- and microscale structures of stratospheric winds: A quick look of balloon observation, *J. Meteor. Soc. Japan*, *62*, 177–182, 1984.

Yamanaka, M., Y. Matsuzaka, J. Nishimura, T. Yamagami, and H. Tanaka, Stratospheric balloon-borne 'adapted gill-type' propeller anemometer, *J. Atmos. Oceanic Technol.*, *2*, 472–481, 1985a.

Yamanaka, M., H. Tanaka, H. Hirosawa, Y. Matsuzaka, T. Yamagami, and J. Nishimura, Measurement of stratospheric turbulence by balloon-borne 'glow-discharge' anemometer, *J. Meteor. Soc. Japan*, *63*, 483–489, 1985b.

Zhang, S. D., F. Yi, C. M. Huang, and K. M. Huang, High vertical resolution analyses of gravity waves and turbulence at a midlatitude station, *J. Geophys. Res.*, *117*, D02,103, 2012.

List of Figures

List of Tables

Acknowledgements

First I would like to thank Prof. F.-J. Lübken for offering me the great opportunity to work at the IAP and to perform experimental research with balloon soundings. His ideas and the countless discussions have contributed very much to this study. My special thanks goes to Michael Gerding. He always had time for me and in almost never-ending discussion we found solutions for problems occurring during the experimental work or during the analyses of the huge data set. His support has been very important for finishing my thesis. I would like to thank my colleague Torsten Köpnick for his substantial support in developing electronic devices for the balloon experiments. My thanks also goes to all colleagues at the IAP for the friendly environment and many fruitful discussions. I would like to thank Jens Hildebrand for the careful proofreading of my thesis and for the help with Latex secrets. I would like to thank the German Aerospace Center (DLR) and the Swedish National Space Board (SNSB) for providing the opportunity to take part in the REXUS/BEXUS programme. Therefore it was possible to launch LITOS from Kiruna and to obtain new insights in stratospheric turbulence. Furthermore, thanks to the DLR Berlin-Adlershof it was possible to perform comprehensive laboratory studies. For these studies, the small wind channel has been kindly provided by the Lehrstuhl Strömungsmechanik (LSM) at the University of Rostock. In addition, thanks to the LSM we could calibrate our sensors in their wind channel facilities. Last but not least, I especially would like to thank Fiete for his continuous help and support during my work. Without his encouragements I would not been able to finish my thesis.

Erklärung

Hiermit versichere ich an Eides statt, die vorgelegte Arbeit sebstständig und ohne fremde Hilfe verfasst, keine außer den von mir angegebenen Hilfsmitteln und Quellen dazu verwendet und die den benutzten Werken inhaltlich oder wörtlich entnommenen Stellen als solche kenntlich gemacht zu haben.
Die Arbeit wurde bisher weder im Inland noch im Ausland in gleicher oder ähnlicher Form einer anderen Prüfungsbehörde vorgelegt. Weiterhin erkläre ich, dass ich ein Verfahren zur Erlangung des Doktorgrades an keiner anderen wissenschaftlichen Einrichtung beantragt habe.

Kühlungsborn, den 2.11.2012

(Anne Theuerkauf)